Facoltà di Scienze Matematiche, Fisiche e Naturali
Dipartimento di Fisica

Dottorato in Fisica, XXVIII ciclo

Precise measurement of the charged B meson mass at the LHCb experiment

Tutor:
Prof. **Giovanni Carboni**

Coordinatore:
Prof. **Roberto Benzi**

Candidato:
Emiliano Furfaro

Anno Accademico
2015-2016

Acknowledgments

The work described in this thesis is the fruit of labor made with the "Tor Vergata" LHCb group in Rome. The work has been possible thanks to the useful and precious guidance of Professor Giovanni Carboni, my tutor and my teacher during this years, who substantially contributed to my educational growth. I wish to express my gratitude for his insightful observations and his generous advice that enriched my work. My gratitude is also extended to Dr. Alessia Satta and Prof. Emanuele Santovetti for their fundamental support and precious suggestions throughout my work. This thesis could not have been completed without their generous assistance.

I must express my gratitude to my wife Elisabetta for her support, encouragement and patience. Finally I would like to thank my family, my mother, my father and my sister, as well as my extended family: my mother, my father and my sister in law.

Contents

Introduction

In the 1957 the parity (P) violation of weak interactions was discovered by Chien Shiung Wu in the β decay of $^{60}Co \rightarrow {}^{60}Ni + e^- + \bar{\nu}_e$ [1]: the parity violation implies that some physical phenomena don't have the same behaviour when the spatial coordinates are inverted. The parity is not a symmetry for the weak interactions.
One year later even the charge conjugation (C) symmetry violation was discovered by M. Goldhaber during the studies over neutrino helicity [2].
It was believed that, while P and C operator separately led to asymmetries, their CP combination did not. However, in the 1964, the CP violation was observed for the first time by J.H. Christenson, J. W. Cronin, V. L. Fitch and R. Turlay in the neutral kaons decay [3]. CP violation is still one of the most interesting phenomena in particle physics and it is stil an object of studies.
According to the Standard Model (SM) CP violation is explained by the CKM (*Cabibbo-Kobayashi-Maskawa*) matrix, whose elements have to be experimentally estimated. In this regard the b physics represents one of the critical elements of the flavor physics programme. It is a powerful lab to test the SM predictions and to constraint CKM elements.
CP violation in B mesons decay was observed for the first time in the 2001 by the BaBar experiment at SLAC [4] and by the BELLE experiment at KEK [5].
Another sector that is investigated by means of B meson decays is the Quantum Chromodynamics (QCD) that describes the strong interaction between quarks and gluons confined inside hadrons. In order to prove the theoretical predictions and to verify if QCD is the correct theory of strong interactions, accurate experimental measurements are needed.
At the hadronic scale the coupling constant of QCD is of order unity and perturbative methods fail. For this reason a non-perturbative tool for calculating the hadronic spectrum and the matrix elements of any operator called lattice QCD (LQCD) has been developed.
In the b physics sector, after after the b quark mass value is extrapolated from calculation the b hadron masses could be extracted and then could be compared to

experimental measurement.
Nowadays, thanks to the LHCb experiment, more precise values of hadrons physical properties can be reached: the aim of this study is to give a precise measurement of the charged B meson masses.
LHCb (Large Hadron Collider beauty) is one of the four high energy physics experiments of LHC (Large Hadron Collider) at CERN (European Organization for Nuclear Research) in Geneva. In order to study the b physics, LHCb takes advantage of the high luminosity available at LHC that produces protons beams with a design center of mass energy of 14 TeV: the cross section for $b\bar{b}$ mesons pairs production is foreseen to be about 500 μb with a luminosity of 2×10^{32} cm^{-2}s^{-1} that corresponds to 10^{12} $b\bar{b}$ pairs produced per year. Thanks to this high statistics is possible to reduce errors with respect to previous measures and furthermore to study with high precision extremely rare processes with branching fractions in the order of 10^{-9}.
In these first years of activity LHC was able to accumulate an integrated luminosity of about 30 fb^{-1} with a peak luminosity of 7.7×10^{33} cm^{-2}s^{-1}.

During 2010-2011, the LHCb experiment recorded data collisions both at $\sqrt{s} = 7$ and 8 TeV and were able to perform the measurement of the branching ratio of the rare decay $B_s \to \mu^+\mu^-$ [8], studies on the forward-backward asymmetry of the muon pair in the flavour changing neutral current, the measurement of the CP violating phase in the decay $B_s \to J/\psi\phi$ [9] and the recent studies on exotic structures in $J/\psi\phi$ [108] mass spectrum and in $J/\psi K$ mass spectrum [109] in the decay $B^+ \to J/\psi\phi K^+$.

Chapter 1

Beauty physics

1.1 The Standard Model

The Standard Model (SM) is a quantum field theory of the fundamental interactions between elementary particles [10, 11, 12]. In the SM the interactions arise by requiring that the theory is invariant under local gauge tranformations. The invariance under a local phase gauge transformation leads to electromagnetic interactions and to charge conservation: U(1) symmetry group. In the electroweak theory, electromagnetic interactions are unified to weak interactions, which are invariant under local phase transformation in the group of isospin non abelian transformations SU(2). The strong interaction theory, Quantum Chromodynamics (QCD), arises from the invariance under local transformations in the group of color SU(3). The SM is therefore defined as a theory based on $SU(3)_{color} \otimes SU(2)_L \otimes U(1)_Y$ gauge symmetry. Physical observations are compatible with SM hypothesis: last years of data taking at LHC allowed us to observe the Higgs Boson that explains the origin of the masses of the particles through the Higgs Mechanism [13]. However it is known that there are some unresolved questions, so SM can not considered a complete model. First of all it doesn't include the gravitational theory; secondly, in SM theory there are many parameters that are not base quantities but have to measured by experiments. Some of these are the parameters that rule the CP violation.

In the SM frame the fundamental constituents of matter are the fermions that interact with each other by means exchange bosons.
Fermions are 1/2 spin particles and are divided in two category: leptons, subjected to electromagnetic and weak interactions, and quarks, subjected to strong interactions

too[1]. In table 1.1 the main features of leptons and the main ones related to quarks are listed.

Table 1.1: Leptons and Quarks summary table [14]

lepton	**mass (MeV/c^2)**	**Q/e**
ν_e	$< 2 \times 10^{-6}$	0
e^-	$0.5109989461 \pm 0.0000000031$	-1
ν_μ	< 0.19	0
μ^-	$105.6583745 \pm 0.0000024$	-1
ν_τ	< 18.2	0
τ	1776.86 ± 0.12	-1
Quark flavor	**mass (MeV/c^2)**	**Q/e**
up	$2.3^{+0.7}_{-0.5}$	$\frac{2}{3}$
down	$4.8^{+0.5}_{-0.3}$	$-\frac{1}{3}$
charm	1275 ± 25	$\frac{2}{3}$
strange	95 ± 5	$-\frac{1}{3}$
top	$173210 \pm 510 \pm 710$	$\frac{2}{3}$
bottom (beauty)	4180 ± 30	$-\frac{1}{3}$

Leptons are listed according to three families: electronic, muonic, tauonic and each lepton has its corresponding antilepton. Each family consists of a charged lepton, that is able to interact by means weak and electromagnetic interactions, and of a neutral one that interacts by means weak interactions only.
Quarks are listed in ascending order according to their masses and, unlike leptons, they have never been observed as free particles. For each quark also there is the corresponding antiquark. Strong interactions are characterized by an additional

[1]In order to be thorough, we should include gravitational interactions too since quarks and leptons have a mass; however this force is completely negligible at fundamental level, being gravity the weakest of the known interactions.

quantum number, called *color*, that represents the strong charge. For each flavor three colors exist: *Red*, *Green* and *Blue* (R, G, B) symbolically. Since the strength of the strong interaction is very intense, quarks are confined inside hadrons and constitute neutral color particles, or white color singlet, (all free particles observed have color charge equal to zero): *baryons*, constituted by three quarks with colors R-G-B, and *mesons*, constituted by a quark and the corresponding antiquark to form a color-anticolor pair. The strong interaction is responsible for protons and neutrons to be bound inside the atomic nucleus.
Gauge bosons, the particles that carry fundamental interactions, are spin 1 particles: the gauge boson of the electromagnetic interaction is the photon, γ, having zero mass; in the weak interaction three gauge bosons are exchanged, $W^{\pm}$ with masses $\simeq$ 80 GeV$/c^2$ and Z^0 with mass $\simeq$ 90 GeV$/c^2$; the strong interaction is finally mediated by the exchange of massless gauge bosons called gluons, g, that act between quarks, antiquarks, and other gluons.

1.2 The CKM matrix

As predicted by Kobayashi and Maskawa in 1973 [22], the b quark forms, together with its heavier partner t, the third generation of quarks, as shown in the previous section. Such prediction was confirmed in the 1977 by the first observation of a $b\bar{b}$ meson [23].
In SM the gauge bosons of weak interaction take their masses by spontaneous symmetry breaking caused by the Higgs mechanism [13]. For what concerns fermions, interactions between Yukawa and the Higgs fields give the mass terms to the massive particles. Let us linger on quarks:

$$\mathcal{L} = -Y^D_{ij}\overline{Q^I_{L_i}}\phi D^I_{R_j} - Y^U_{ij}\overline{Q^I_{L_i}}\tilde{\phi}U^I_{R_j} + h.c. \tag{1.1}$$

where $Y^{U,D}$ are 3×3 complex matrixes, ϕ is the Higgs field, i e j are the indexes of generations; Q^I_L are lefthanded quarks pairs and D^I_R, U^I_R are righthanded quarks singlets of the *down* (d, s, b) and *up* (u, c, t) type in the base of weak eigenstates. When ϕ takes a vacuum expectation value different from zero, $\langle\phi\rangle = (0, v/\sqrt{2})$, the equation (1.1) gives the mass terms for quarks. Physical states are obtained by the diagonalization of $Y^{U,D}$ by means unitary matrixes, $T^{U,D}_{L,R}$, getting:

$$M^f_{diag} = T^f_L Y^f T^{f\dagger}_R \left(\frac{v}{\sqrt{2}}\right) \qquad f = U, D\,. \tag{1.2}$$

In this way the quark fields, lefthanded and righthanded, are converted in their mass eigenstates [15]:

$$U^m_{L[R]} = T^U_{L[R]} U_{L[R]}, \quad D^m_{L[R]} = T^D_{L[R]} D_{L[R]} \,. \tag{1.3}$$

Let us consider now the interaction lagrangian between quarks and W boson:

$$\mathcal{L}^{cc}_W = -\frac{g}{\sqrt{2}}(J^+_\mu W^{-,\mu} + J^-_\mu W^{+,\mu}) \tag{1.4}$$

where the charged current is defined as:

$$J_\mu = \overline{U}_L \gamma_\mu D_L \tag{1.5}$$

and W^μ represents the vector boson.
In terms of the mass eigenstates (equation (1.3)) the equation (1.5) takes this form:

$$J_\mu = (\overline{u}, \overline{c}, \overline{t})_L \gamma_\mu V_{CKM} \begin{pmatrix} d \\ s \\ b \end{pmatrix}_L \tag{1.6}$$

where:

$$V_{CKM} = T^u_L T^{d\dagger}_L \tag{1.7}$$

is the Cabibbo-Kobayashi-Maskawa unitary matrix (CKM) [16, 17].
It connects the weak interactions eigenstates (d', s', b') to the mass eigenstates (d, s, b) by means of unitary transformation:

$$\begin{pmatrix} d' \\ s' \\ b' \end{pmatrix} = \begin{pmatrix} V_{ud} & V_{us} & V_{ub} \\ V_{cd} & V_{cs} & V_{cb} \\ V_{td} & V_{ts} & V_{tb} \end{pmatrix} \begin{pmatrix} d \\ s \\ b \end{pmatrix} \equiv V_{CKM} \begin{pmatrix} d \\ s \\ b \end{pmatrix} . \tag{1.8}$$

CKM matrix is a $n \times n$ complex parameters matrix with $n = 3$, so the number of real parameters is given by $2n^2 = 18$. Unitary condition

$$\sum_j V_{ij} V^*_{jk} = \delta_{ik} \,,$$

reduces to n^2 the number of independent real parameter [15]. The $2n$ quark fields can be redefined by choosing $2n-1$ arbitrary relative phases, in this way the independent parameters are reduced to:

$$n^2 - (2n-1) = (n-1)^2 = 4 \,.$$

where $\frac{1}{2}n(n-1)$ describes the independent rotation angles:

$$N_{angle} = \frac{1}{2}n(n-1) = 3\,. \tag{1.9}$$

Consequently the number of the independent phases will be:

$$N_{phase} = \frac{1}{2}(n-1)(n-2) = 1\,. \tag{1.10}$$

The CKM matrix is defined by 3 angles and 1 phase: such phase is the one that generates the CP violation in the SM framework [18]. Among the different parameterizations, the most convenient is the one proposed by Wolfenstein [19], which corresponds to a phenomenological expansion up to the third order of the quantity $\lambda \equiv |V_{us}| = \sin\theta_c \simeq 0.22$, where θ_c is the Cabibbo's angle [16]:

$$V_{CKM} = \begin{pmatrix} 1-\frac{\lambda^2}{2} & \lambda & A\lambda^3(\varrho - i\eta) \\ -\lambda & 1-\frac{\lambda^2}{2} & A\lambda^2 \\ A\lambda^3(1-\varrho-i\eta) & -A\lambda^2 & 1 \end{pmatrix} + \mathcal{O}(\lambda^4)\,. \tag{1.11}$$

From B mesons decays the elements $|V_{cb}|$ and $|V_{ub}|$ were measured [20]: from them, A and $\sqrt{\rho^2+\eta^2}$ can be obtained.
The unitarity of CKM matrix, $V_{CKM}V^{\dagger}_{CKM} = 1$, leads to a set of nine equations consisting in three normalization relations and six orthogonality relations. The last ones could be represented as six triangles in the complex plane, all having the same area [21]. However, only two of these triangles have the sides with comparable dimensions, having order of magnitude of $\mathcal{O}(\lambda^3)$. In the remaining ones, on the contrary, one side is suppressed of $\mathcal{O}(\lambda^2)$ or $\mathcal{O}(\lambda^4)$ if compared to the others. The orthogonality relations describing the triangles with comparable sides are the following ones:

$$V_{ud}V^*_{ub} + V_{cd}V^*_{cb} + V_{td}V^*_{tb} = 0\,, \tag{1.12}$$
$$V_{ud}V^*_{td} + V_{us}V^*_{ts} + V_{ub}V^*_{tb} = 0\,. \tag{1.13}$$

As can be seen from CKM matrix in the equation 1.11, these two triangles are identical to $\mathcal{O}(\lambda^3)$ order. At LHC, thanks to the high experimental precision reached, the two triangles can be distinguished, so higher orders have to take into account (figure 1.1).

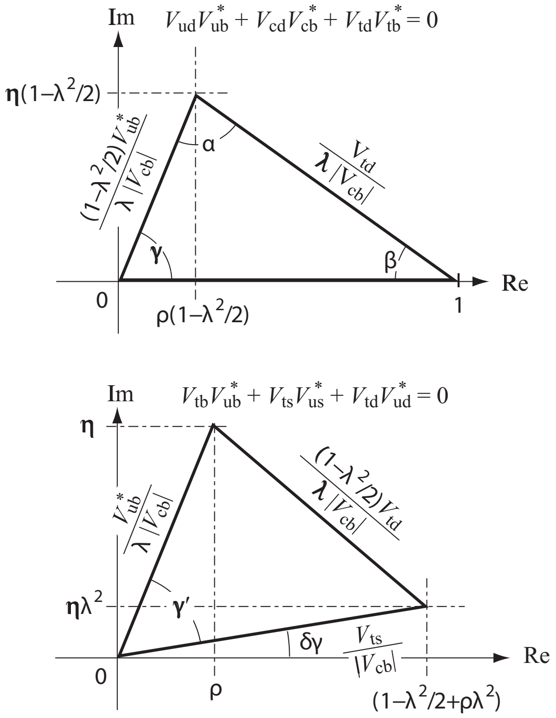

Figure 1.1: Two unitarity triangles in the Wolfenstein parametrization till $\mathcal{O}(\lambda^5)$ order.

α, β, γ, $\delta\gamma$ angles are defined as:

$$\alpha \equiv \arg\left(-\frac{V_{td}V_{tb}}{V_{ud}V_{ub}^*}\right) \qquad \beta \equiv \arg\left(-\frac{V_{cd}V_{cb}}{V_{td}V_{tb}^*}\right)$$

$$\gamma \equiv \arg\left(-\frac{V_{ud}V_{ub}}{V_{cd}V_{cb}^*}\right) \qquad \delta\gamma \equiv \arg\left(-\frac{V_{us}V_{ts}}{V_{cd}V_{cb}^*}\right) \tag{1.14}$$

As it will be seen in the next sections, b mesons decays give the possibility to study and to measure the parameters of the unitarity triangles. The angles can be extrapolated indirectly by measuring the length of the sides or, in the SM framework, directly from CP asymmetries. The lack of agreement between the two different methods could be an indication for “New Physics”.
A list of decays in the neutral B meson sector used to measure the angles of the unitary triangles is shown as an example:

- $B_d^0 \to \pi^+\pi^-$:
  this decay permits us to define the α angle. The final state is given by a tree diagram for the decay $b \to u$ and by a little bit not negligible contribution from a penguin diagram $b \to u$.

- $B_d^0 \to J/\psi K_s^0$:
  this decay is called *golden channel* and allow us to find the β parameter and, like the previous one, is made up by a tree and a penguin diagram. The interest for this channel comes from the absence of QCD factors: CP violation effects are large, due to interference between decay and K and B oscillations.

- $B_s^0 \to J/\psi\phi$:
  from this decay it is possible to find $\delta\gamma$. In this case too, CP violation is given by interference between decay and mixing.

1.3 Property of beauty particles

B mesons are quark-antiquark bound sistems of type $\bar{b}q$ where q could be one of u, d, s and c quark. In this way four different states are formed, two neutral and two charged.
b baryons are a three quark composition of type qqb. The first b baryon to be observed was the Λ_b^0 while for the Ξ_b there was only an indirect observation [24]. Thanks to the huge amount of data collected at Tevatron and by LHCb a large variety of b baryons were observed [25, 31]. In the table 1.2 the observed b hadrons are listed.

Since the b quark is the lighter element of the third generation quark doublet, the decays of b hadrons occur via generation-changing processes through the CKM matrix. Because of this, many interesting features such as loop and box diagrams, flavor oscillations, CP asymmetries, can be observed in the weak decays of b hadrons. SM permits two generic types of decay for b quark: tree-level and loop-level (figure 1.2). Tree-level decays occur due to the exchange of $W^\pm$ bosons and thus they are not sensitive to new phenomena originating from physics beyond SM. In the loop-level processes the $W^\pm$ boson could emit a Z^0 boson or a photon creating a quark-antiquark pair. In such loops, massive, virtual and so far undetected particles can be exchanged: this kind of diagram provides potential sensitivity to physics beyond the SM.

Table 1.2: b particles summary table (values from PDG [14])

meson	$\bar{b}q$	**mass (Mev/c^2)**	**mean life (10^{-12}s)**
B_u^+	$\bar{b}u$	5279.29 ± 0.15	1.638 ± 0.004
B_d^0	$\bar{b}d$	5279.61 ± 0.16	1.520 ± 0.004
B_s^0	$\bar{b}s$	5366.79 ± 0.23	1.510 ± 0.005
B_c^+	$\bar{b}c$	6275.1 ± 1.0	0.507 ± 0.009
baryon	qqb	**mass (Mev/c^2)**	**mean life (10^{-12}s)**
Λ_b^0	udb	5619.51 ± 0.23	1.466 ± 0.010
Σ_b^+	uub	5811.3 ± 1.9	NA
Ξ_b^0	usb	5791.9 ± 0.5	1.464 ± 0.031
Ξ_b^-	dsb	5794.5 ± 1.4	1.560 ± 0.040
Ω_b^-	ssb	6046.4 ± 1.9	$1.57^{+0.23}_{-24}$

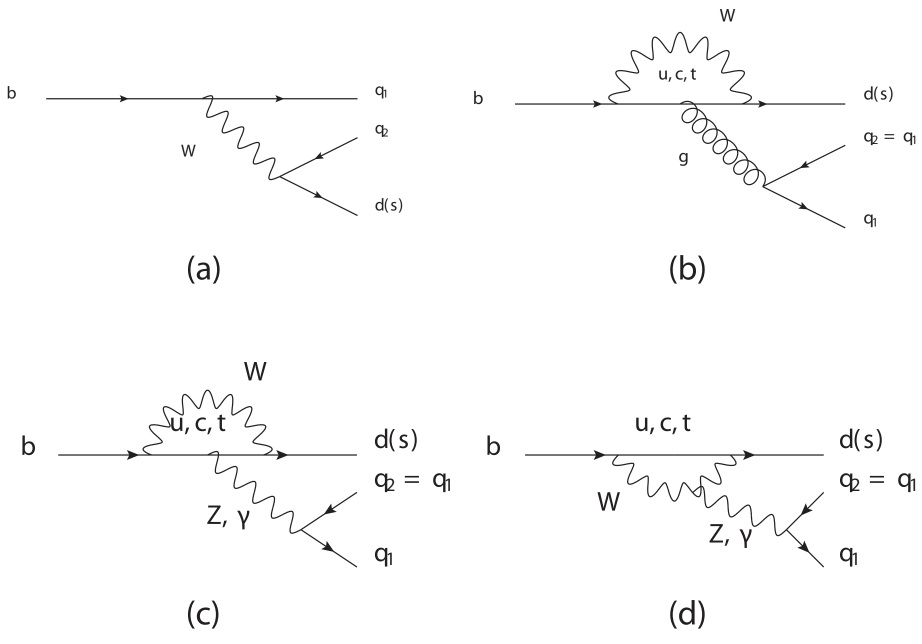

Figure 1.2: Tree-level (a) and loop-level (b, c, d) processes.

1.4 b production at LHC

The proton-proton, pp, inelastic scattering is explained, in the framework of QCD parton model, as a parton-parton elastic scattering. As proposed by Feynman in 1969, partons are the hadrons' constituents: called quarks and gluons. According to the model, the deep inelastic scattering of hadrons, typical of high energies, can be sketched as a collision between two free partons: the typical time scale of the parton-parton interaction is much smaller compared to the typical time evolution parton time scale. Throughout the interaction, parton density functions $f_i(x)$ can be introduced. Such functions describe the number of the i type parton that carries a fraction of the total hadron momentum between x and δx, being x defined as: $x = \frac{\mathbf{P}_{parton}}{\mathbf{P}_{hadron}}$.
Let the interacting hadrons momentum be P_1 and P_2, then the total cross section will be:

$$\sigma(P_1, P_2) = \sum_{ij} \int dx_1 dx_2 f_i(x_1) f_j(x_2) \sigma_{ij}(x_1 P_1, x_2 P_2) \tag{1.15}$$

where the sum is made over quarks and gluons. At LHC energies the dominating process for $b\bar{b}$ production in the collision

$$pp \to b\bar{b} + \ldots \text{ other } \ldots$$

is shown in figure 1.3.

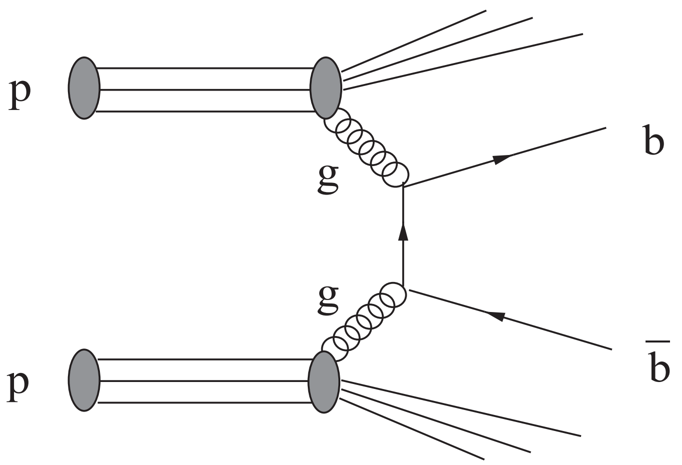

Figure 1.3: Diagram illustrating the dominating process for high energies $b\bar{b}$ pairs production

Such a diagram is referred to as *gluon fusion*. In the heavy quarks production QCD allows us to study this kind of precess in a perturbative way, which considerably simplifies the cross section calculations.
In figure 1.4 a physics framework where the z axis coincides with the beams direction is shown.
In such framework the transverse momentum referred to z, p_t, and the polar angle

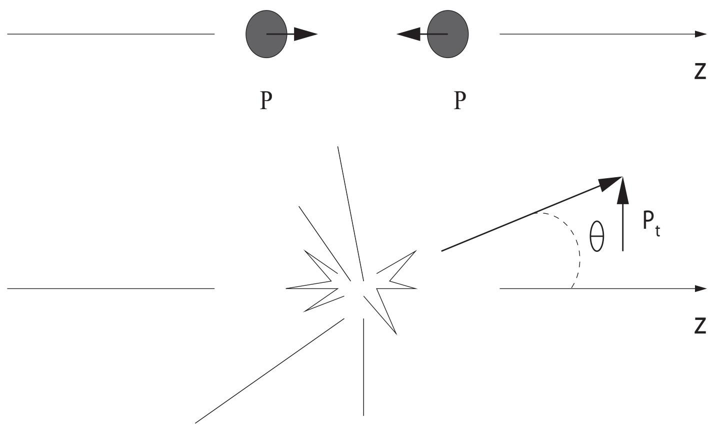

Figure 1.4: Cinematics of pp collision

θ related to the beam direction are defined. From the projection of p on z axis the *rapidity*, y, can be derived: in the high energy limit (i.e. m is negligible) the rapidity is approximated to the *pseudorapidity*, η. In such limit the rapidity tends to its maximum as $\theta \to 0, \pi$.
We can conclude that the maximum probability to observe $b\bar{b}$ pairs from high energy protons collisions is found in the forward direction production (figure 1.5) with highly correlated pairs ($\Delta y \sim 0$).
If compared to other colliders LHC is the richest B mesons source. LHC is a *p-p* collider with 14 TeV center of mass energy, 40 MHz bunch crossing frequency and 1×10^{34} cm^{-2}s^{-1} luminosity. Once the cross section for the process is fixed, the luminosity is referred to as the number of the particles traversing the impact area in the time unit. A related quantity is integrated luminosity that is the integral of the luminosity with respect to time. The main expected values for proton-proton reactions with such $\sqrt{s}$ are listed in table 1.3.
Thanks to this large b production cross section ($\sigma = 500\mu b$), even with a reduced luminosity (2×10^{32} cm^{-2}s^{-1}) a big amount of $b\bar{b}$ pairs are produced per year: 10^{12}pairs/10^7s. Any kind of b hadrons are produced: B_u (40%), B_d (40%), B_s (10%) and B_c and others, Λ_b^0, Σ_b^+, Ξ_b^0, Ξ_b^-, Ω_b^- etc., (10%).

Table 1.3: Values evaluated with PYTHIA

$\sigma_{tot.}$	100 mb
$\sigma_{inel.}$	80 mb
$\sigma_{inel.} - \sigma_{diffr.}$	55 mb
$\sigma_{b\bar{b}}$	500 μb
$\sigma_{c\bar{c}}$	1.5 μb

B hadrons produced in the forward region have a mean momentum of 80 GeV/c, that corresponds to a mean decay path of about 7 mm.
Quark b events are only a little fraction of the total production:

$$\frac{\sigma_{b\bar{b}}}{\sigma_{inel.}} = 0.6\%$$

so, in order to study the b physics, a very fast and robust trigger system is needed to assure an efficient and good event selection, considering the big amount of produced events.

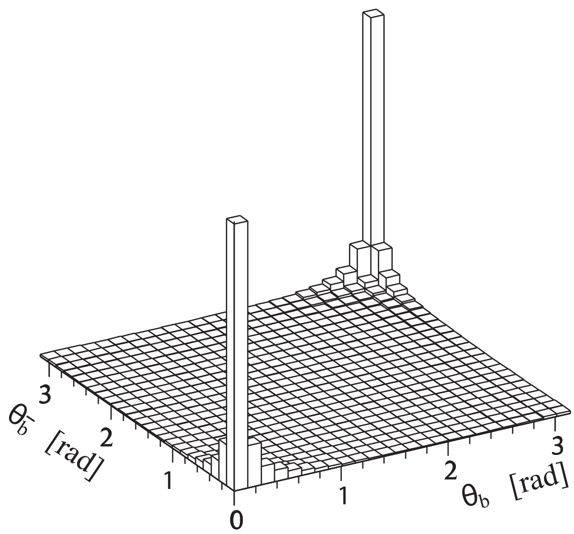

Figure 1.5: b and $\bar{b}$ polar angles as calculated by the event generator PYTHIA

1.5 b physics as stringent Standard Model test

As stated before, B mesons could be used as a laboratory to evaluate the CKM matrix parameters. Starting from the $\lambda = \sin\theta_C$ value (that could be determined from kaon decays, hyperon decays and tau decays) being 0.22536 ± 0.00061 [20], the triangles in figure 1.1 are completely given by ρ and η that can be derived from $|V_{cb}|$, $|V_{ub}|$ and $|V_{td}|$.
$|V_{cb}|$ and $|V_{ub}|$ values (see section 1.2) are extrapolated from semileptonic B meson decays amplitudes based on $b \to cl\nu$ and $b \to ul\nu$ processes. Precision determinations of these elements are central to test the CKM sector of the Standard Model.
$|V_{td}|$ value can be obtained by B_d^0-$\bar{B}_d^0$ oscillations.
Theoretical uncertainties in hadronic effects constraint the accuracy on the current measurement of this matrix element. A more precise value can be obtained by extrapolating $|V_{ts}|$ from B_s^0-$\bar{B}_s^0$ oscillation and then using the ratio $|V_{td}/V_{ts}|$ to get the $|V_{td}|$ value [20].
Once got ρ and η parameters are known, we are able to calculate angles α, β, γ and $\delta\gamma$ in indirect way. In the SM these angles, or their combinations, could be also easily calculated from CP asymmetries in the different final states of B mesons decay that could be originated by the complex phase of the CKM matrix. A crucial milestone was the first observation of CP violation in the B meson system in the 2001, by the BaBar [39] and Belle [40] collaborations.
Recent developments in b hadron physics include the significant improvement in experimental determination of γ angle, the increased information on B_s and B_c and the observation of $B_s \to \mu^+\mu^-$ decays.
Other fundamental parameters of the Standard Model are the quark masses: since quarks are not observed as free particles their masses have to be extrapolated by comparing the result of mass hadron measurements with theoretical calculation. Thanks to the high luminosity reached at LHC, precise measurements of B mesons mass could be obtained, therefore the b quark mass could be calculated with high precision.
From the last studies, absolute values of CKM matrix elements result to be:

$$V_{CKM} = \begin{pmatrix} 0.97427 \pm 0.00014 & 0.22536 \pm 0.00061 & 0.00355 \pm 0.00015 \\ 0.22522 \pm 0.00061 & 0.97343 \pm 0.00015 & 0.0414 \pm 0.0012 \\ 0.00886^{+0.00033}_{-0.00032} & 0.0405^{+0.0011}_{-0.0012} & 0.99914 \pm 0.00005 \end{pmatrix}. \quad (1.16)$$

In figure 1.6 the constraints on unitarity triangle of figure 1.1 (top side) are shown: the colored areas represent the allowed regions for $\bar{\rho} = \rho(1 - \lambda^2/2)$ and for $\bar{\eta} =$

$\eta(1 - \lambda^2/2)$ values obtained by recent measurements of the physics parameters like $\sin 2\beta$ or ΔM_d and ΔM_s.

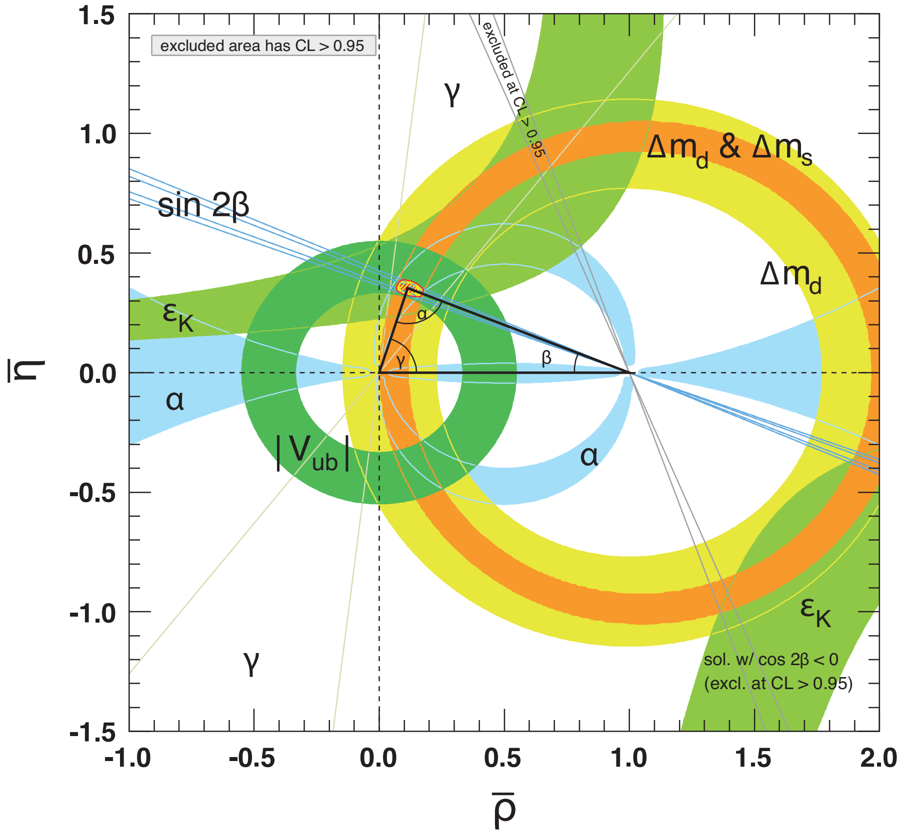

Figure 1.6: Constraints on Unitarity Triangle where $\bar{\rho} = \rho(1 - \lambda^2/2)$ and $\bar{\eta} = \eta(1 - \lambda^2/2)$

1.5.1 CP violation in b meson decay

In general, we can define the decay amplitudes of a state M and its CP conjugate $\bar{M}$, both with a final state f and its CP conjugate $\bar{f}$, as:

$$\begin{aligned} A_f &= \langle f|\mathcal{H}|M\rangle & \bar{A}_f &= \langle f|\mathcal{H}|\bar{M}\rangle \\ A_{\bar{f}} &= \langle \bar{f}|\mathcal{H}|M\rangle & \bar{A}_{\bar{f}} &= \langle \bar{f}|\mathcal{H}|\bar{M}\rangle \end{aligned} \tag{1.17}$$

where $\mathcal{H}$ is the Hamiltonian governing weak interaction. The action of CP operator on these states introduces two phases, ξ_M and ξ_f, that depend on the state flavor content.
In b meson decay three different CP violation processes could be defined:

- CP violation in decay, also known as *direct* CP violation. In charged mesons is the only source of CP violation.
- CP violation in mixing, occurring in neutral meson decays, also known as indirect CP violation: the probability of a B^0 to oscillate into a $\bar{B}^0$ is different from the probability of the conjugate process.
- CP violation in interference between one decay without mixing and one with mixing, that occurs only in decays with final states that are common both to neutral meson and its antiparticle, including all CP eigenstates.

Direct CP violation

Direct, or in decay, CP violation occurs when the decay amplitude for a process and the one for its CP conjugate are different: a different rate for the process $B_q \to f$ and for the process $\bar{B}_q \to \bar{f}$ can be observed (figure 1.7).

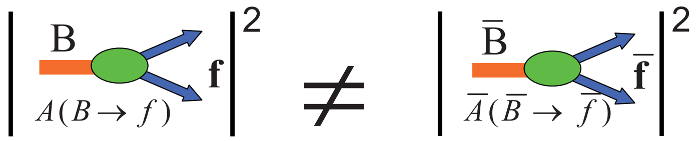

Figure 1.7: *Direct* CP violation

Hence we consider decays written as: $A_f = \langle f|\mathcal{H}|B_q\rangle$ e $\bar{A}_{\bar{f}} = \langle \bar{f}|\mathcal{H}|\bar{B}_q\rangle$. In general the total amplitude can be written as a sum of different contributions, given by all possible decay channels:

$$A_f = \sum_i A_i e^{i\phi_i} e^{i\delta_i} \qquad \bar{A}_{\bar{f}} = \sum_i A_i e^{-i\phi_i} e^{i\delta_i} \tag{1.18}$$

where ϕ_i is the weak phase and δ_i is the strong phase.
The weak phase is connected to CKM matrix, so it is given by complex parameters in the Lagrangian of weak interactions and represents the CP violation: it takes different signs in A_f and in its conjugate $\bar{A}_{\bar{f}}$.

The strong phase is due to interaction between quarks in the final state: it takes the same sign both in A_f and $\bar{A}_{\bar{f}}$ and preserve CP.
When CP is preserved all the weak phases are equal, $\phi_i = \phi_j$, and so:

$$\left| \frac{\bar{A}_{\bar{f}}}{A_f} \right| = 1 \, . \tag{1.19}$$

On the other side, mesons could decay by many mechanisms with different amplitudes and with different weak and strong phases; this leads to an interference between decay amplitudes causing a difference between $B_q \to f$ and $\bar{B}_q \to \bar{f}$ rates. Then:

$$\left| \frac{\bar{A}_{\bar{f}}}{A_f} \right| \neq 1 \, . \tag{1.20}$$

Let's now consider a decay occurring by means of two processes, A_1 and A_2, with total amplitude:

$$A = A_1 e^{i\phi_1} e^{i\delta_1} + A_2 e^{i\phi_2} e^{i\delta_2}$$

and its conjugate:

$$\bar{A} = A_1 e^{-i\phi_1} e^{i\delta_1} + A_2 e^{-i\phi_2} e^{i\delta_2} \, .$$

The asymmetry can be defined in the following way:

$$\mathcal{A} \equiv \frac{|A|^2 - |\bar{A}|^2}{|A|^2 + |\bar{A}|^2} = -\frac{2|A_1||A_2| \sin(\delta_1 - \delta_2) \sin(\phi_1 - \phi_2)}{|A_1|^2 + |A_2|^2 + 2|A_1||A_2| \cos(\delta_1 - \delta_2) \cos(\phi_1 - \phi_2)} \, . \tag{1.21}$$

Only in particular conditions the asymmetry is enough large to be observed: both the involved processes must have comparable amplitudes; furthermore the effect could be reduced or canceled by the presence of other contributions.
With the tree-level decay of the processes $B^\pm \to D^{(*)} K^\pm$, called *golden channel*, measurement of the γ angle is obtained. The decays used are: $B^+ \to D^0 K^+$, which proceeds via the quark transition $b \to \bar{u} c \bar{s}$, and $B^- \to \bar{D}^0 K^-$, which proceeds via the quark transition $b \to u \bar{c} \bar{s}$, with the D^0 and $\bar{D}^0$ decaying into a common final state. The CP-conjugate processes are sensitive to $\delta - \gamma$. Measurements of branching ratios and CP asymmetries allow the determination of γ [33] and δ from amplitude triangle relations.

Indirect CP violation

Indirect, or in mixing, CP violation occurs for neutral decays only and it shows as difference between $\Gamma(B^0(0) \to \bar{B}^0(t))$ and $\Gamma(\bar{B}^0(0) \to B^0(t))$ transition probability (figure 1.8).

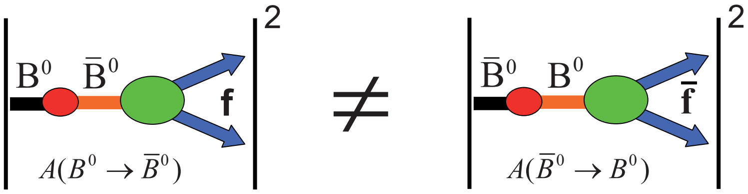

Figure 1.8: *Indirect* CP violation

This kind of CP violation is visible for example in B neutral semileptonic decays and we can define semileptonic asymmetry as:

$$\mathcal{A}_{SL}(t) \equiv \frac{\Gamma(\bar{B}^0(t) \to l^+\nu X) - \Gamma(B^0(t) \to l^-\bar{\nu} X)}{\Gamma(\bar{B}^0(t) \to l^+\nu X) + \Gamma(B^0(t) \to l^-\bar{\nu} X)} = \frac{1 - |q/p|^4}{1 + |q/p|^4} \,. \tag{1.22}$$

In this case the asymmetry is given by the interference between amplitudes related to intermediate virtual states, referred to as *off-shell*, and the ones related to *on-shell* intermediate states.
As stated before, $|q/p|$ ratio is very close to 1 so it is very hard to make precise calculations of such kind of asymmetry.

CP violation in interference between decay and mixing

When both B^0 and $\bar{B}^0$ can decay to the same final state (CP eigenstate) f_{CP}, then CP violation could occur by interference between decay and *mixing* (figure 1.9). In this case the $B^0 \to f_{CP}$ process has two different contributions (figure 1.10): the meson could directly decay to the final state or change flavor and decay later.
This interference could introduce a CP asymmetry defined as:

$$\mathcal{A}_{f_{CP}}(t) \equiv \frac{\Gamma(\bar{B}^0(t) \to f_{CP}) - \Gamma(B^0(t) \to f_{CP})}{\Gamma(\bar{B}^0(t) \to f_{CP}) + \Gamma(B^0(t) \to f_{CP})} \,. \tag{1.23}$$

From (1.17), the amplitudes for the two processes could be written as A_f for $B^0 \to f$ and $\bar{A}_f$ for $\bar{B}^0 \to f$. We can now introduce the parameter:

$$\lambda_f \equiv \frac{q\bar{A}_f}{pA_f} = \eta_f \frac{q\bar{A}_{\bar{f}}}{pA_f} \text{ , with } \eta_f = \frac{\bar{A}_{\bar{f}}}{\bar{A}_f} \tag{1.24}$$

that takes into account the combined effect of oscillation and decay. It is possible

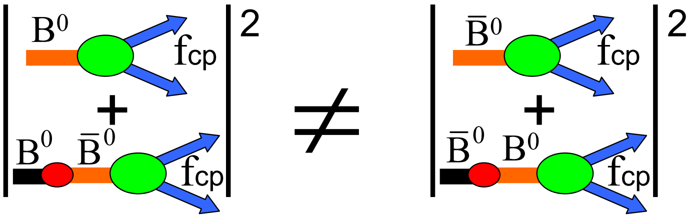

Figure 1.9: CP violation in interference between decay and *mixing*

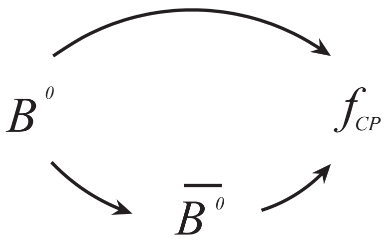

Figure 1.10: Interfering processes that origin CP violation in interference between decay and *mixing*

to solve (1.23) in a simplified way [34, 35, 36]:

$$\mathcal{A}_{f_{CP}}(t) = S_{f_{CP}} \sin(\Delta M t) - C_{f_{CP}} \cos(\Delta M t)\,, \tag{1.25}$$

where

$$S_{f_{CP}} \equiv \frac{2Im\lambda_f}{1+|\lambda_f|^2}\,, \qquad C_f \equiv \frac{1-|\lambda_f|^2}{1+|\lambda_f|^2}; \tag{1.26}$$

with no *direct* and *indirect* CP violation ($|\bar{A}_f/\bar{A}_f| = 1$ and $|q/p| = 1$) we get $C_f = 0$, but CP violation could occur if $Im\lambda \neq 0$.
SM foresees $|\lambda| \simeq 1$ and from equations (3.26 in Appendix A), (1.18) we can obtain, with good accuracy,

$$\lambda_f = -\eta_f \frac{M_{12}^* A e^{i(-\phi+\delta)}}{M_{12} A e^{i(\phi+\delta)}} \tag{1.27}$$

and, writing $M_{12} = |M_{12}|e^{i\phi_M}$, we get:

$$\lambda_f = e^{-2i(\phi-\phi_M)} \tag{1.28}$$

from which it is possible to write (1.25)

$$\mathcal{A}_{f_{CP}}(t) = -Im\lambda_f \sin(\Delta M t) = \eta_f \sin(2\Phi)\sin(\Delta M t)\,, \tag{1.29}$$

where $\Phi = \phi - \phi_M$.
The $B_s^0 \to D_s^{\mp}K^{\pm}$ decay leads to the possibility of CP violation in the interference between mixing and decay since both B_s^0 and $\bar{B}_s^0$ can decay directly to the same final state. This decay goes through two tree-level diagrams and, thanks to this fact, the theoretical uncertainty on the CP observables in terms of the γ angle is very small: $|\delta\gamma| \lesssim \mathcal{O}(10^{-7})$ [41]. So the measurement of CP violation in this decay gives an efficient measurement of the γ angle.

1.5.2 Decay studies

Particle physics could also be tested by the study of those processes that are highly suppressed in SM. An example is given by the Flavor Changing Neutral Current (FCNC) process: transitions that change the flavor of a fermion current without altering its electric charge. According to SM, these kind of precesses can occur only through the GIM (Glashow-Iliopoulos-Maiani) [42]: via suppressed box diagrams and penguin (loop) diagrams. One example of such processes is the rare decay $B_s^0 \to \mu^+\mu^-$ (figure 1.11). Such decay is characterized by a purely leptonic final state, so precise predictions of its branching fraction, $\mathcal{B}(B_s^0 \to \mu^+\mu^-) = (3.23 \pm 0.27) \times 10^{-9}$ [43], is possible. This rare decay could be considered as a strong evidence of physics beyond SM: in presence of *New Physics* (NP) additional contributions of new particles, which are not permitted in SM, could happen in loop level [44].
In this system the value $\Delta\Gamma_s \equiv \Gamma_H^{(s)} - \Gamma_L^{(s)}$ is expected to be large and leads to a complicated extraction of branching ratio values for B_s meson decays: systematic biases will be of the order of $\mathcal{O}(10\%)$, depending on the dynamics of the specific decay [45].
Previous searches, made by D0 and CDF at the Fermilab and then by ATLAS, CMS and LHCb at LHC, constrained the possible SM deviation: the lowest limit of $\mathcal{B}(B_s^0 \to \mu^+\mu^-) < 4.5 \times 10^{-9}$ at 95% confidence level was obtained by the LHCb collaboration with data collected in 2011 [46].

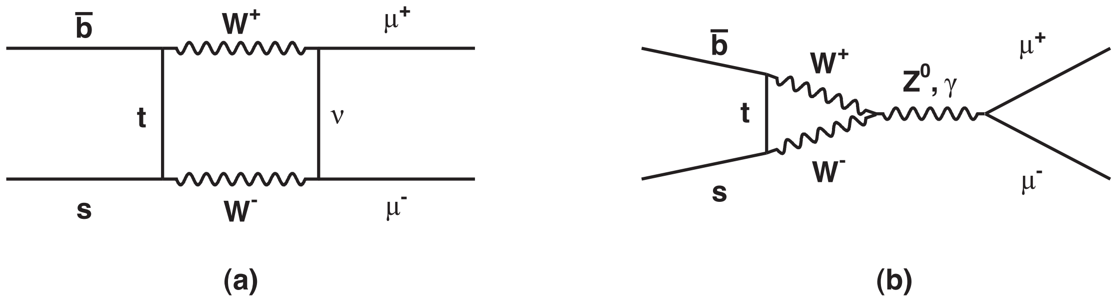

Figure 1.11: Feynman diagrams for the $B_s^0 \to \mu^+\mu^-$ process: (a) box diagram, (b) penguin diagram.

The LHCb experiment has recently made the first observation of this decay using data collected both in 2011 and 2012 [47]. This leads to $\mathcal{B}(B_s^0 \to \mu^+\mu^-) = (3.2^{+1.5}_{-1.2}) \times 10^{-9}$ which is in agreement with the SM prediction.

1.5.3 Mass measurements

A basic property of hadrons that can be compared to theoretical predictions is their masses: for this reason precision measurements of hadron masses have been performed in recent years by several experiments. The most of such measurements concerned B mesons whereas, in contrast, few precision D meson mass measurements existed.
Thanks to LHCb experiment, in the last years several b and c hadron masses have been measured allowing us to achieve results more precise than in the past.
B mesons masses' measurements are performed with the exclusive decay modes [95] [99], b baryons masses were studied from decays to J/ψ meson [97] and D^0 meson from semileptonic b-hadron decay [120]. In the table 1.4 the list of the last hadron mass measurements is shown.

Since quarks are confined inside hadrons and are not observed as physical particles, it is not possible to measure quark masses directly: the only way to get their values is to determinate them in an indirect way, through the hadronic properties. Looking at the mass of hadrons, it can be realized that the whole mass is almost totally made up by interacting energy. An example is given by the proton mass: a proton is composed by 2 u quarks and by 1 d quark having a total mass about 10 Mev/c^2 while the proton mass is about 1000 Mev/c^2. So, hadron masses and any

Table 1.4: Summary of LHCb precise hadron mass measurements

Particle	**Decay mode**	**mass (MeV/c^2)**
B^+	$B^+ \to J/\psi K^+$	$5279.38 \pm 0.11_{stat} \pm 0.33_{syst}$ [95]
B^0	$B^0 \to J/\psi K^{(*)0}$	$5279.58 \pm 0.15_{stat} \pm 0.28_{syst}$ [95]
B_s	$B_s \to J/\psi \phi\phi$	$5367.08 \pm 0.38_{stat} \pm 0.15_{syst}$ [95]
Λ_b^0	$\Lambda_b^0 \to J/\psi \Lambda$	$5619.53 \pm 0.13_{stat} \pm 0.45_{syst}$ [97]
Ξ_b^-	$\Xi_b^- \to J/\psi \Xi^-$	$5795.8 \pm 0.9_{stat} \pm 0.4_{syst}$ [97]
Ω_b^-	$\Omega_b^- \to J/\psi \Omega^-$	$6046.0 \pm 2.2_{stat} \pm 0.5_{syst}$ [97]
D^0	$D^0 \to K^+K^-K^-\pi^+$	$1864.75 \pm 0.15_{stat} \pm 0.11_{syst}$ [120]

matrix element between hadronic state can not be treated in perturbative way and non-perturbative calculation techniques have been developed. Lattice QCD (LQCD) provides a non-perturbative tool for calculating the hadronic spectrum and the matrix elements of any operator.
According to Lehmann-Symanzik-Zimmermann (LSZ) formalism developed in the 1955, the physical S matrix elements (scattering amplitudes) can be extracted by appropriate T-ordered correlation functions of the theory.
Let the correlator in the Minkowski metric be:

$$T \langle 0| \widehat{O}_1(x)\widehat{O}_2(0) |0\rangle = \vartheta(tx) \langle 0| \widehat{O}_1(x)\widehat{O}_2(0) |0\rangle + \vartheta(-tx) \langle 0| \widehat{O}_2(0)\widehat{O}_1(x) |0\rangle \quad (1.30)$$

where

$$\widehat{O}(x) = \mathrm{e}^{-i\widehat{p}_\mu x^\mu}\ \widehat{O}(0)\ \mathrm{e}^{+i\widehat{p}_\mu x^\mu}, \quad (1.31)$$

with

$$\mathrm{e}^{i\widehat{p}_\mu x^\mu} = \mathrm{e}^{i\widehat{H} - i\widehat{\mathbf{p}}\cdot\mathbf{x}}. \quad (1.32)$$

The Euclidean formulation of the equation 1.31 is obtained considering the correlator of operator $\widehat{O}_1$ at time 0 with operator $\widehat{O}_2$ at imaginary time $t = i\tau$. So the operator can be written as:

$$\widehat{O}(x) = \mathrm{e}^{t\widehat{H}}\mathrm{e}^{i\widehat{\mathbf{p}}\cdot\mathbf{x}}\ \widehat{O}(0)\ \mathrm{e}^{-t\widehat{H}}\mathrm{e}^{-i\widehat{\mathbf{p}}\cdot\mathbf{x}}. \quad (1.33)$$

The change from real to imaginary time is often referred to as *Wick rotation*.
Let be for $tx > 0$:

$$\begin{aligned} f(x) &= \langle 0| \mathrm{e}^{t\widehat{H}}\mathrm{e}^{i\widehat{\mathbf{p}}\cdot\mathbf{x}}\ \widehat{O}_1(0)\ \mathrm{e}^{-t\widehat{H}}\mathrm{e}^{-i\widehat{\mathbf{p}}\cdot\mathbf{x}}\ \widehat{O}_2(0) |0\rangle = \\ &= \langle 0| \widehat{O}_1(0)\ \mathrm{e}^{-t\widehat{H}}\mathrm{e}^{-i\widehat{\mathbf{p}}\cdot\mathbf{x}}\ \widehat{O}_2(0) |0\rangle . \end{aligned} \quad (1.34)$$

In the 3-momentum space the last equation transforms as:

$$f(t, \mathbf{p}) = \langle 0| \widehat{O}_1(0)\ \mathrm{e}^{-t\widehat{H}}(2\pi)^3\delta(\widehat{\mathbf{p}} - \mathbf{p})\ \widehat{O}_2(0)\,|0\rangle\,. \tag{1.35}$$

Since the unit operator $\mathbb{I}$ can be written in terms of the vectors of a complete orthonormal basis as

$$\mathbb{I} = \Sigma_n\,|E_n\rangle\,\langle E_n|\,,$$

and the spectrum of the Hamiltonian is discrete since the lattice has a finite volume ($\mathbf{p} = \frac{2\pi\mathbf{n}}{L}$), it is possible to write the equation 1.35 as:

$$f(t) = \Sigma_n\,\langle 0|\,\widehat{O}_1(0)\,|E_n\rangle\,\langle E_n|\,\widehat{O}_2(0)\,|0\rangle\ \ \mathrm{e}^{-tE_n}. \tag{1.36}$$

For $\mathbf{p} = 0$ and in the limit $t \to \infty$ one obtains:

$$f(t) = \langle 0|\,\widehat{O}_1(0)\,|E_0\rangle\,\langle E_0|\,\widehat{O}_2(0)\,|0\rangle\ \ \mathrm{e}^{-tE_0} + \mathcal{O}(\mathrm{e}^{-t(E_1-E_0)})\ , \tag{1.37}$$

where $\langle 0|\,\widehat{O}_1(0)\,|E_0\rangle \neq 0$.
In case of B charged meson the operators can be written as $\widehat{O}_1 = \widehat{O}_{B^+}$ and $\widehat{O}_2 = \widehat{O}^\dagger_{B^+}$; while the mass is given by the slope of the dominant part of the equation 1.37, that is the energy E_0: $E_0 = m_{B^+}$.
$\widehat{O}_{B^+}$ can be one of the infinite pseudoscalar operators having beauty number equal to 1, such as $\bar{b}(0)\gamma_5 u(0)$ or $\bar{b}(0)\gamma_5 u(0)\bar{s}s$ etc.
The Euclidean correlator can be numerically computed as a path integral which is an integral over all possible configurations of the field Φ.

The fundamental result of LQCD is then obtained:

$$T\,\langle 0|\,\widehat{O}_1(x)\widehat{O}_2(0)\,|0\rangle = \int \mathcal{D}[\Phi]\mathrm{e}^{-S[\Phi]}O_1[\Phi(x)]O_1[\Phi(0)] \tag{1.38}$$

The crucial point is that the left-hand side is formulated in the operator language of quantum field theory while the right-hand side is not expressed in terms of field operators.
In the integrand, the two operators $\widehat{O}_i$ are translated to functionals O_i of the fields and then weighted with the Boltzmann factor containing the classical Euclidean action $S[\Phi]$: the integral can be evaluated numerically on the lattice.
Lattice calculation can be summarized in the following steps:

- The functional integral is computed numerically.
- A lattice spacing and a finite volume is introduced (figure 1.12).

- The numerical integration over a huge (but finite) number of variables is done with a Markov chain Monte Carlo.

- Numerical calculation is unavoidably affected by systematic errors: limited statistics, finite lattice spacing, finite volume, unphysical values of quark masses (u, d too light and b too heavy on current lattices).

- Systematic errors are quantified and removed by extrapolating the numerical results: continuum limit, infinite volume limit, extrapolation to physical values of quark masses.

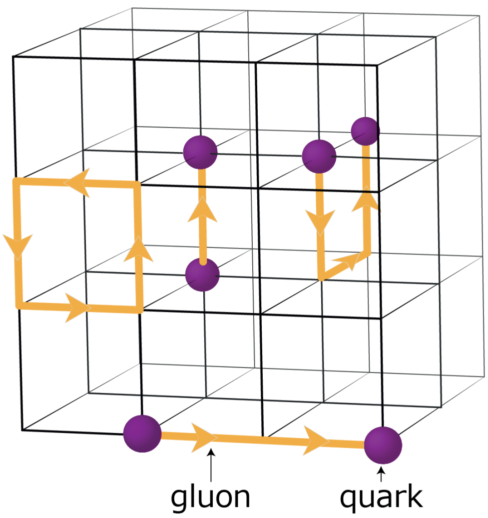

Figure 1.12: QCD Lattice sketch.

Example of extraction of a meson mass from a two-point correlator is visible in figure 1.13, while b quark mass calculations with integral evaluated for different quark field numbers ($N_f = 2$ (ud), $N_f = 2 + 1$ (uds), $N_f = 2 + 1 + 1$ ($udsc$)) is shown in figure 1.14.

This procedure is not trivial in case of the B^+ meson: being a the lattice spacing, the condition $am_{quark} > 1$ is not verified since $am_b << 1$. The present LQCD uses values in the range of $1/a = 2 - 4$ GeV ($a \approx 0.1 - 0.05$ fm) which works fine with light quarks (u, d and s). For the high mass bottom quark approaches like Non-Relativistic QCD (NRQCD) (the spectroscopy of mesons containing at least one b or c quark is summarized in figure 1.15 [56]) or Heavy Quark Effective Theory (HQET) are used.

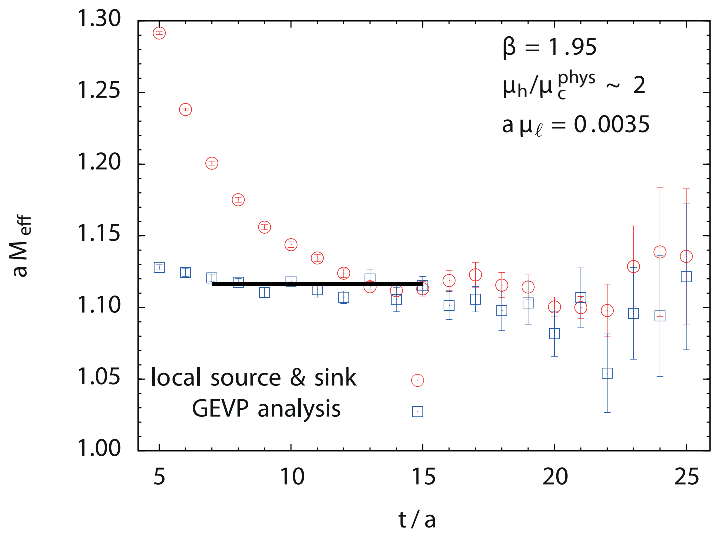

Figure 1.13: Plot of extraction of a meson mass from a two-point correlator.

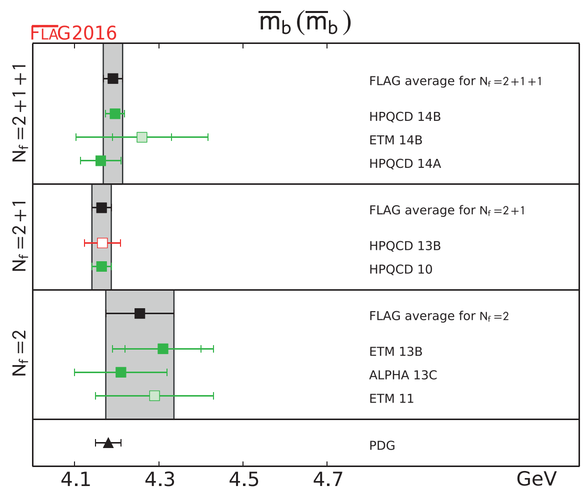

Figure 1.14: b quark mass calculations review.

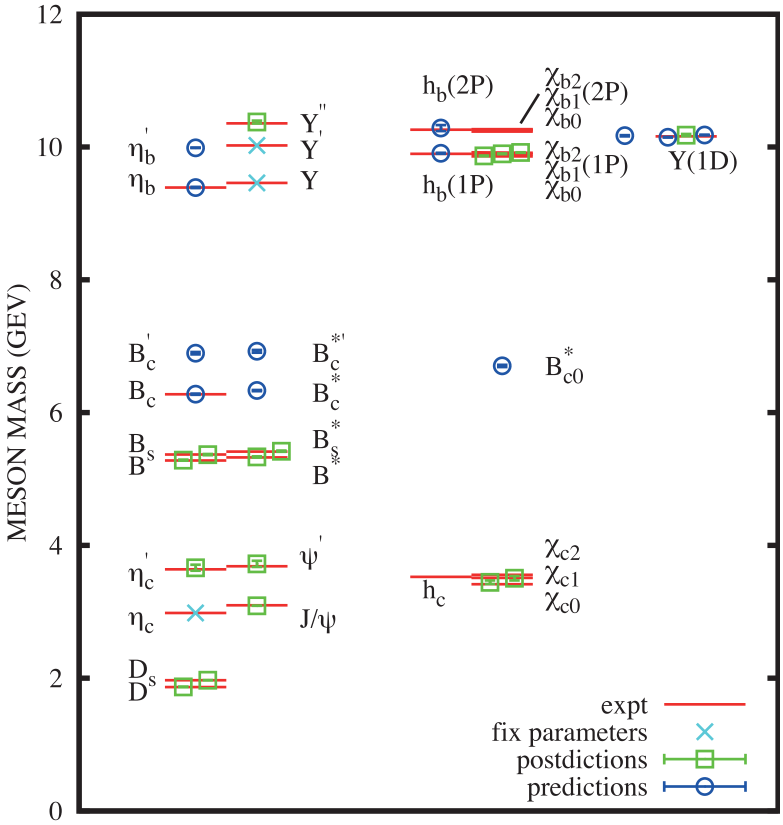

Figure 1.15: Spectroscopy of mesons containing at least one b or c quark.

The fundamental request is that LQCD predictions have to match experimental data if QCD is the correct theory of strong interactions. In figure 1.16 a summary of lattice spectroscopy of light hadron provided by A. Kronfeld [93] is shown.

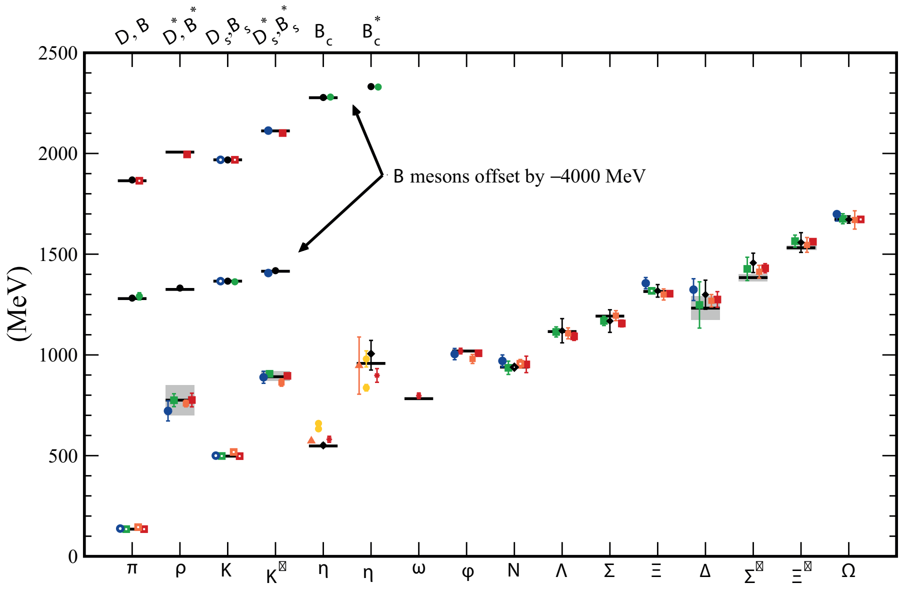

Figure 1.16: Spectroscopy of hadron from lattice QCD. b-flavored meson masses are offset by -4000 MeV. Details are reported in [93].

In order to improve the precision of calculations and to reduce the errors of the analysis, a variety of calculation are used and independent measurements have to be made by different groups. Furthermore, experimental precise measurement of B meson mass will be needed as the CPU power calculation will be improved.
Another point of interest is given by values of B charged and B neutral masses reported in table 1.4. As for protons and neutrons, charged and neutral B mesons differ each other from a u quark becoming a d and they form an isospin doublet. Since strong interaction preserve the isospin, the mass difference between the members of the same multiplet is given by electromagnetic interaction only. Presently the difference is less than experimental errors. An improvement on B meson mass measurement precision could lead to the measure of $B_{charged} - B_{neutral}$ mass difference.
The objective of this thesis is to give an improved measurement of the charged B meson mass.

1.6 The Large Hadron Collider

The *Large Hadron Collider* (LHC) [62], built at CERN Laboratories, is an high luminosity collider and it is the world's largest and most powerful proton-proton collider. It has about 27 Km circumference and it is designed to reach center of mass energy of about $\sqrt{s} = 14$ TeV. The four main experiments located at LHC are ATLAS, CMS, LHCb and ALICE, which are placed in the four interaction points of the proton beams (figure 1.17). ATLAS [63] and CMS [64] are two experimental

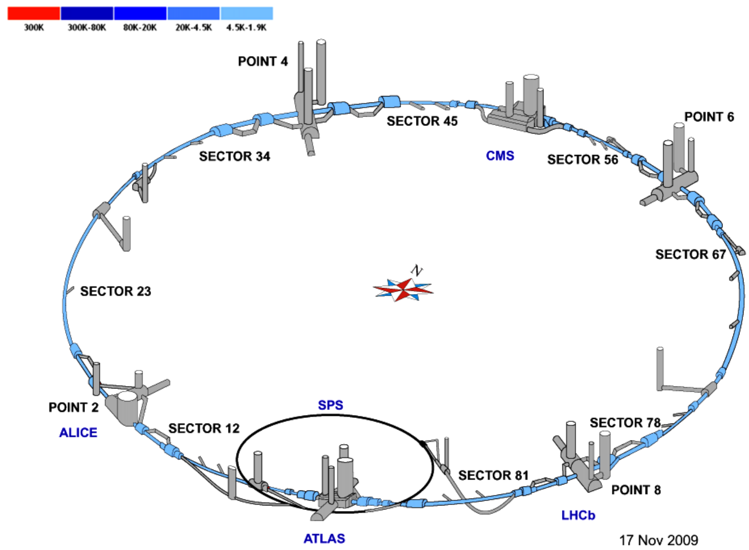

Figure 1.17: Draft of LHC complex

apparatus designed to study physics at high transverse momentum. Their attention is mainly oriented to Higgs Boson studies and to the production of new particles not foreseen by SM. ALICE [65] studies high energy heavy-ion (Pb-Pb nuclei) collisions. LHCb [66] is devoted to heavy quark studies, mainly b physics.
The main LHC features are listed in table 1.5:
LHC is located beneath the Franco-Swiss border at about 100 m underground in the same tunnel that was used for the previous LEP collider (figure 1.18). It consists of two parallel vacuum tubes, where the two proton beams are accelerated in opposite directions. In order to keep protons in the rotation orbit, an high strength magnetic field is needed: 1232 superconductor magnetic dipoles generate up to 8 T magnetic field working at 1.9 K temperature.

Table 1.5: main LHC features summary table [62]

$\sqrt{s}$	14 TeV
circumference	26.7 km
$f_{bunch\ crossing}$	40 MHz
design luminosity ($\mathcal{L}$)	10^{34} cm^{-2}s^{-1}
ATLAS, CMS luminosity	10^{34} cm^{-2}s^{-1}
LHCb luminosity	2×10^{32} cm^{-2}s^{-1}
$\sigma_{tot.}$	100 mb
$\sigma_{inel.}$	80 mb
$\sigma_{b\bar{b}}$	500 μb
$\sigma_{b\bar{b}}/\sigma_{inel.}$	6×10^{-3}

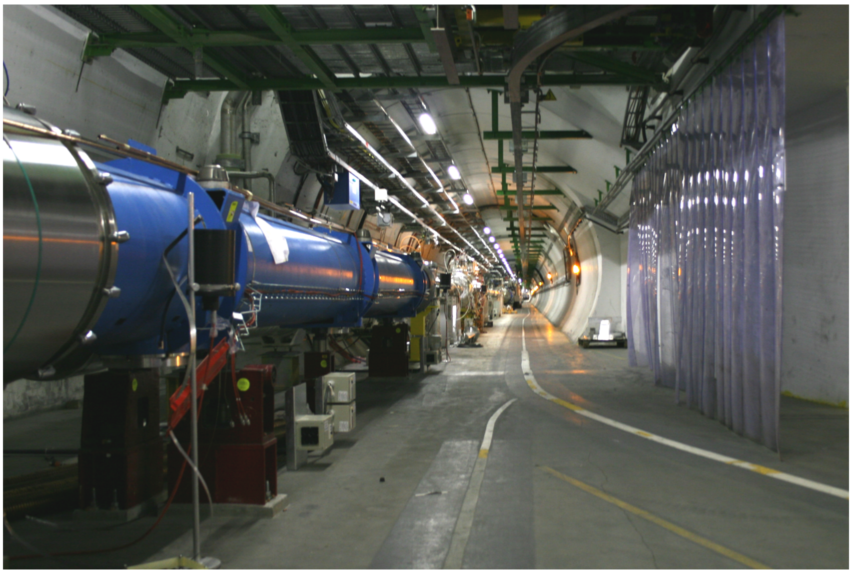

Figure 1.18: Underground tunnel of the LHC collider

The proton accelerating process consists of different steps (figure 1.19): protons are extracted from hydrogen atoms after a ionization process. These are then injected in the *PS Booster* (*PSB*) at 50 MeV energy by the *Linac 2*. Then the *Booster* accelerates them to 1.4 GeV. Beams go now through the *Proton Synchrotron* (*PS*), where they are accelerated to 25 GeV energy. They are further accelerated by the *Super Proton Synchrotron* (*SPS*) to 450 GeV. Finally they are injected into LHC, where they are accelerated to their nominal energy. Both beams are composed by

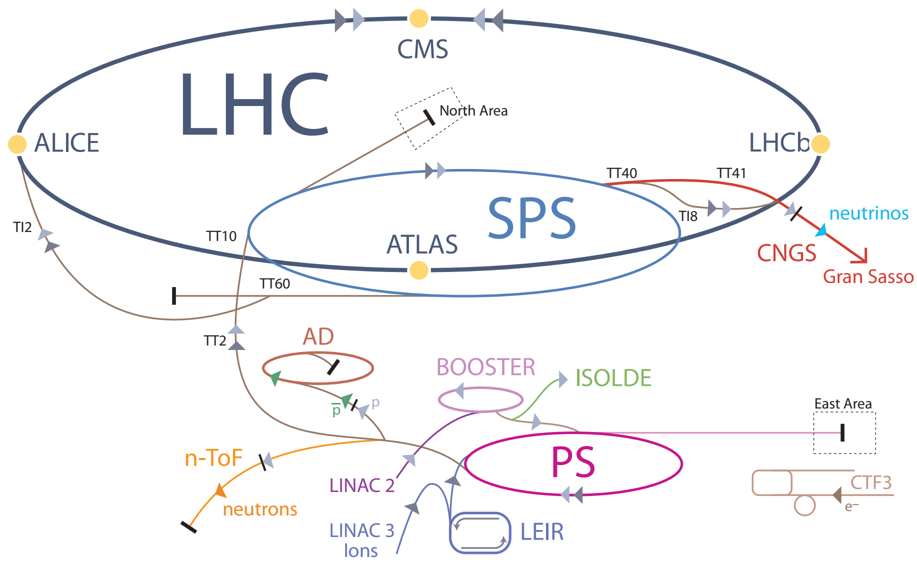

Figure 1.19: Protons accelerating process sketch

10^{11} proton bunches and, given a bunch crossing frequency of 40 MHz at 7 TeV energy per beam, it is possible to estimate the number $\mathcal{N}$ of interactions for a single crossing:

$$\mathcal{N}_{\text{LHC}} = \frac{\sigma_{inel.}\,\mathcal{L}_{\text{LHC}}}{\text{f}_{bunch\ crossing}} = \frac{(80 \times 10^{-27})\ \text{cm}^2 \times 10^{34}\ \text{cm}^{-2}\text{s}^{-1}}{40 \times 10^6\ \text{s}^{-1}} \simeq 20\,. \tag{1.39}$$

Since LHCb's luminosity is 50 times lower then LHC's (table 1.5), we get the interactions number for LHCb as:

$$\mathcal{N}_{\text{LHCb}} = \frac{\sigma_{inel.}\,\mathcal{L}_{\text{LHCb}}}{\text{f}_{bunch\ crossing}} \simeq \frac{20}{50} = 0.4\,, \tag{1.40}$$

that leads to a mean value of about 2 interactions per 5 intersections. Such a difference between other experiments and LHCb, in number of interactions, rises because

LHCb detects particles with small solid angle, where the background is at the maximum level. Therefore, in order to reduce the number of recorded events, a reduction of luminosity is needed. Both ATLAS and CMS do not have this kind of problem, because they are designed to detect particles with high transverse momentum: in this way a remarkable amount of background signal is removed by construction. Reducing luminosity in LHCb, moreover, allows the reduction of particles track multiplicity and allow preserving the instrumentation from radiation damages.
For what concerns LHCb, the number of pairs $b\bar{b}$ is given by:

$$\mathcal{L}_{\mathrm{LHCb}} \times \sigma_{b\bar{b}} = 10^5 \ \mathrm{s}^{-1} \ , \tag{1.41}$$

that correspond to 3×10^{12} pairs per year.

Chapter 2

The LHCb experiment

2.1 The LHCb detector

The LHCb [66] experiment is a forward spectrometer (figure 2.1) designed to take advantage of the characteristic $b\bar{b}$ pair angular distribution. The detector is set in a pre existing cavern where the interaction point is shifted of about 11 m from the cavern center itself. In this way the detector length is about 20 m and the total dimensions are about $6 \times 5 \times 20$ m^3.
The horizontal angular acceptance, given by the magnet geometry, has a range from 10 mrad to 300 mrad in the beam bending vertical plane (xz) (figure 2.2) and from 10 mrad to 250 mrad in the non-bending plane (yz) (figure 2.1). With such acceptance the detector is able to reconstruct about 20% of all $b\bar{b}$ produced.
According to the LHCb cartesian coordinate system, the nominal collision point is located at $z = 0$. The detector region before the magnet centered at $z_m \simeq 5$ m is referred to as *upstream*, whereas the region after the magnet is said *downstream*.
b and c hadrons decays are measured by a precise tracking system that is located in the region from $z \simeq 1$ m and $z \simeq 9$ m. The proper time is obtained by measuring the distance between the collision point, that define the Primary Vertex (PV), and the decay vertex according to $t = \frac{L}{\beta\gamma c}$, where L is the distance between the PV and decay vertex, as an example in the case of B mesons $L \simeq 7$ mm, while β and γ are the relativistic factor of the particle.
By means an high precision measurement of the daughter particles the hadron mass reconstruction is obtained: this is achieved by the *upstream* and the *downstream* track reconstruction.
LHCb tracking system [67] consists of a vertex locator (VELO) [75], situated around the interaction region centered at $z = 0$, and four planar tracking stations: the Trig-

ger Tracker, upstream of the dipole magnet, and three tracking stations T1-T3 downstream of the magnet.
T1-T3 stations consist of an Inner Tracker (IT), located at the center of the stations and close to the beam pipe, and of an Outer Tracker (OT) for the outer parts: a minimum momentum of 1.5 GeV/c is needed to reach the tracking stations [68].

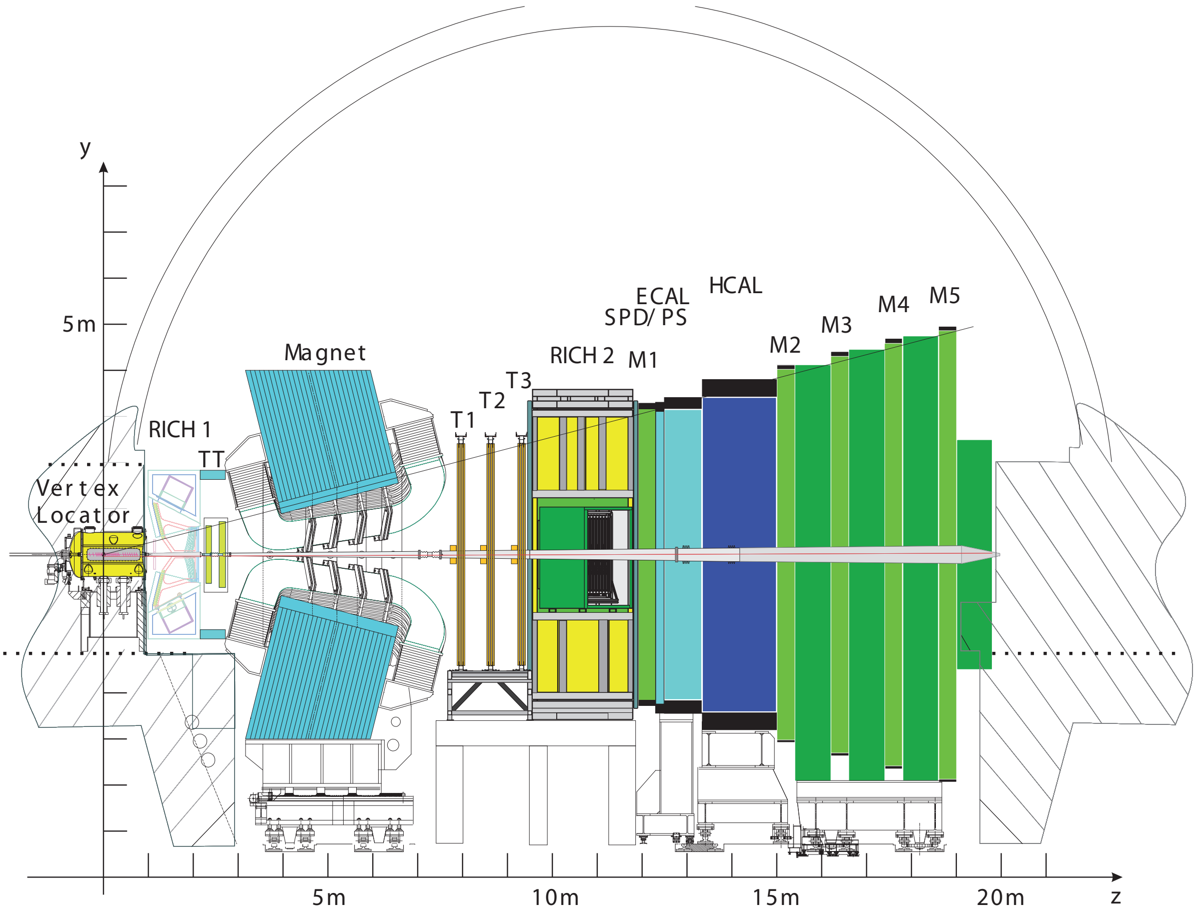

Figure 2.1: The LHCb detector: side view

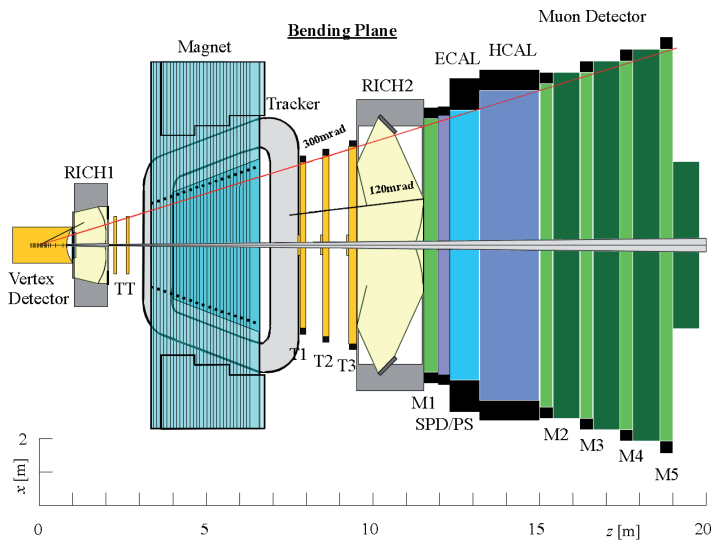

Figure 2.2: The LHCb detector: top view

The dipole magnet [76] produces a magnetic field with vertical orientation that is able to bend charged particles in the xz plane and has a basic role for particles momentum measurement.

For the particle identification the following detectors are used: two Ring Imaging Cherenkov (RICH1 e RICH2) [70] for K/π discrimination; a calorimetric system [71] made by a scintillator and a *Preshower* (SPS/PS) detector for charged particles identification, electron-gamma and electron-hadron discrimination; a electromagnetic calorimeter (ECAL) for electron and positron energy reconstruction; an hadronic calorimeter (HCAL) for identification and reconstruction of energy and position of hadrons; and finally a muon system [72, 73, 74] (M1, M2, M3, M4, M5) for identification and reconstruction of muon tracks.
The different stages will be briefly described in the next sections.

2.2 Tracking system

2.2.1 Dipole magnet

In order to measure the particles momentum a warm dipole magnet is used (figure 2.3). The dipole magnet acceptance is ± 250 mrad in the vertical plane and ± 300 mrad in the horizontal one. The magnetic field strength, $\int$ Bdl $= 4$ Tm till to 10 m from the interacting point, was chosen in order to have a value of 2 Tm maximum in the RICH and in order to maximize its value in the region between VELO and TT. A warm magnet was chosen for the cost effectiveness and the time constraints involved in building a superconducting magnet.

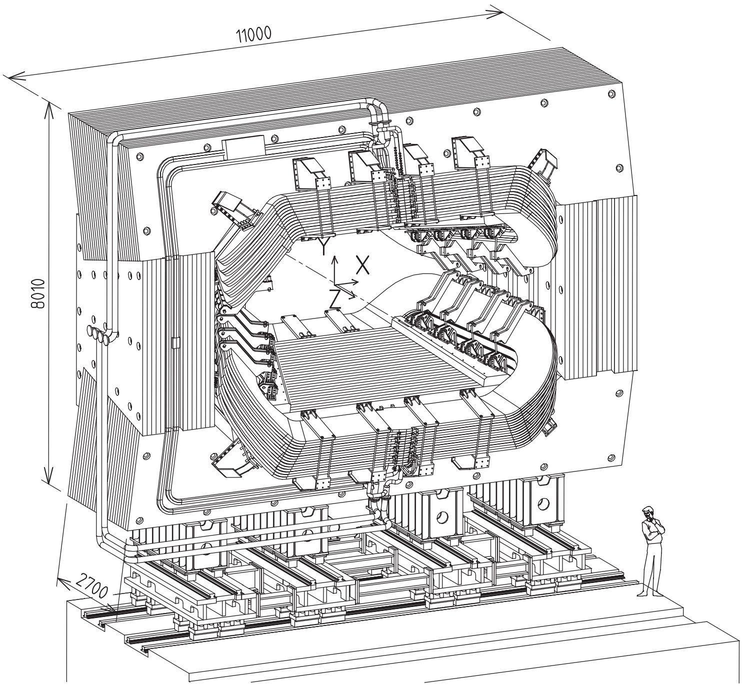

Figure 2.3: Dipole magnet sketch

2.2.2 Vertex Locator

The VELO (figure 2.4) provides precision measurements of the tracks near the interaction region. Cylindrical coordinates (r, ϕ, z) are used. The VELO is used to reconstruct the production and decay vertex of b and c hadrons, to provide accurate measurements of their mean life and to measure the impact parameter of the various tracks related to the PV.
It is able to detect particles with pseudorapidity in the range $1.6 < \eta < 4.9$ and coming from PV in the range $|z| < 10.6$ cm, to cover the downstream detector geometric acceptance.

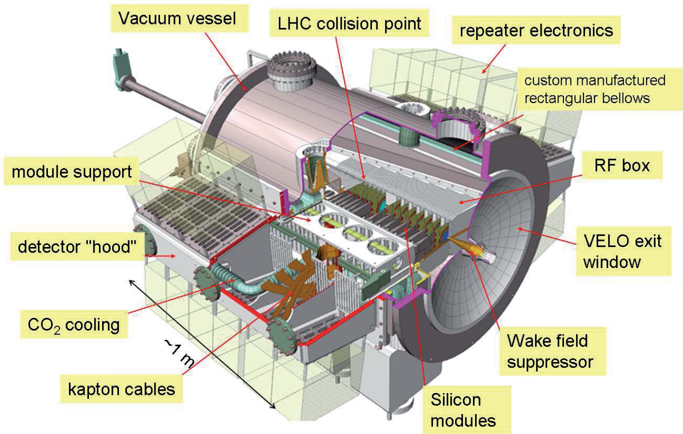

Figure 2.4: VELO sketch

The VELO consists of two halves each containing 21 modules. Each module is made up of two silicon half discs, of 300 μm thickness, with strips in either radial, r, or polar, ϕ, coordinates (figure 2.5). According to simulations, cylindrical geometry is used in order to achieve a fast track and vertex reconstruction in the trigger.

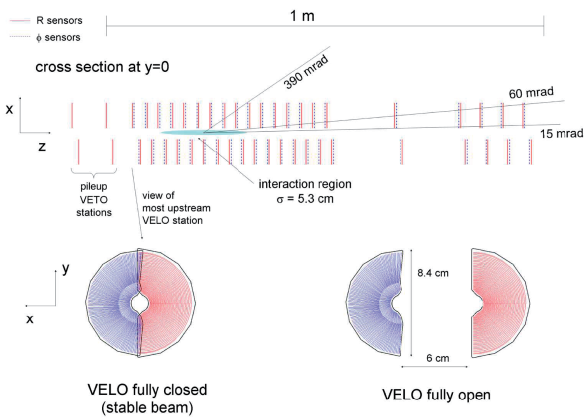

Figure 2.5: VELO silicon sensors Section on (x, z) plane and single module section on (x, y) in open and closed position

Since vertex reconstruction is fundamental for LHCb experiment, the VELO has to satisfy strict performance parameters:

- 4 μm cluster spatial resolution for 100 mrad tracks at the lowest inter-strip pitch of 40 μm. This is crucial to reach good performances in impact parameter measurement,
- the material in front of the detector has to be the minimum as possible in order to reduce the multiple scattering: in order to satisfy such request the VELO has to be placed the closer as possible to the beam pipe (about 8 mm) minimizing the material budget.

Silicon sensors operate inside a so called *roman pot* [69] in a secondary vacuum instead of the one in which the beams circulate, where the pressure less than 10^{-8} mbar. In order to minimize the damage by irradiation and to dissipate the heat produced, a cooling system is installed on VELO. Such a system is able to keep the temperature in a range between -10 to 0 °C. Furthermore, the silicon discs and the frontend electronics is shielded by an aluminium layer of 300 μm thickness (*RF foil*).

2.2.3 Silicon Tracker

The Silicon Tracker (ST) is made up by two detectors: the TT [77] and the IT [78], the TT is made up by 500 μm thick microstrips while the IT by either 320 μm and 410 μm.
The TT station has a double function: together with VELO, it is used at trigger level to make transverse momentum measurements and it is used for tracking in the event reconstruction phase.
The TT is located after the VELO and just after the RICH1 where there is a residual magnetic field able to deflect charged particles and to make momentum measurement possible with precision about 20-30%. TT is composed by four stations grouped as two, called TTa and TTb, space by 30 cm (figure 2.6). Each module is constructed from four layers of silicon strip sensors that with a rectangular area of 150 cm wide and 130 cm high cover the total LHCb acceptance (figure 2.7). The strips of the first and the fourth stations lay in the vertical xy plane and measure the bending x coordinate, while the ones of the second and the third have a stereo angle of $+5°$ and $-5°$ respectively.
The IT is used in the regions close to the beam pipe, where the particle rate is higher. It makes up the inner region of the three downstream tracking stations,

T1-T3, situated beyond the magnetic field region just before RICH2. Each station consists in four overlapped silicon layers with two of these that are rotate by a stereo angle of $\pm 5°$ and two that are aligned to the y axis. Each layer is made up by four independent modules placed around the beam pipe, covering about a 120×40 cm^2 area (figure 2.8).

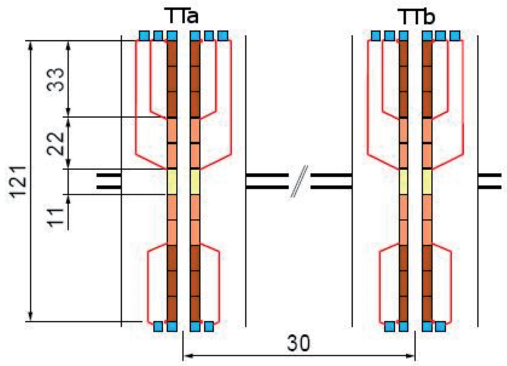

Figure 2.6: TTa and TTb sketch

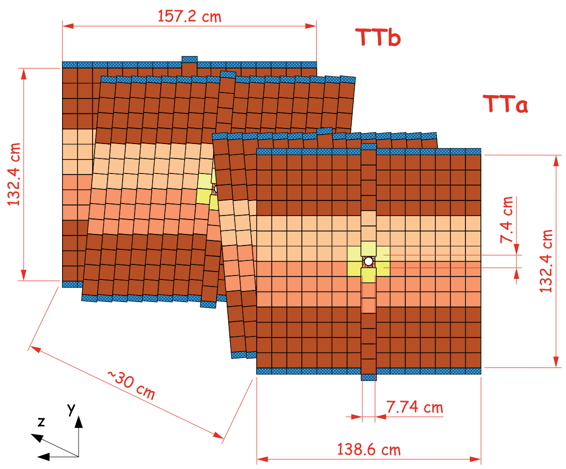

Figure 2.7: TT frontal view sketch. The strip arrangement is shown: on the left strips parallel to vertical y axes, on the right strips $5°$ rotated.

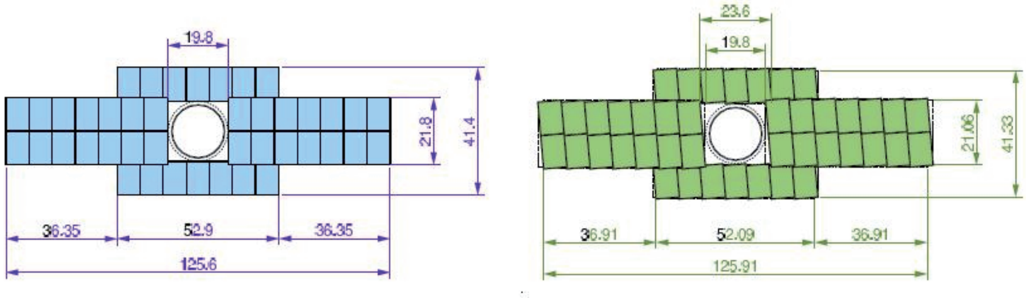

Figure 2.8: IT stations (x, y) plane sketch. On the left a x type chamber with strip parallel to y axes is shown; on the right a u, v type chamber with strip 5° angle with respect vertical direction rotated.

The main features for the ST are listed:

- Spatial resolution: about 50 μm per hit both for TT and IT, with strip pitch about 200 μm for both.
- Hit occupancy: the average occupancy in the TT, and similarly in the IT, varies between 1.9% for the inner sectors to 0.2% for the outermost modules.
- The frontend electronics is able to form signals within 25 ns in order to avoid overlapping between consecutive bunches.
- As VELO is, both TT an IT are placed in a high particles rate region too. To minimize radiation damages, sensors will work at 5° C temperature.

2.2.4 Outer Tracker

The OT is a drift-time detector [79] used for charged particles tracking and momentum measurement in a wide acceptance range. The OT is made by straw tubes drift chambers with the internal diameter of 4.9 mm filled with Ar/CO_2 gas mixture with ratio $70-30$ that provides 50 ns time resolution and 200 μm spatial resolution with 10% maximum occupancy. The detector is composed by three stations made up by four modules (figure 2.9). In the first and third module the straw tubes are aligned to the vertical y axis while in the third and fourth ones they have a stereo angle of $\pm 5°$. The total active area is about 5971×4850 mm^2 and the acceptance is 300 mrad in the horizontal plane and 250 mrad in vertical one.

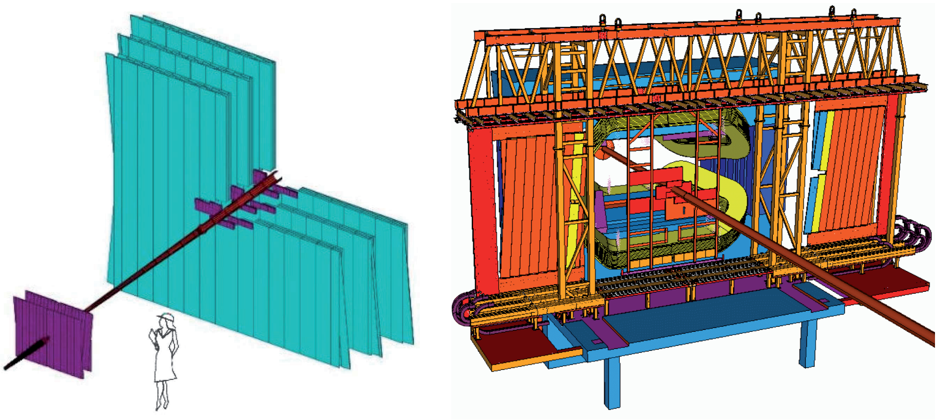

Figure 2.9: OT module arrangement on the left, frontal sketch view with modules open on the right (on the left in violet the IT is shown).

2.3 Track reconstruction

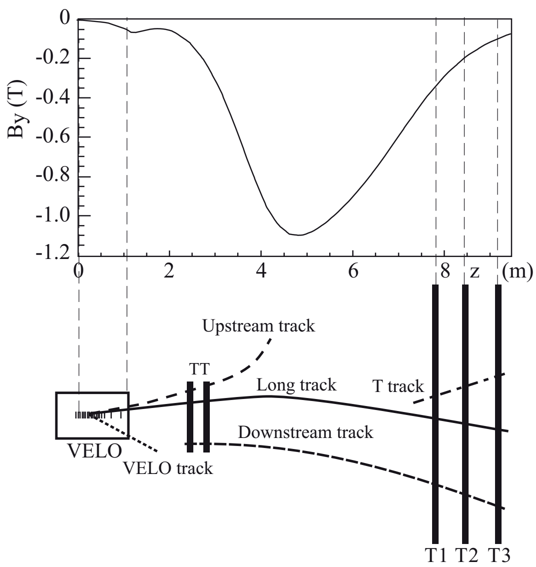

Figure 2.10: Schematic illustration of the various track types

Tracks of particles are reconstructed from hits in VELO, TT, IT and OT detectors. Depending on their paths through the detectors, the following track types are defined (figure 2.10):

- **Long tracks**: traverse the full tracking system with hits in VELO, T stations and optionally in TT. They have the most precise momentum measurement.
- **Upstream tracks**: pass only through the VELO and TT stations. Their momentum is too low to traverse the magnet and reach the T stations. They are therefore also used to understand backgrounds in the particle identification algorithm of the RICH.
- **Downstream tracks**: pass only through the TT and T stations. They are used to reconstruct long lived particles like K_s.
- **VELO tracks**: pass only through the VELO. They are useful for the primary vertex reconstruction.
- **T tracks**: pass only through the T stations. They are typically produced in secondary interactions, but are useful for RICH2 particle identification.

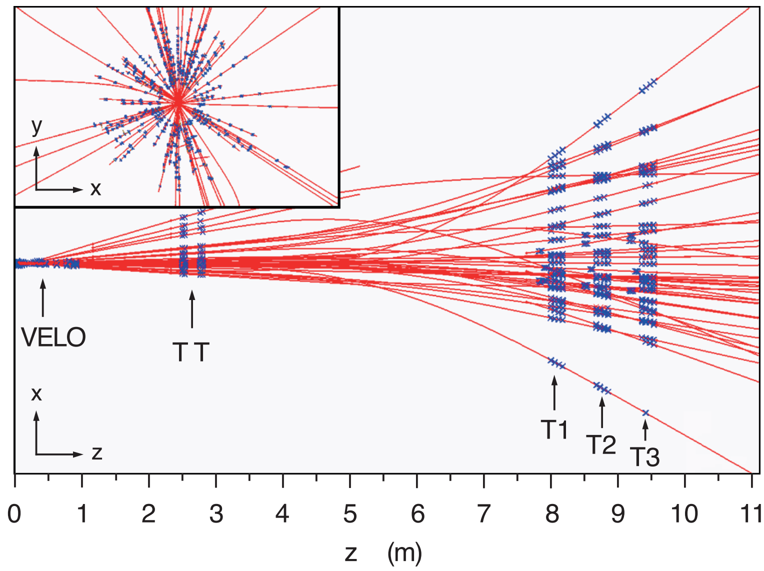

Figure 2.11: Display of reconstructed tracks and assigned hits in an event in the x-z plane [80]. On the top left a zoom of the VELO region in the x-y plane is shown.

2.4 Particle identification

Particle identification (PID) is a fundamental requirement of the LHCb experiment in order to distinguish the large number of b hadron decays.
In many interesting b hadron decays there are pions and kaons: for example $B^0 \to \pi^+\pi^-$, $B^0 \to K^+K^-$, $B^0 \to K^+\pi^-$. In these decays the identification of even just one of the particles is a powerful means to discriminate one decay from another. The importance of PID rises for example in the study for physics beyond SM in the flavor sector where charmless $H_b \to h^+h'^-$ decays are considered [81] (H_b is a b-flavoured meson or baryon and h h' could be a pion, a kaon or a proton).
In figure 2.12 the invariant mass distribution for $B \to h^+h^-$ is shown: LHCb data before the use of the RICH information (*left*) and after applying RICH particle identification (*right*).

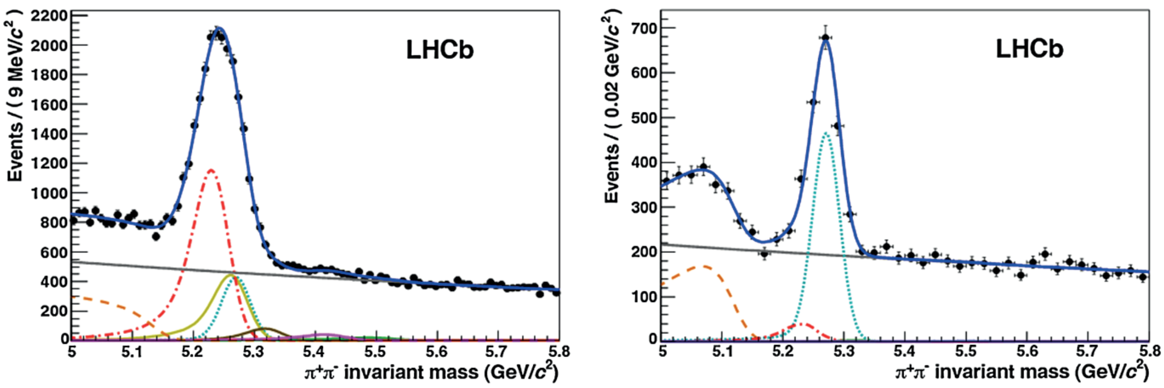

Figure 2.12: Invariant mass distribution for $B \to h^+h^-$ in the LHCb data before the use of the RICH information (*left*), and after applying RICH particle identification (*right*). $B^0 \to \pi^+\pi^-$ signal is shown (turquoise dotted line). The contributions from different b-hadron decay modes are eliminated by positive identification of pions, kaons and protons and only the signal and two background contributions remain visible in the plot on the right. Taken from [82]

LHCb particle identification is provided by four different detectors: two RICH detectors, the calorimeter and the muon system.

2.4.1 RICH system

The primary role of the RICH system is to provide π/K discrimination in a wide momentum range through the Cherenkov effect. The measurement of the Cherenkov angle θ_c of emitted photons (figure 2.13)provides the velocity v of the particle: given the momentum, different mass particles emit photons with different angle sizes. The particle mass value is then obtained by means the combination of velocity and momentum measurement.
As said before, LHCb is provided by two Cherenkov detectors named RICH1 and RICH2. The use of both detectors together allows us to achieve a π/K separation in a range between 1 and 150 GeV/c, that is the momentum range with 90% kaons and pions produced by B mesons decay.
Cerenkov photons are detected by a combined system of mirrors (both plane and

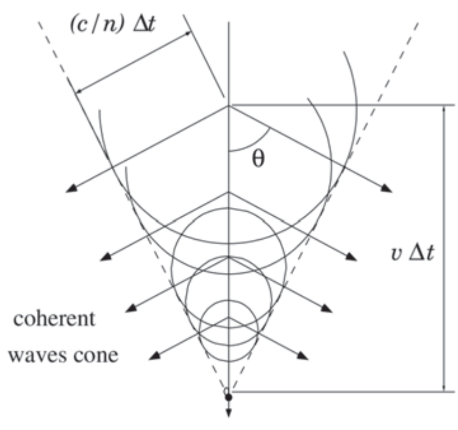

Figure 2.13: Cone of Cherenkov light.

spherical) used to guide photons to photo-detector matrixes (Hybrid Photon Detector, HPD). The light cones, because of reflection on mirrors, appears in the focal plane as circular rings whose radius is proportional to θ_c angle of Cerenkov cone light. The photodetectors are located outside the detector acceptance, in a region where the magnetic field is weak and the radiation is not intense.
The only way to cover a so wide momentum range ($1 < p < 150$ GeV/c) is to exploit two Cerenkov detectors with a different refractive indexes. The RICH1 is designed to detect particles with low and intermediate momentum value, from 1 to 40 GeV/c, while RICH2 the ones with the higher values.

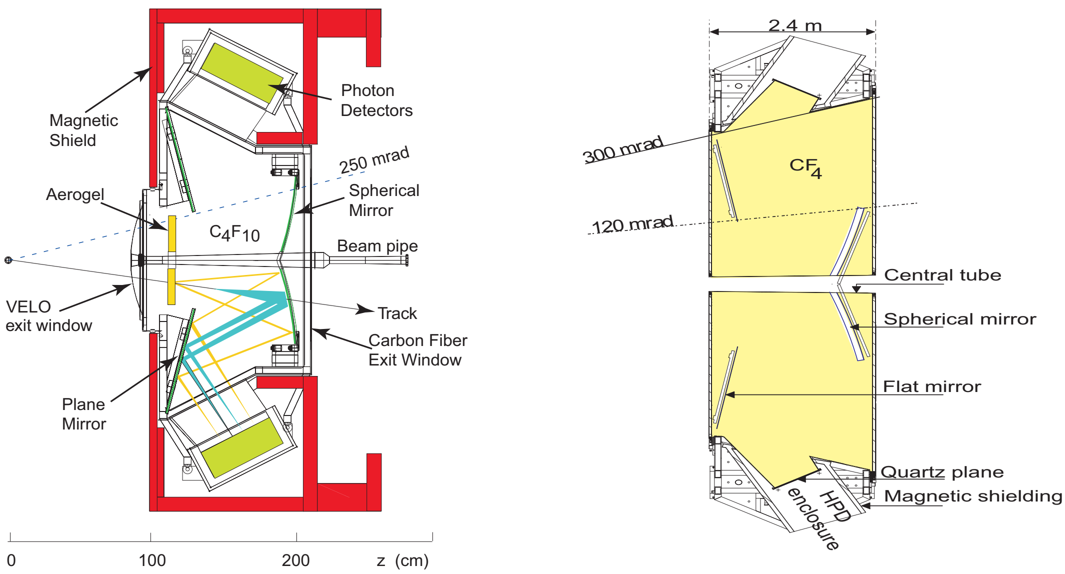

Figure 2.14: Left: RICH1 (y, z) plane sketch view. Right: RICH2 detector.

A RICH1 sketch is shown in figure 2.14 left. The RICH1 is placed close to the interaction region in order to cover the whole LHCb acceptance. It is made up by two different radiator materials: an aerogel layer 5 cm thick whit refractive index $n = 1.03$ and a C_4F_{10} gas layer 85 cm thick with refractive index $n = 1.0014$. The Aerogel, thanks its higher refractive index, is able to make π/K discrimination at lower momenta, to 10 GeV/c, while the C_4F_{10} radiator pushes the discrimination to about 40 GeV/c.
Unlike RICH1, RICH2 has a smaller angular acceptance and is placed more distant, between T3 and the first muon station, in order to detect forward produced particle with high momentum. It covers an angular region of about 120 mrad in the (y, z) plane and 100 mrad in the (x, z) one. The RICH2 is able to discriminate pions from kaon by means CF_4 gas with refractive index $n = 1.00046$. A RICH2 sketch is shown in figure 2.14 right.

The Cherenkov angles for the three different materials and for different particles as a function of the momentum are shown in figure 2.15 [83].

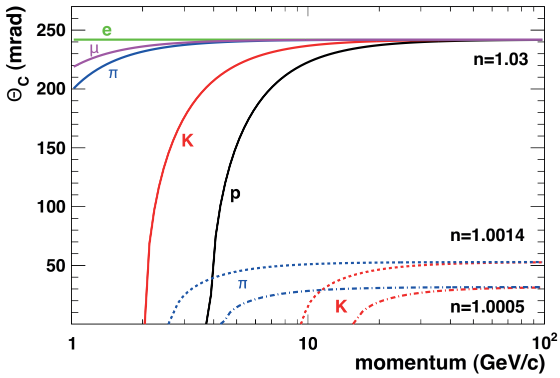

Figure 2.15: Cherenkov angles as a function of momentum for different particles and for the three different values of the refractive index n corresponding to the three radiator materials used in the LHCb RICH setup.

2.4.2 Calorimeters

Calorimeter system's aim is to identify hadrons, electrons and photons and to measure their energy and position for L0 trigger, that takes a decision 4 μs after the interaction. The calorimeter system is made up by four *sub-detectors*:

- The scintillator Pad Detector (SPD)
- The PreShower detector (PS)
- The Electromagnetic Calorimeter (ECAL)
- The Hadron Calorimeter (HCAL)

Each detector is segmented in regions in the xy plane and composed by active cells with different dimensions. ECAL, PS and SPD are divided in three sections with active pads growing from the inner to the outer according to granularity requirements (figure 2.16 *left*). HCAL is divided in two sections (figure 2.16 *right*).

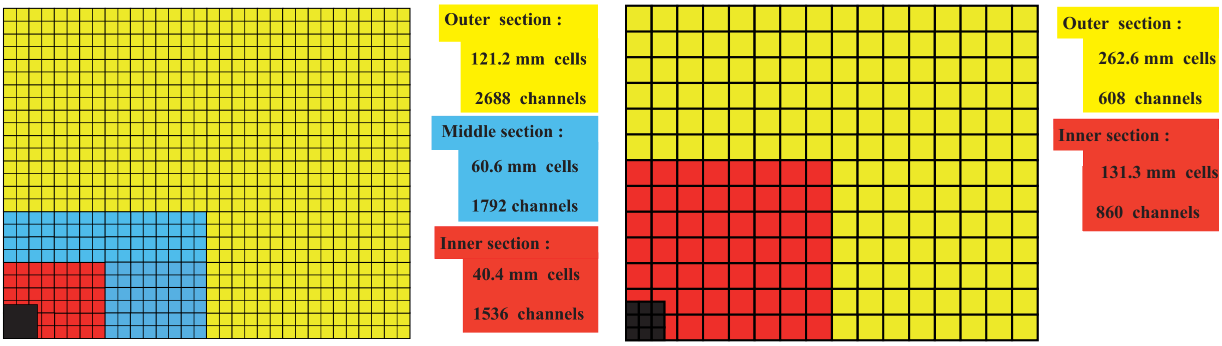

Figure 2.16: Left: SPD, PS and ECAL transverse segmentation. Right: HCAL transverse segmentation. In both figures a square represents a module and only a calorimeters quadrant in (x, y) section is shown.

The SPS and PS are placed just before ECAL. The SPD provides charged and neutral particle separation, while PS is used for pion/electron discrimination. They are used at the trigger level in association with ECAL to indicate the presence of electrons, photons and neutral pions.
The detectors are made by two plastic scintillator layers separated by a 15mm thick lead plate where electrons and photons radiate: the downstream sample scintillator could so collects the radiated energy. The lead thickness is optimized to get a low energy loss for the particles that have to be detected by ECAL. The light from scintillators is sent to photomultipliers by wavelength-shifter (WLS) optical fibers.
ECAL employs the *Shashlik* technology: independent modules, made using scintillating tiles and lead plates, are alternated. Each module consists of 2 mm of lead followed by 4 mm of scintillator material. The ECAL consists of 66 layers of such modules (figure 2.17 right).
ECAL too uses WLS optical fibers to guide the light from the detector to photomultipliers placed on the back of each module. The energy resolution achieved is

$$\frac{\sigma(E)}{E} = \frac{10\%}{\sqrt{E}} \oplus 1\%\,, \tag{2.1}$$

where E is the energy expressed in GeV.
HCAL is a sampling calorimeter too: it is made up by the iron and scintillating tiles, as absorber and active material respectively. The peculiar feature of this sampling structure is the orientation of the scintillating: the tiles run parallel to the beam axis.

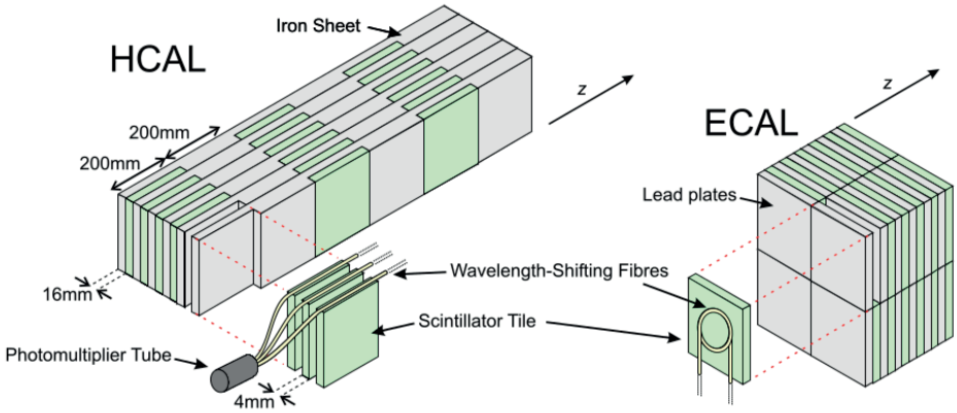

Figure 2.17: Alternate scintillator-absorber layers for HCAL (right) and ECAL (left).

In the lateral direction tiles are spaced with 1 cm iron, while in the longitudinal one the length of the tiles and iron spacers corresponds to the hadron interaction length $\lambda_I \simeq 20$ cm in steel.
The light is collected by the WLS optical fibres running along the detector towards the back side where photomultiplier tubes are housed (figura 2.17 *left*). The HCAL is used to measure the hadronic shower transverse energy for L0 requirements and to give a contribution in improving high momentum electron/hadron separation. The energy resolution achieved is

$$\frac{\sigma(E)}{E} = \frac{(69 \pm 5)\%}{\sqrt{E}} \oplus (9 \pm 2)\% \,, \tag{2.2}$$

where E is the energy expressed in GeV.

2.4.3 Muon System

As stated before, the Muon System (figure 2.18) consists of five stations (M1-M5) of rectangular shape. The complete system is made up by 1380 chambers and covers 465 m^2 area. The complete system has an acceptance in the bending plane from 20 mrad to 306 mrad; while in the non-bending plane from 16 mrad to 258 mrad. This results in a total acceptance of about 20% for muons from semileptonic inclusive b decays.

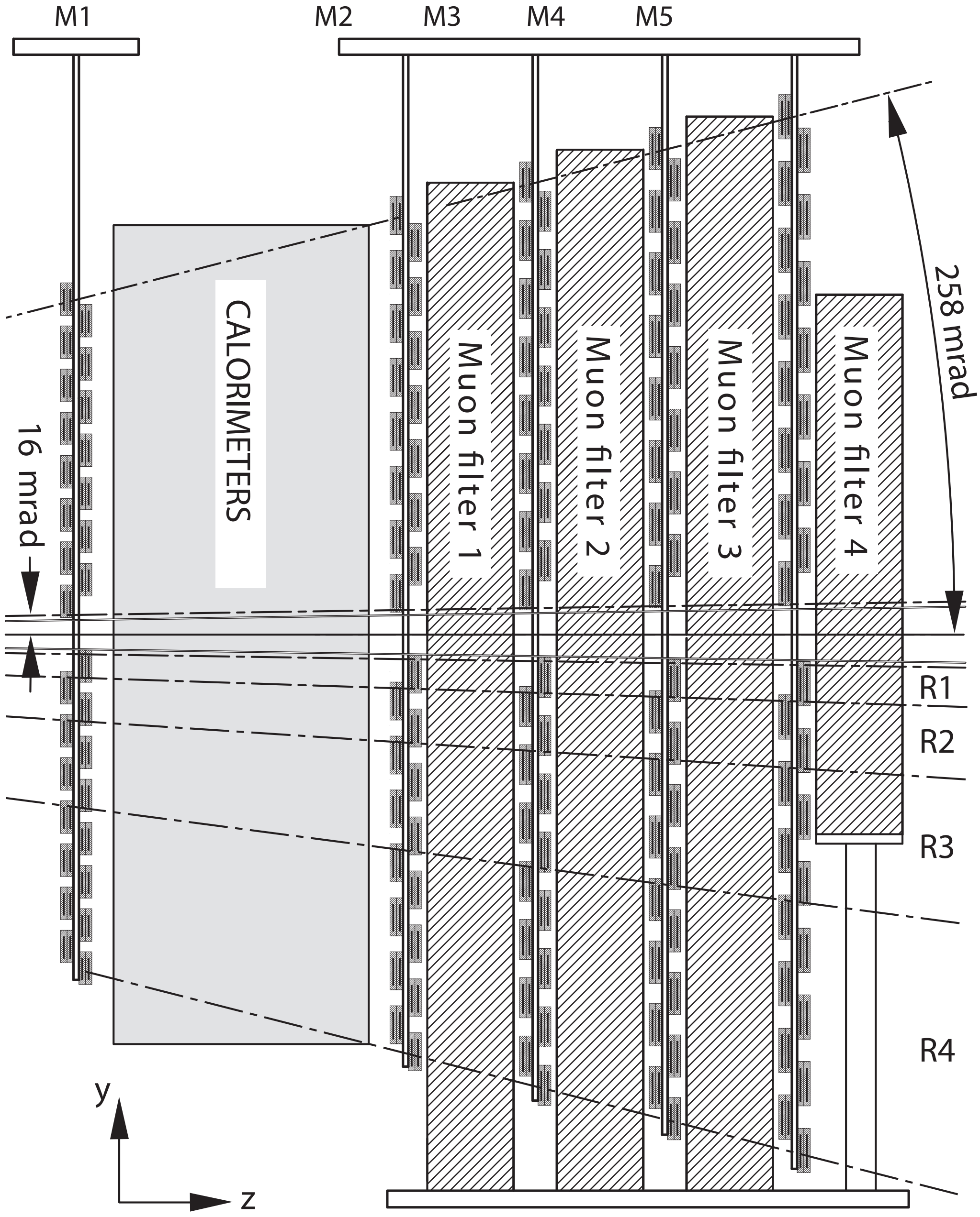

Figure 2.18: Muon system side view.

M1 station is placed in front of the calorimeters and is used in order to improve the p_t measurement in the trigger. M2-M5 are instead placed downstream the calorimeters and are interleaved with 80 cm thick iron absorbers. The total absorption thickness, calorimeters included, is about 20 interaction lengths: in this way the minimum momentum for muons crossing the five stations is about 6 GeV/c. The geometry of the five stations is projective: all the transverse dimensions scale as the distance from the interaction point.
The muon trigger is based on an independent track reconstruction and on p_t measurement, it demands that there are aligned hits in all of the five stations. M1-M3 have high spatial resolution in the x direction (bending plane) and are used to define the track direction and measure the muon candidate p_t with 20% resolution. M4-M5 have a limited spatial resolution being their task to identify penetrating particles. The momentum is obtained by measuring the trajectory deflection in the magnetic field extrapolating the reconstructed track to the magnet center plane at $z_M = 5.15$ m. It is so possible to extrapolate the momentum p by the measurement of θ angle (figure 2.19).

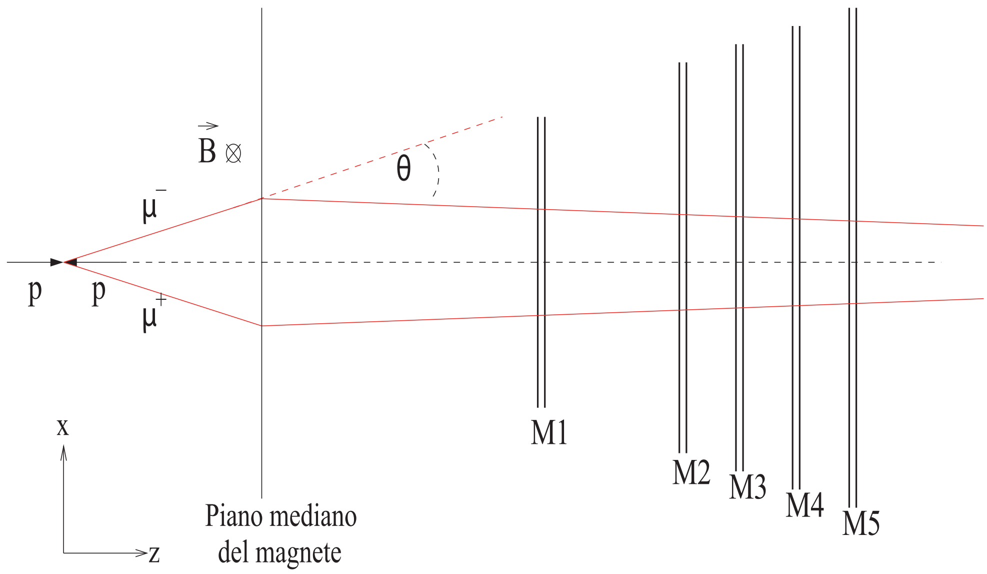

Figure 2.19: Muon station top view (z, x plane). By θ angle measurement muon momentum is obtained.

Each station is divided in four regions from R1 to R4 (figure 2.20) with dimensions scaling in the ratio 1:2:4:8.

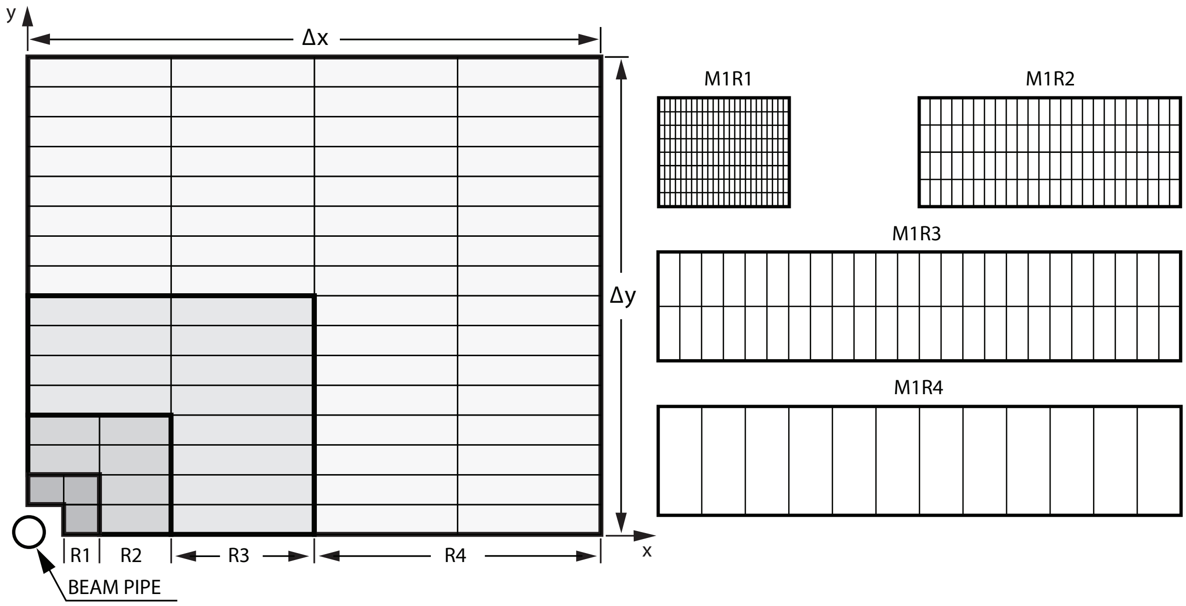

Figure 2.20: Left: station quadrant front view. Each station holds 276 chambers. Right: logical pad segmentation for the chambers related to the four M1 regions. In each region of stations M2-M3 (M4-M5) the pad columns number is twice (half) respect to the corresponding M1 region, while the pad rows number is the same.

The high LHC bunch crossing frequency (40 MHz) and the high particle rate [84] give strict constraints on muon system efficiency, time resolution, rate capability, aging, speed and electronics radiation resistant.
In all regions *Multi-wire proportional chambers* (MWPC) are used, except for the M1 inner region (R1) where, due to the high rate that exceeds the safety limit for aging, triple GEM (*gas electron multiplier*) chambers are used. In the table 2.1 the chambers' geometric features are listed.

Table 2.1: Chambers geometric features. Dimensions are in cm. z: distance from IP; Δx e Δy: quadrant dimensions; R1-R4: region granularity. In square brackets logical pad dimensions, in round brackets logical pad projected to M1 station.

	M1	**M2**	**M3**	**M4**	**M5**
z Δx Δy	1210 384 320	1527 480 400	1647 518 432	1767 556 464	1887 594 495
R1	$[24 \times 8]$ 1×2.5	$[48 \times 8]$ 0.63×3.1 (0.5×2.5)	$[48 \times 8]$ 0.67×3.4 (0.5×2.5)	$[12 \times 8]$ 2.9×3.6 (2×2.5)	$[12 \times 8]$ 3.1×3.9 (2×2.5)
R2	$[24 \times 4]$ 2×5	$[48 \times 4]$ 1.25×6.3 (1×5)	$[48 \times 4]$ 1.35×6.8 (1×5)	$[12 \times 4]$ 5.8×7.3 (4×5)	$[12 \times 4]$ 6.2×7.7 (4×5)
R3	$[24 \times 2]$ 4×10	$[48 \times 2]$ 2.5×12.5 (2×10)	$[48 \times 2]$ 2.7×13.5 (2×10)	$[12 \times 2]$ 11.6×14.5 (8×10)	$[12 \times 2]$ 12.4×15.5 (8×10)
R4	$[12 \times 1]$ 8×20	$[24 \times 1]$ 5×25 (4×20)	$[24 \times 1]$ 5.4×27 (4×20)	$[6 \times 1]$ 23.1×29 (16×20)	$[6 \times 1]$ 24.8×30.9 (16×20)

Each muon station is designed to achieve an efficiency above 99% in a 20 ns time window with a noise rate below 1 kHz per physical channel, as described in [85]. To reach such an efficiency two detectors' layers per station, connected in logical OR, are used; while the time resolution is achieved by a fast gas mixture.
In M2-M5 the MWPC are made up by four *gaps* in two layers with independent reading; in M1 the chambers have only two *gaps* in order to minimize the material in front of the calorimeters.
Two different solutions for the readout are used (table 2.2): chambers are divided in

logical pad, anode wires and cathode pads for MWPCs and anode pads for GEMs, that are red by a front end electronics (FE). In order to keep a limited noise and

Table 2.2: Reading methods used in the muon chambers

Reading	Region
MWPC	
wire pad	R4
wire and cathode pad combination	R1-R2 in M2-M3
cathode pad	in the other regions
GEM	
anode pad	M1R1

a short dead time, the electric capacitance and the rate of a single pad has to be kept limited. So, in many chambers, the physical pad dimensions have to be smaller than the spatial resolution requirements. In these cases up to four consecutive pads are used to form a logical pad. On the other hand, in R1-R2 regions of M2-M3 stations, the required spatial resolution on x is such that the logical pads should be too smaller to be manufactured, so a combination of wire strips and cathodic pads is used.
The whole muon system consists of 122112 physical channels, OR connected in 25920 logical channels and transmitted by optical connections to L0 trigger and to DAQ. The appropriate combination of logical channels in L0 e in HLT gives the 55296 logical pad used in muon tracking.

Multi Wire Proportional Chambers

A total number of 1368 *Multi Wire Proportional Chambers* is used. The time resolution is about 5 ns per gap, thanks to 2 mm wire spacing, with a total gap thickness of about 5 mm. The necessary time resolution is ensured by a fast gas mixture and an optimized charge-collection geometry. The gas used is the non-flammable $Ar/CO_2/CF_4$ mixture in the ratio 40:55:5. The high voltage can varies from 2600 V to 2700 V. The maximum gain for MWPC is about 10^5.

Triple GEM Chambers

The M1 station inner region R1 (12 chambers) is exposed to a very high particle rate and the chambers need a good aging performance and reduced dead time. As for the other regions, two detector layers per station, connected in logical OR, are here used too. A GEM is made up by a thin kapton foil (50 μm) plated with copper on each face. The foil is perforated in a large number of holes. Each hole has a bi-conic structure whose external diameter is about 70 μm, the internal one about 50 μm and the distance between two consecutive holes is about 140 μm. The detector consists in three GEM layers, the anode, segmented in pads, and the cathode. The gas mixture is $Ar/CO_2/CF_4$ in the ratio 45:15:40.

The muon identification

The muon identification strategy can be divided in three steps:

IsMuon binary selection: given a reconstructed track in the LHCb tracking system, is defined according to the number of stations (function of track momentum p as shown in table 2.3) where a hit is found within a field of interest (FOI) defined around the track extrapolation.

Table 2.3: Muon stations request to trigger the IsMuon decision as a function of momentum range.

Momentum range	**Muon stations**
3 GeV/c < p < 6 GeV/c	M2 and M3
6 GeV/c < p < 10 GeV/c	M2 and M3 and (M4 or M5)
p > 10 GeV/c	M2 and M3 and M4 and M5

muDLL: using the tracks surviving the IsMuon requirement, the average squared distance significance is defined as:

$$D^2 = \frac{1}{M}\sum_i \left\{ \left(\frac{x^i_{closest} + x^i_{track}}{pad^i_x} \right)^2 - \left(\frac{y^i_{closest} + y^i_{track}}{pad^i_y} \right)^2 \right\} \tag{2.3}$$

where the index i runs over the stations containing hits within the FOI, $x^i_{closest}$ and $y^i_{closest}$ are the coordinates of the closest hit to the track extrapolation point for each station (x^i_{track} and y^i_{track}) and $pad^i_{x,y}$ corresponds to one half of the pad sizes in the x,y directions. The total number of stations containing hits within their FOI is denoted by N. True muons tend to have a much narrower D^2 distribution, close to zero, than the other particles that are incorrectly selected by the IsMuon requirement.

Combined likelihood: muDLL is combined with the likelihoods provided by the RICH systems and the calorimeters to improve the muon identification performance. For each track in the event, a likelihood is assigned to each of the different mass hypotheses (electron, muon, pion, kaon and proton). The RICH likelihood can differentiate between muons and other particles in particular at low momentum, below 5 GeV/c. The informations from calorimeters are also used to evaluate likelihoods for the minimum ionizing particle's (MIP) muon, electron and hadron hypotheses. A combined log-likelihood is then obtained for each track and for each of the different mass hypotheses by summing the logarithms of the likelihoods obtained using the muon system, the RICH and the calorimeters. In this computation, the non-muon likelihood obtained in the muon system is assigned to the electron, pion, kaon and proton hypotheses. The difference of the combined log-likelihoods for the muon and pion hypotheses (DLL) is then used to identify the muons.

2.5 LHCb Trigger

The LHCb trigger is composed by two different trigger levels: the Level-0 (L0) based on custom electronic boards and the High-Level (HLT) on a computer farm. L0 makes decisions based on information get from the calorimeter and muon systems only and it performs selection in order to reduce the event rate from 40 MHz to below 1 MHz. The HLT is a software application running on a processor farm that further reduces the rate of accepted events to about 3 kHz to be stored (figure 2.21).
The trigger purpose is to achieve the highest efficiency for the events selected in the offline analysis and it is optimised to reject as strongly as possible uninteresting background events.

2.5.1 Level-0 hardware trigger

The L0 trigger is divided into three independent units; the L0-Calorimeter trigger, the L0-Muon trigger and the L0-PileUp trigger of VELO, used only for the determination of the luminosity, following the procedures:

- cluster selection in the calorimeter due to hadron, photon and highest transverse energy electron,
- highest p_t muon selection in the muon system,

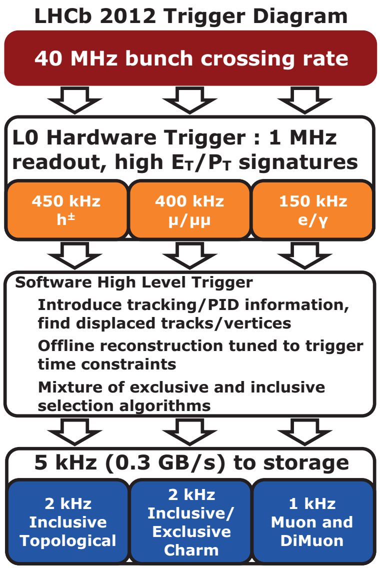

Figure 2.21: Trigger scheme for LHCb [87].

- multiple visible interactions per bunch crossing rejection by means of the "ad hoc" *Pile-Up System* detector housed in the VELO.

L0 calorimeter system

The L0-Calorimeter part of the trigger get informations from SPD, PS, ECAL and HCAL and computes the transverse energy deposited by incident particles: $E_T = E_0 \cos\theta$ where E_0 is the energy of the particle and θ is the angle given by the position in the detector. Together with energy information, the total number of hits in the SPD (SPD Multiplicity) is also determined in order to veto events that would take a too large fraction of the available processing time in the HLT. From calorimeter informations three types of candidates are built and selected according to specific transverse energy (E_T) criteria:

1. Hadron candidate (L0Hadron)

2. Photon candidate (L0Photon)

3. Electron candidate (L0Electron)

L0 muon processors

L0 requires a muon candidate to have a hit in all five muon stations. The L0 muon processors boards select the two highest p_T muon tracks in each quadrant of the muon system with a maximum of eight candidates. The trigger sets single threshold either on the largest muon p_T (L0 muon trigger) or on the product of the largest and the 2nd largest (L0 dimuon trigger).

Events with SPD multiplicity > 600 are excluded in the L0 muon trigger in order to minimize the track multiplicity. This limit is raised to 900 in the L0 dimuon trigger for a small increase in rate.

The typical L0 thresholds used in Run I are listed in the table 2.4 [88]:

Table 2.4: L0 thresholds for Run I

Line	2011	2012
L0Hadron E_T	> 3.50GeV	> 3.70GeV
L0Photon E_T	> 2.50GeV	> 3.00GeV
L0Electron E_T	> 2.50GeV	> 3.00GeV
L0Muon p_T	> 1.48GeV$/c$	> 1.76GeV$/c$
L0DiMuon $p_T^{\mu_1} \times p_T^{\mu_2}$	$> (1.30\text{GeV}/c)^2$	$> (1.60\text{GeV}/c)^2$

The total output rate of the L0 trigger is limited to 1 MHz, which is the maximum rate value accepted by the HLT1. Such output rate consists of: about 400 kHz of muon triggers, about 500 kHz of hadron triggers and about 150 kHz of electron and photon triggers, where the individual triggers have an overlap of about 10%.

2.5.2 High Level Trigger

Data from L0 are send to the Event Filter computer Farm (EFF) which runs the HLT algorithms. The HLT is a software application whose 29500 instances run on the EFF. Each instance is made up of independently operating trigger lines: each line consists of selection parameters for a specific class of events.
The HLT is divided into two stages. The first stage (HLT1) processes the full L0 rate and uses partial event reconstruction to reduce the rate to 43 kHz. The second stage (HLT2) reduces the rate to about 3 kHz performimg a more complete event reconstruction [90].

HLT1

The offline VELO reconstruction algorithm performs a full 3D pattern recognition and is fast enough to be run on all events entering the HLT. However, it makes a second pass on unused hits to enhance the efficiency for tracks pointing far away from the beam-line. In the first stage of the HLT this second pass is not used because of CPU constraints. Vertices are reconstructed from a minimum of five intersecting VELO tracks and are considered to be "primary vertices" when are in a radius of 300 μm of the mean position of the pp-interaction envelope. HLT1 limits the number of VELO tracks that are passed through the forward tracking algorithm (that searches for matching hits in the tracking stations). The forward track search has further a minimum momentum requirement, between 3 and 6 GeV/c during Run I. If a VELO track without matching muon hits occurs, then a minimum p_T between 0.5 and 1.25 GeV/c is required. The reconstructed forward tracks are then fitted.
For comparison, with this procedure a resolution of only 3% worse than the 15.1 MeV/c^2 obtained offline is found for the invariant mass of $J/\psi \to \mu^+\mu^-$ candidates reconstructed. For muon candidates the offline muon identification algorithm [91] is applied, so the purity of the muon sample is increased.
The inclusive beauty and charm trigger selection is based on track p_t and on displacement from the primary vertex (typical value IP $>$ 0.1 mm). This trigger line produces around 58 kHz of output: the largest contribution to the allocated HLT1 bandwidth. It is the most efficient line for physics channels that do not contain leptons in the final state. The inclusive one-track based trigger also exists in a version for electrons or photons identified by L0, with reduced thresholds related to the inclusive version. The output rate of these lines is around 7 kHz.
A similar line exists for tracks that are matched to hits in the muon chambers. Such trigger line is able to select those good quality muon candidates that are detached from the primary vertex and that have $p_T > 1\text{GeV}/c$; whereas single muon candidates with $p_T > 4.8\text{GeV}/c$ are selected by a trigger line without any vertex separation requirements.
Dimuon candidates are either selected based on their mass values: if $m_{\mu\mu} > 2.5\text{GeV}/c^2$ the selection in made without any displacement requirement, otherwise it is based on their displacement without the mass requirement. Dimuon candidates are also triggered based on their distance of closest approach (DOCA): the distance of closest approach of two objects is defined as the distance between their centers when they are externally tangent and can be referred to objects with geometric shapes or physical particles with well defined boundaries.
After the combination of the muon trigger lines, a 14 kHz output rate is obtained. Dedicated lines are developed in order to improve the trigger performance in case

of the presence of events containing candidates for displaced vertices, high ET jets, di-protons or high p_T electrons. Luminosity and beam-gas measurements could be selected by additional lines used in the HLT1.
HLT1 muon lines are executed only if events have passed L0Muon or L0DiMuon. They are divided in sigle and dimuon lines: Hlt1TrackMuon accepts events with B, D or τ decays with at least one muon in the final state, Hlt1SingleMuonHighPT triggers on muons originating from heavy particles with a negligible lifetime like $W^\pm$ or Z^0, Hlt1DiMuonHighMass selects b-hadron decays without lifetime cuts, Hlt1DiMuonLowMass triggers on final states with two muons with a relatively small invariant mass.
The names of the HLT1 muon lines and their cuts are listed in table 2.5 [89]:

Table 2.5: HLT1 muon lines and their cuts.

Hlt1	**TrackMuon**	**SingleMuon HighPT**	**DiMuon HighMass**	**DiMuon LowMass**
Track IP (mm)	> 0.1	–	–	–
Track IP χ^2	> 16	–	–	> 3
Track p_T (GeV/c)	> 1	> 4.8	> 0.5	> 0.5
Track p (GeV/c)	> 8	> 8	> 6	> 6
Track χ^2/ndf	< 2	< 4	< 4	< 4
DOCA (mm)	–	–	< 0.2	< 0.2
χ^2_{vertex}	–	–	< 25	< 25
Mass (GeV/c^2)	–	–	> 2.7	> 1
Rate (kHz)	5	0.7	1.2	1.3

HLT2

The HLT2 is able to reduce the rate down to ~ 3 kHz: at this rate HLT2 performs forward tracking of all VELO tracks. HLT2 employs the algorithm based on seeding the search with VELO tracks. In order limit the search windows $p > 5$GeV/c and $p_T > 0.5$GeV/c cuts are applied.
Muon identification is performed using the off-line algorithm on all tracks from the forward tracking. Tracks are also associated to ECAL clusters to identify electrons. Informations from the L0-Calorimeter system are used to build photons and neutral pions.
The HLT2 is made up by:

- **Generic beauty trigger**: a large portion of the 3 kHz output rate of HLT2 is selected by *topological* trigger lines, which are designed to trigger on partially reconstructed inclusive b-hadron decays. Such kind of lines are used to cover all b-hadrons with at least two charged particles in the final state and a displaced decay vertex. The track selection is based on requirements on track fit quality ($\chi^2/ndof$), impact parameter (IP) and identification of muons or electrons. N-body vertexes are constructed, starting from the selected tracks, by requiring their distance of closest approach (DOCA), while n-track combination uses the variables: $\sum |p_T|$, p_T^{min}, n-body invariant mass (m), DOCA, IPχ^2 and flight distance (FD) χ^2. The output rate of the topological trigger is 2 kHz.

- **Muon triggers**: are designed to select events containing muon or dimuon candidates. The single muon candidate event is selected by two different lines: the first one, called Hlt2SingleMuon, selects semileptonic b and c-hadron decays with the TOS condition[1]; the second one, Hlt2SingleMuonHighPT, is designed to select heavy particles, like $W^{\pm}$ and Z^0, that decay promptly to one or more muons.
  The Dimuon candidates selection is grouped in two categories: the ones dedicated to prompt decays use the mass as the main discriminant, while detached lines use the separation between the dimuon vertex and the PV as the main discriminant. The first group is formed by Hlt2DiMuonJPsi(Psi2S) and Hlt2DiMuonJPsi(Psi2S)HighPT lines.
  The second one is made by Hlt2DiMuonDetached, Hlt2DiMuonDetachedHeavy and Hlt2DiMuonDetachedJPsi lines.
  Such lines are optimized in order to take advantage of the physics potential of J/ψ and $B \to J/\psi X$ decays.
  The total output rate of all single and dimuon trigger lines is about 1 kHz.

- **Charm triggers**: about 600 kHz of $c\bar{c}$-events are produced in the 2012 in the LHCb acceptance, so tight exclusive selections are required. Hadronic two and three body lines are the main exclusive selections for prompt charm. The total output rate of all charm selections is about 2 kHz.

The cuts corresponding to all HLT2 lines are summarized in the following tables [89]:

[1] An event is classified as TOS (Trigger on Signal) if the trigger objects that are associated with the signal are sufficient to trigger the event. An event is classified as TIS (Trigger Independent of Signal) if it could have been triggered by those trigger objects that are not associated to the signal.

Table 2.6: HLT2 lines based on single muon identification.

Hlt2Single	**Muon**	**MuonHighPT**
Hlt1TrackMuon	TOS	–
Track IP (mm)	> 0.5	–
Track IP χ^2	> 200	–
Track p_T (GeV/c)	> 1.3	> 10
Track χ^2/ndf	< 2	–
Pre-scale	0.5	1
Rate (Hz)	480	45

Table 2.7: HLT2 lines based on dimuon identification belonging to the first category (see text).

Hlt2DiMuon	**JPsi**	**Psi2S**	**JPsiHighPT**	**Psi2SHighPT**
Track χ^2/ndf	< 5	< 5	< 5	< 5
Mass (GeV/c^2)	$m_{J/\psi} \pm 0.12$	$m_{\psi(2S)} \pm 0.12$	$m_{J/\psi} \pm 0.12$	$m_{\psi(2S)} \pm 0.12$
χ^2_{vertex}	< 25	< 25	< 25	< 25
$p_T^{\mu\mu}$ (GeV/c)	–	–	> 2	> 3.5
Pre-scale	0.2	0.1	1	1
Rate (Hz)	50	80	115	15

Table 2.8: HLT2 lines based on dimuon identification belonging to the second category (see text)

Hlt2DiMuon	**Detached**	**DetachedHeavy**	**DetachedJPsi**
Track χ^2/ndf	< 5	< 5	< 5
Track IP χ^2	> 9	–	–
Mass (GeV/c^2)	> 1	> 2.95	$m_{J/\psi} \pm 0.12$
FD (flight distance) χ^2	> 49	> 25	> 9
χ^2_{vertex}	< 25	< 25	< 25
$p_T^{\mu\mu}$ (GeV/c)	1.5	–	–
Rate (Hz)	70	75	35

2.6 LHCb software

Beside the real p-p collisions, simulated events are produced in order to estimate detector response, the invariant mass distribution of the background processes, to obtain the shape of the signal decays and to obtain the selection efficiency. In this light, the events' reconstruction and the physics analysis softwares are designed to use both real and simulated events.
The simulation phase consists in three main steps:

- **Event generation**: consists in the simulation of hadron production in p-p collisions and in the generation of their decay.
- **Detector response simulation**: is the simulation of the detector particle tracking and the simulation of the physics processes occurring in the interaction with the experimental setup.
- **Digitization of simulated data**: responsible for digitizing the output from the simulation phase.

The generation and the simulation are made by the Gauss package software.
The simulation phase consists of two different softwares: **PYTHIA** that is used to create p-p collisions and **EvtGen** that is dedicated to b-hadrons particle decays. The simulation phase of **Gauss** uses **GEANT4** and the detector description database (**DDDB**) to simulate the passage of particles through the LHCb detector.
The Digitization phase is done by **BOOLE** that take the output from **Gauss** simulation and forms an output in the same format as real data read directly from the experiment: at this point, both real data and simulated data are processed by the **Moore** software. **Moore** runs either in the online trigger farm processing online data from the LHCb DAQ system, or offline starting from real data or from the output of the detector digitization application.
Both real and simulated data are now reconstructed by the event reconstruction application called **BRUNEL** that makes data ready for analysis: it reconstructs tracks in the event, runs particle identification algorithms and creates the so called *proto-particles*. The *proto-particles* retains all the informations about their kinematic, reconstruction process and a list of identification hypothesis with a probability.
The chain is finally concluded with the physics analysis made by the **DaVinci** software package, used to study both real and simulated data. It forms particles starting from *proto-particles* and associating them a choice of particle identification. The analysis is then performed combining the particle formed and fitting them in order to compose composite particles. **DaVinci** allows also to perform a series of

cuts on many parameters in order to refine the event selections.
Since not all of the full events coming from the recorded data contain decays of interest for any single analysis, the concept of *stripping* is introduced. The aim of stripping at LHCb is to reduce the dataset used for a single analysis by breaking down it into lines to be used in data analysis. The stripping is run over the reconstructed data using **DaVinci** and each line is fed by many stripping selections, which are algorithms designed for specific decay channels in the data sample. In this way only the events passing one or more of the lines are retained. Stripping lines regarding similar physics analysis can be also grouped into streams. Data are then stored in files called *DST* (*Data Summary Tape*).

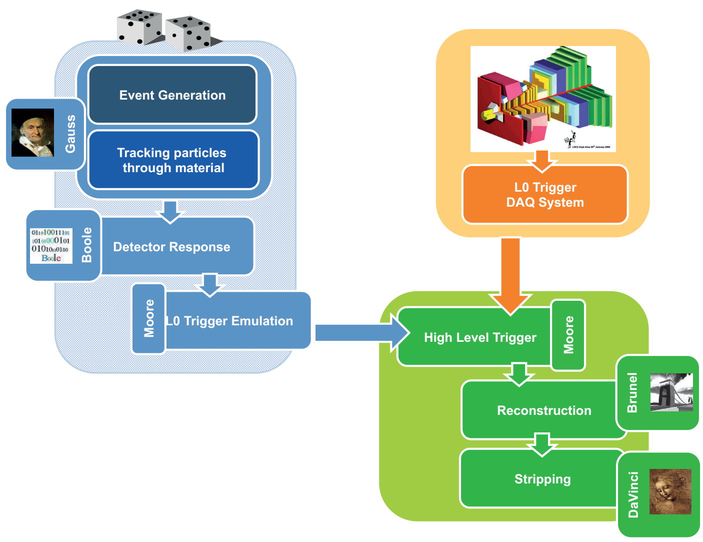

Figure 2.22: Outline of the LHCb data processing. On the left in blue the processing of Monte Carlo samples, the Data Taking in orange on the right. The Reconstruction and Stripping for both the MC and the data collected by the DAQ of the experiment are in green [92].

Chapter 3

$B^{\pm}$ mass measurement

3.1 Introduction

As stated before, in the SM framework hadrons are colourless particles composed of quarks and gluons that interact by means the strong interactions described by Quantum chromodynamics (QCD).
B meson physics is one of the critical elements of the flavor physics programme since the properties of such particles are important to constrain CKM elements.
In section 1.5.3 Lattice QCD (LQCD) was described and it was shown as lattice calculations could provide B meson mass values. In addiction, an improvement in B meson mass measurement should be of interest in order to measure the B charged and B neutral mass difference: today the value of such difference is less than experimental error on B mesons mass.
In this light accurate experimental measurements are essential and thanks to the luminosity reached at LHC it is now possible to improve the measurements recorded in literature in particular for B mesons since LHCb provides a unique b physics laboratory.
The objective of this analysis is to improve the measurement of the B^+ meson mass (charge-conjugate state is implied throughout).
The current B^+ meson mass value, as reported by PDG [93], is

$$m(B^+) = 5279.25 \pm 0.26\ \mathrm{MeV}/c^2$$

and it is obtained by performing the average of the experimental measurements starting from 1996. The last two measurements, in particular, were made by experiments located in two different hadron colliders: CDF at Tevatron in 2006 [94] and LHCb at LHC in 2012 [95].

CDF operated at $\sqrt{s} = 1.96$ TeV and it collected data corresponding to an integrated luminosity of 220 pb^{-1}. The B^+ mass was measured by reconstructing the decay mode $B^+ \to J/\psi K^+$. CDF reconstructed about 2300 B^+ mesons and obtained the following result:

$$m(B^+) = 5279.10 \pm 0.41_{stat} \pm 0.36_{sys} \text{ MeV}/c^2$$

The LHCb measurement is based on the same channel used by CDF on a data sample obtained at LHC pp collider at $\sqrt{s} = 7$ TeV center of mass energy. Collected in the 2010, it corresponds to an integrated luminosity of 35 pb^{-1}. The signal yield obtained by LHCb is about 11000 leading to the result of:

$$m(B^+) = 5279.38 \pm 0.11_{stat} \pm 0.33_{sys} \text{ MeV}/c^2,$$

that is more precise than the previous ones from CDF II and from the other experiment listed by PDG [93].
In order to get an high mass resolution a decay with all charged particles in its final state was chosen. In this way the B meson under the study can be reconstructed with the higher efficiency: charged particles are reconstructed using tracking detectors (see section 2.1) formed by the VELO that encloses the interaction region, the TT stations before the spectrometer magnet and the T1-T3 stations downstream. The high spatial resolution of the VELO provides a precise determination of the particle's flight direction close to the primary interaction point, resulting in a high vertex and angular resolution.
The error on invariant mass measurement is then mainly given by the error on momentum measurement, being the error on angle measurement negligible. If δp and $\delta\theta$ are the errors related to momentum and angle measurements the resolution on mass measurement is obtained:

$$\frac{\delta m_0}{m_0} = \frac{m_0^2 - m_1^2 - m_2^2}{2m_0^2}\left[\left(\frac{\delta p_1}{p_1}\right)^2 + \left(\frac{\delta p_2}{p_2}\right)^2 + \left(\frac{\delta\theta}{tan\theta}\right)^2\right]^{1/2}.$$

Another factor that determines the precision of the measurement is the size of systematics related to the momentum scale. Such biases can be due to several effects: an inaccurate description of the alignment of LHCb detectors, the use of an not well described particle energy loss in the track fit, an incorrect magnetic field map. So, a good calibration of the momentum scale is needed.
The momentum scale calibration is based on a large samples of $B^+ \to J/\psi K^+$ decays and it is referred to the same dataset used in this analysis [97].

Such deviation is converted in an estimate of the momentum scale bias, referred to as α, which is defined such that the measured mass is equal to the expected value when the momentum of all particle if multiplied by $1 + \alpha$ factor. In figure 3.1 the resulting values of α for various decay modes are shown.
The largest value of $|\alpha|$ amongst the considered modes, 0.3×10^{-3}, is conservatively

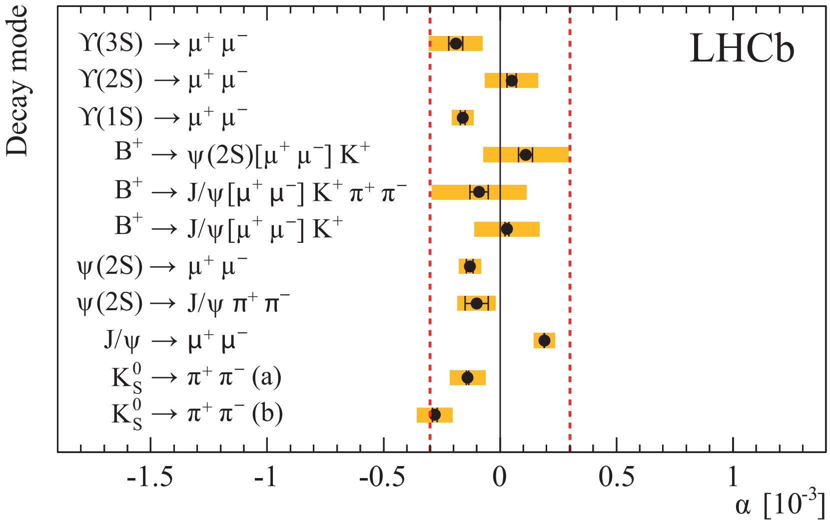

Figure 3.1: Average momentum scale bias α determined from the reconstructed mass of various decay modes after the momentum calibration procedure [97]. The black error bars represent the statistical uncertainty whilst the yellow filled areas also include contributions to the systematic uncertainties.

taken as the systematic uncertainty on the calibrated momentum scale (due to changes in the alignment of the tracking devices, the resulting uncertainty obtained in the last analysis is a bit larger than the 0.2×10^{-3} achieved in the previous one with the 2010 data [98]. The dataset used in the 2010 was relatively small and a very careful calibration was done. Large changes to detector performance/alignment was identified and the detector was re-aligned correspondingly and a very good precision was achieved (0.02%). In the 2011-2012, on the contrary, the alignment was done in larger blocks and detector conditions were less homogeneous and in the end 0.03% was achieved.).

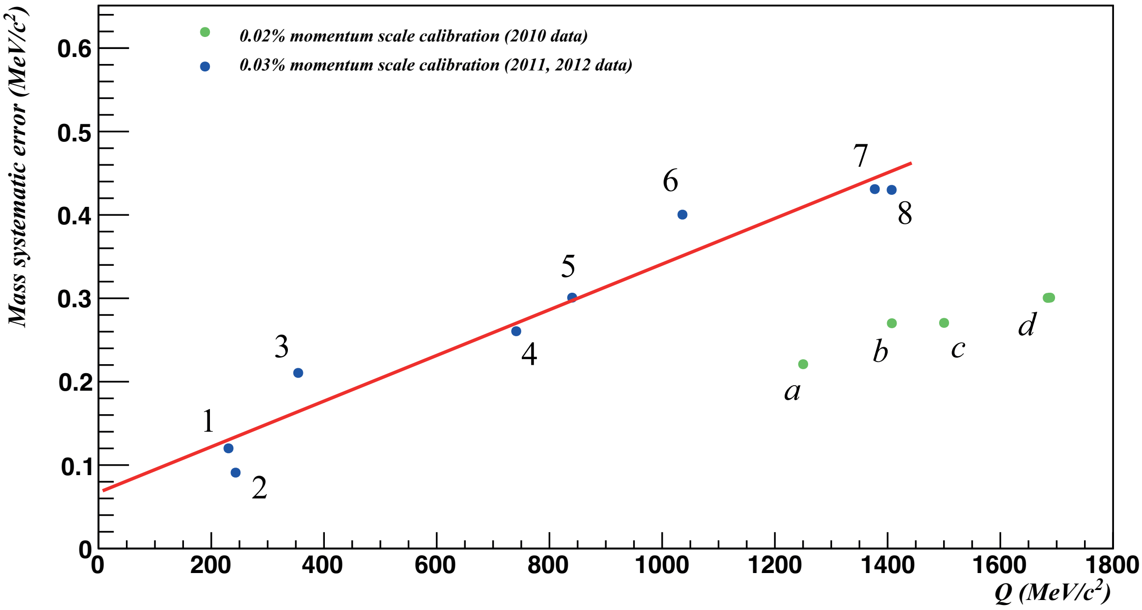

Figure 3.2: Momentum scale systematic error on mass measurements at LHCb vs Q value. The decay are listed in table 3.1.

Table 3.1: Decay channel list referred to figure 3.2.

1) $B_s \to J/\psi\phi\phi$ [99]
2) $D^0 \to K^+K^-K^-\pi^+$ [101]
3) $D^0 \to K^+K^-\pi^+\pi^-$ [101]
4) $D^\pm \to K^+K^-\pi^\pm$ [101]
5) $D_s^+ \to K^+K^-\pi^+$ [101]
6) $B_c^+ \to p\overline{p}\pi^+$ [103]
7) $\Xi_b^- \to J/\psi\Xi^-$ [102]
8) $\Lambda_b^0 \to J/\psi\Lambda$ [102]
a) $B_s^0 \to J/\psi\phi$ [104]
b) $\Lambda_b^0 \to J/\psi\Lambda$ [104]
c) $B^0 \to J/\psi K^{*0}$ [104]
d) $B^+ \to J/\psi\phi K^+$ [104]

In order to compute the effect of the momentum scale error on the mass measurement let us to consider a generic n-body decay of a particle of mass M.
In the center-of-mass frame we can write $M = E_1 + E_2 + \cdots E_n$. The error on M can be written as

$$\delta M = \beta_1 \delta p_1 + \beta_2 \delta p_2 + \cdots \beta_n \delta p_n = (\beta_1 p_1 + \beta_2 p_2 + \cdots \beta_n p_n)\delta\alpha$$

where

$$\delta\alpha = \delta p/p.$$

The error is minimized when the daughter particles have the lowest possible velocity. This is achieved when the the $Q-$value of the decay tends to zero:

$$Q = M - \sum m_i \to 0$$

and it remains true if the momenta are measured in the laboratory frame.
In the non-relativistic limit $\beta p = 2T = 2(E - m)$, the kinetic energy of the particle. Therefore, summing over all the particles

$$\delta M = 2(M - \sum m_i)\delta\alpha = 2Q\delta\alpha.$$

In general we can assume that approximately $\delta M = k\,Q$ where k is a constant for a given momentum resolution.
Fig. 3.2 shows the systematic error vs Q for several hadron masses measured by LHCb and confirms the advantage of using decays with the lowest possible $Q-$value. As an example, the decay $B_s \to J/\psi\,\phi\,\phi$, first observed in the Tor Vergata group [99], will allow, with sufficient statistics, to improve substantially the precision on the B_s mass.
Previous measurements of the B^+ mass used the decay $B^+ \to J/\psi K^+$, having $Q = 1690$ MeV$/c^2$. In this thesis the channel $B^+ \to J/\psi\phi K^+$ has been selected for the mass measurement. For this decay the $Q-$value is about 670 MeV$/c^2$ allowing a factor ≈ 3 improvement in the systematic accuracy.
From simulation the systematic for this decay is obtained to be 0.24 MeV$/c^2$: this is in agreement with the trend shown in the plot of figure 3.2 and, as expected, its value is less than the one expected for $B^+ \to J/\psi K^+$ decay.
Unfortunately this channel is highly suppressed in comparison with the first one. From the literature [93] it is obtained:

$$\frac{\Gamma\,(B^+ \to J/\psi\phi K^+)}{\Gamma\,(B^+ \to J/\psi K^+)} = (5.06 \pm 1.66) \times 10^{-2}\,, \tag{3.1}$$

but it was possible to get about the same B^+ statistics of LHCb and CDF previous analysis by considering that the LHCb integrated luminosity from the 2010 to the 2012 is about 100 times grater than the one used by LHCb in the 2010.

3.2 $B \to J/\psi\phi K$ decay channel

The first observation of this decay was made at CLEO detector [100] at the Cornell Electron Storage Ring (CESR) in 2000 when 10 fully reconstructed candidates were observed. Later, in 2003, it was also studied by the BaBar collaboration [105]. At the time it was the first observed B meson decay requiring the creation of an additional $s\bar{s}$ quark pair. This decay occurs when, together with the quarks produced in the $b \to c\bar{c}s$ transition, a $s\bar{s}$ pair is created from sea quarks. In this case the transition proceeds as a three-body decay or is connected via gluons (figure 3.3). This decay has been extensively used by LHCb for studies on exotic structures in $J/\psi\phi$ mass spectrum and $J/\psi K$ mass spectrum [108, 109].

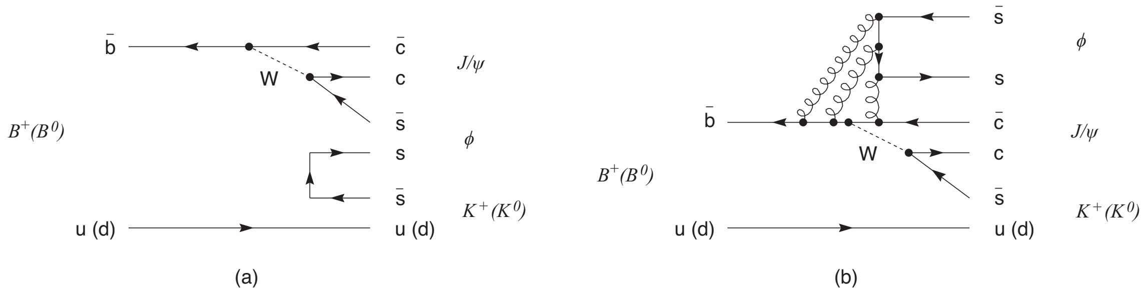

Figure 3.3: Quark diagrams for charged and neutral B meson decay: (a) $s\bar{s}$ sea quarks, (b) gluon coupling.

For what concerns the branching fraction of this decay, the last studies was performed by BaBar collaboration in 2014. Analysis concerning the rare decays $B^+ \to J/\psi K^+K^-K^+$ and $B^0 \to J/\psi K^+K^-K^0_S$, the search for possible resonant states in the $J/\psi\phi$ mass spectrum and the search for the decay $B^0 \to J/\psi\phi$ [111] have reported a last much-improved measurement of the branching fractions of $B \to J/\psi\phi K$ decays. In particular, the decay of B^0 was measured with a precision better more than four times related to the previous one. The current branching fractions are [93]:

In this analysis the $B^+ \to J/\psi\phi K^+$ decay (with $J/\psi \to \mu^+\mu^-$ and $\phi \to K^+K^-$) is studied. The candidates reconstruction and selection, described in the next sec-

Table 3.2: Summary of Branching Fractions of $B \to J/\psi\phi K$ decay (PDG average [93]).

Decay mode	**Branching Fraction** $(\times 10^{-5})$
$B^{\pm} \to J/\psi\phi K^{\pm}$	5.1 ± 0.4
$B^{0} \to J/\psi\phi K^{0}_{S}$	4.9 ± 1.0

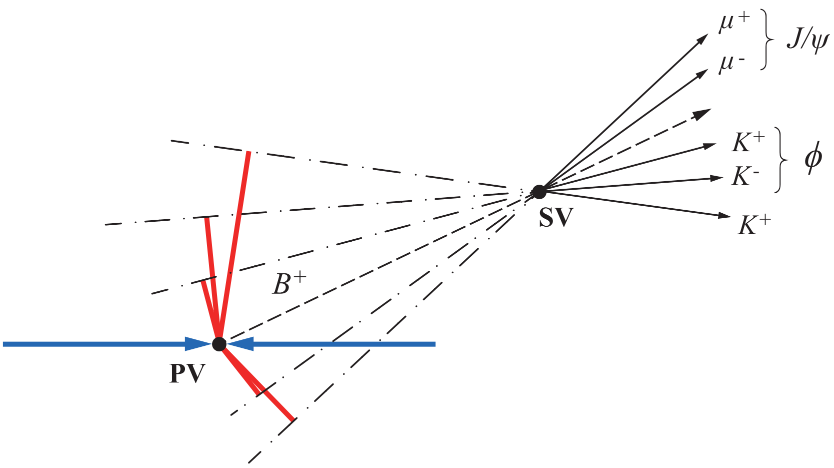

Figure 3.4: Schematic illustration of the $B^+ \to J/\psi\phi K^+$ decay: the B^+ is produced in its Primary Vertex (PV) and decays in its Secondary Vertex (SV). Red lines represent the impact parameter of the particles.

tions, are made by using a strategy that aims to get an high signal purity by means a set of selection cuts performed both by the trigger and in the offline analysis. The background reduction is mainly obtained by requiring that daughter particles have an impact parameter (defined as the perpendicular distance between the path of a particle and the primary vertex) greater than zero; while the precision on mass measurement is obtained by considering the particle track quality and constraining the $\mu^+\mu^-$ invariant mass to J/ψ mass nominal value (figure 3.4).
Finally, for an optimal signal/background separation, a multivariate analysis is performed and the high purity of the sample allows us to reduce the statistic error.

3.3 Data sample and Monte Carlo simulation

The analysis is performed by using data produced at LHC during its first operating period between 2010 and 2013 when Run I took place. Thanks to the large beauty and charm production cross-section, during these years LHCb collected about 10^{12} heavy flavor decays. The Data sample comes from full 2012 and 2011 statistics, that means about 3.2 fb^{-1}: $\sim$ 2.1 fb^{-1} at $\sqrt{s} = 8$ TeV center-of-mass energy in 2012 with $\sigma_{b\bar{b}} \simeq 300$ μb [113] and $\sim$ 1.1 at $\sqrt{s} = 7$ TeV in 2011 with $\sigma_{b\bar{b}} \simeq 280$ μb[112] (figure 3.5).
As described in 2.2.1, LHCb magnet deflects particles in x-z plane. Since positive and negative particles are deflected in opposite directions, charge detection asymmetries could occur because of a difference in performance of the left and right sides of the detector. In LHCb such detection asymmetry is kept to a precision of 10^{-3} or better. This is achieved by changing the direction of the magnetic field regularly: data sets with different polarity are then combined in order to cancel left-right asymmetries. During the Run I the polarity was inverted about two times per month.
Starting from the integrated Luminosity, it is possible to give an estimate of the number $\mathcal{N}_{accept}$ of B^+ (decaying via the channel used in this study) in the detector acceptance:

$$\mathcal{N}_{accept} = \mathcal{L}_{\text{LHCb}}\, \sigma_{b\bar{b}}\;\, 2F\; B_{B^+\to J/\psi\phi K^+}\; B_{J/\psi\to\mu^+\mu^-}\; B_{\phi\to K^+K^-}\; \epsilon_{geom}\,. \tag{3.2}$$

Where:

- $\mathcal{L}_{\text{LHCb}}$ is the LHCb integrated Luminosity between the 2011 and the 2012,
- $\sigma_{b\bar{b}}$ is the $b\bar{b}$ production cross section at Run I condition [112, 113],
- $F = 0.4$ is the probability for a b quark to hadronise in B^+,

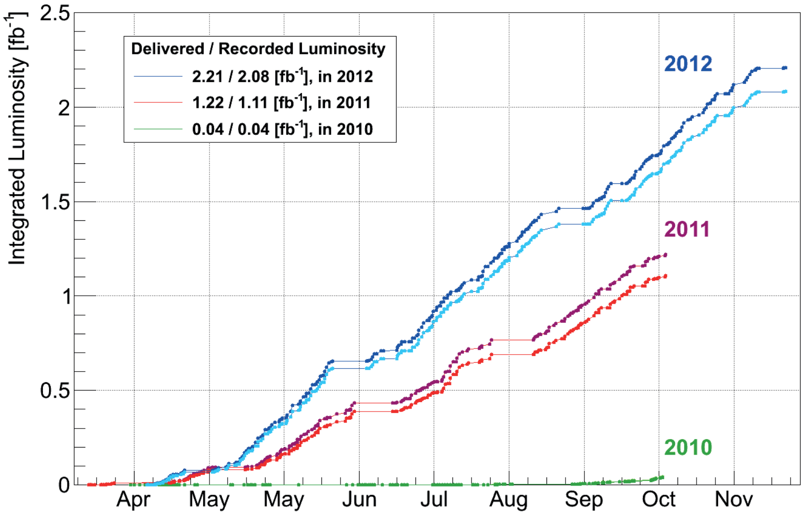

Figure 3.5: LHCb delivered/recorded luminosity

- $B_{B^+\to J/\psi\phi K^+}$ is the Branching Fraction of $B^+ \to J/\psi\phi K^+$ as reported by PDG [93],
- $B_{J/\psi\to\mu^+\mu^-}$ and $B_{\phi\to K^+K^-}$ are the Branching Fraction of $J/\psi \to \mu^+\mu^-$ and $\phi \to K^+K^-$ as reported by PDG [93],
- $\epsilon_{geom} = 15\%$ is the geometrical efficiency of the LHCb detector.

Therefore $\mathcal{N}_{accept}$ can be calculated as follow:

$$\mathcal{N}_{accept} \simeq 3.2\text{fb}^{-1} \times 3 \cdot 10^{11}\text{fb} \times 2 \times 0.4 \times 5.1 \cdot 10^{-5} \times 5.96 \cdot 10^{-2} \times 48.9 \cdot 10^{-2} \times 0.15, \quad (3.3)$$

obtaining

$$\mathcal{N}_{accept} \simeq 1.7 \cdot 10^5 \,. \quad (3.4)$$

Such $\mathcal{N}_{accept}$ are produced among about 10^{11} total B^+ seen in the LHCb acceptance, so the selection of events containing the signal decay is a crucial part of the

analysis.
Simulation is used to estimate the invariant mass distribution of the background processes, to obtain the shape of the signal decays and to obtain the selection efficiency: Monte Carlo (MC) data was produced by means the same reconstruction and stripping versions (the concept of stripping is described in 2.6) that are used for real data.
The so called *Reco14a-Stripping20r1* is created for the 2011 data simulation and the *Reco14a-Stripping20* for the 2012 one. As for the real ones, simulated data are produced both for Magnet Up (MU) and Magnet Down (MD) configuration.
The number of generated signal events for each year of LHCb operation are summarized in the following table:

Table 3.3: MC sample summary table.

LHCb Year operation	Monte Carlo sample
2011	$\sim 1.5 \cdot 10^6$
2012	$\sim 3.0 \cdot 10^6$

3.4 Event Selection

The event selection is designed to maximize the signal candidates and to reject the maximum number of background for each event: an example of a LHCb event is shown in figure 3.6.

First of all they pass through the LHCb trigger requests that select interesting events according to the trigger lines as described in section 2.5, then they go through the LHCb offline analysis and a first preselection. Finally they pass the specific selection made for the analysis and a reduced number of the initial events containing the signal yields with a background contamination is obtained.

3.4.1 Trigger lines

Events are selected by the hardware triggers requiring a single muon or a muon pair with transverse momentum $p_t > 1.48$ GeV/c for 2011 data and $p_t > 1.76$ GeV/c for 2012 data; a muon pair with product of transverse momenta greater than $(1.3\text{GeV}/c)^2$ for 2011 data and $(1.6\text{GeV}/c)^2$ for 2012 data.

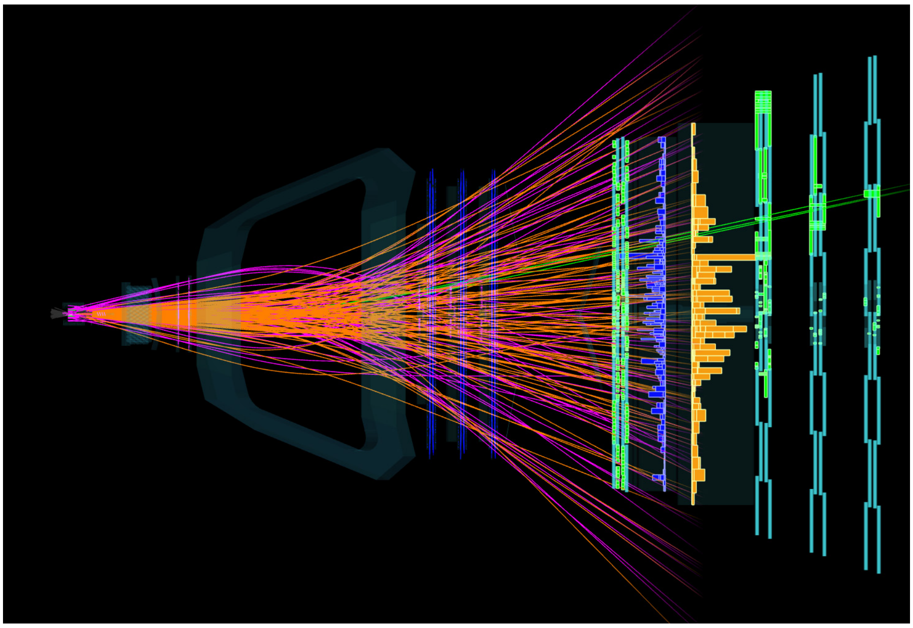

Figure 3.6: Example of an event reconstructed at LHCb (top view of the detector).

At the HLT1 level events are selected that contain two muon tracks with $p_t > 0.5$ GeV$/c$ and invariant mass $m(\mu^+\mu-) > 2.7$ GeV$/c^2$, or a single muon track with $p_t > 1$ GeV$/c$ and χ^2 of the impact parameter (χ^2_{IP}) greater than 16 with respect to any primary vertex (PV). The quantity χ^2_{IP} is the difference between the χ^2 values of a given primary vertex reconstructed with and without the track considered.
The HLT2 stage selects a muon pair with an invariant mass that is consistent with the known J/ψ mass [93], with the effective decay length significance of the reconstructed J/ψ candidate, S_L, greater than 3, where S_L is the distance between the J/ψ vertex and the primary vertex, divided by its uncertainty.

3.4.2 Offline analysis

The offline analysis is made using the LHCb software described in section 2.6. After the offline reconstruction of either simulated or real data made by the **BRUNEL** package, the **DaVinci** package is used for the physics analysis.
In the **DaVinci** framework it is possible to make custom selections to the candidates in order to find the decay chains of interest for the specific analysis. Then a **ROOT**

[114] file with ntuples[1] containing the properties of the particles is created.
The decay reconstruction of this analysis was made by requiring that all daughter particles come from the secondary vertex of the decay.
The selection of muons with the detached condition is made by searching them into the stripping line called *FullDSTDiMuonJpsi2MuMuDetachedLine*. Muons contained in such line are selected cutting on the following variables:

- $p_t(\mu^{\pm})$: muon transverse momentum.
- muon TRCHI2DOF: χ^2 per degree of freedom of the track fit.
- muon PIDmu: $\Delta\log(\mu-\pi)$ that is the combined delta-log-likelihood for the given hypothesis related to muons. The mass hypothesis from the RICH detector is consistent with a muon.
- the J/ψ invariant mass is required to lie within ± 100 MeV/c^2 of the nominal J/ψ mass as referred by PDG [93].
- J/ψ VFASPF(VCHI2PDOF): χ^2 per degree of freedom of the end vertex of the particle. This is a requirement that the tracks of the decay products of the J/ψ extrapolate back to a sensible vertex fit for the decay of the J/ψ.
- J/ψ BPVDLS: gets the related vertex of the particle and calculates the decay length significance with respect to that vertex.
- muon BPVIPCHI2(): impact parameter (IP) χ^2 defined as the difference between the χ^2 of the primary vertex (PV) reconstructed with and without the track under consideration. Where the IP is the perpendicular distance between the path of muons and the pp collision vertex, that is the PV (see figure 3.4).

[1] In the **ROOT** framework an ntuple is a list of variables related to the properties of each particle in the decay chain.

The cuts on the stripping line variables are listed in the following table:

Table 3.4: *FullDSTDiMuonJpsi2MuMuDetachedLine* cuts

Variable	**Threshold**
$p_t(\mu^{\pm})$ (MeV/c)	> 550.0
muon TRCHI2DOF	< 5.0
muon PIDmu	> 0.0
$\Delta m(J/\psi)$ (MeV/c^2)	200
J/ψ VFASPF(VCHI2PDOF)	< 20.0
J/ψ BPVDLS	> 3.0
muon BPVIPCHI2()	> 4.0

The last condition in the reconstruction phase is to constrain the $\mu^+\mu^-$ invariant mass to the J/ψ nominal mass value as reported by PDG [93]: this allows us to correct the momentum of the particles and thereby to obtain an improved B^+ mass resolution.

During the reconstruction of the decay process, a set of loose cuts was adopted so that the amount of data to manage in the final analysis is reduced. The cuts conditions are related both to the particles kinematic and to the track and vertex reconstructions. The cut values' choice for any variable was made in order to retain a window large enough so that the number of the events is not substantially reduced: in order to accomplish it a MC sample is studied after the same offline reconstruction used to precess real data is imposed.

In this regard, the variables to take into account are the ones that are well described by the simulation, that is:

- the particle mass,
- the χ^2 per degree of freedom related to the end vertex of a single particle,
- the particle transverse momentum,

- the particle momentum,
- the minimum χ^2 of a particle trajectory to the primary vertex,
- the IP χ^2 of the PV (as previously defined),
- the angle between the momentum of the particle and the direction of flight from the best primary vertex to the decay vertex,
- χ^2 per degree of freedom of the track fit,
- $K^{\pm}$ mass hypothesis from the RICH detector has to be consistent with a Kaon.

In order to optimize the set of cuts, MC distributions both for signal and background are studied.
As an example, particles' transverse momentum p_t distributions for J/ψ, ϕ, K^+ from ϕ, K^+ from B^+ and μ^+ are shown in figures 3.7 and 3.8. (the complete set of distributions are shown in Appendix B): MC background and MC signal distributions are overlapped.
After the offline analysis, the real data distribution of B^+ meson invariant mass is almost completely given by the background and the B^+ resonance peak is totally covered.

In order to improve cuts selection and to achieve an optimal signal/background ratio a specific event selection, divided in two phases, was performed: the first one consists in the event preselection, the second one in using a multivariate analysis method called Boosted Decision Tree (BDT).
Thanks to this kind of technique an optimal signal-background separation could be performed by applying cuts on a set of variables after they are trained over a sample, both for the signal and the background, made by real data or MC events (see Appendix C).
In the next sections the description of each phase is shown.

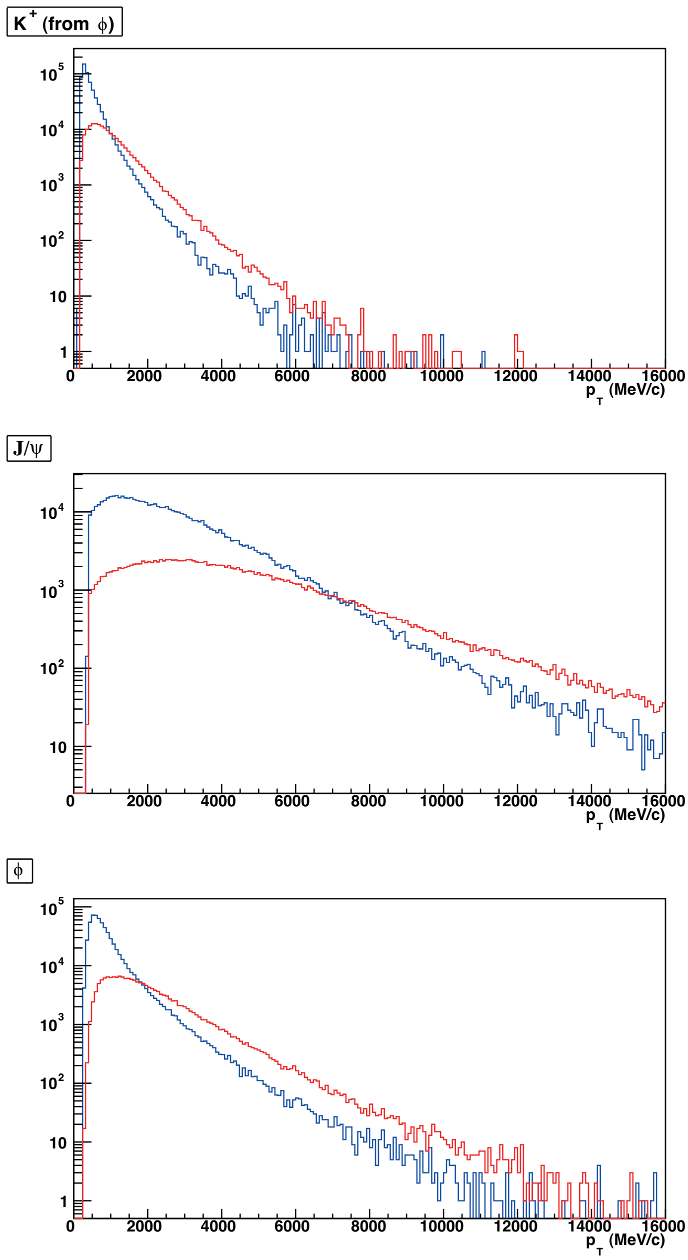

Figure 3.7: p_T distributions of K^+ from ϕ, J/psi and ϕ after loose cuts are applied: MC background (blue) and signal (red) are overlapped.

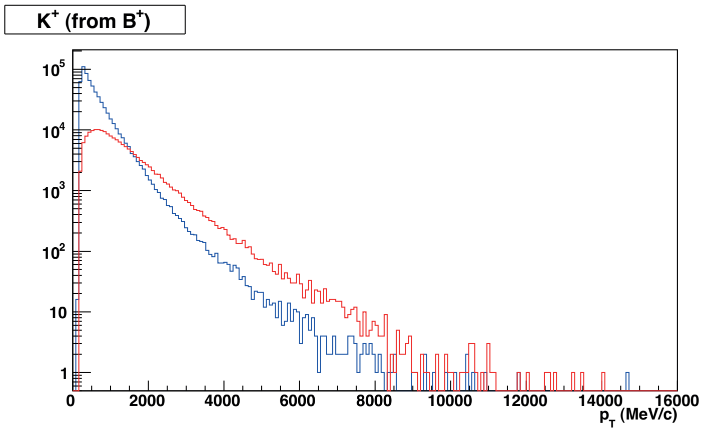

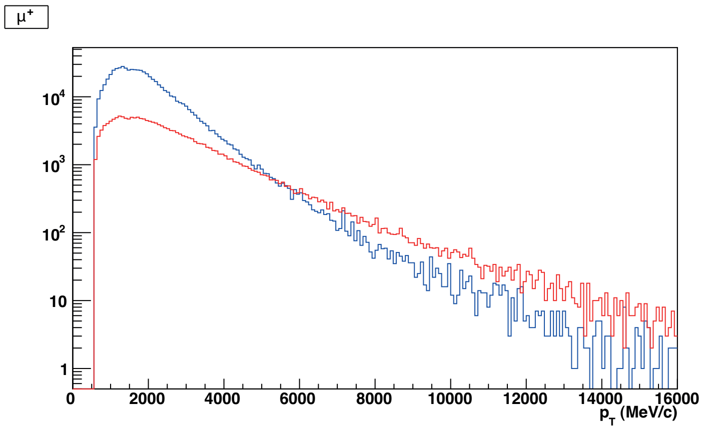

Figure 3.8: p_T distributions of K^+ from B^+ and μ^+ after loose cuts are applied: MC background (blue) and signal (red) are overlapped.

3.4.3 Event preselection

After the offline selection phase a big amount of Real Data events is obtained: about 2×10^7. So, before to perform the multivariate analysis, a further set of cuts has to be applied in order to manage a smaller amount of data.
In the preselection phase a substantial reduction of background events is achieved without to significantly affect the signal. Such result is obtained by analyzing first the B^+ invariant mass spectrum window: according to simulation, it is possible to exclude mass values in the ranges $m(B^+) < 5200$ MeV/c^2 and $m(B^+) > 5360$ MeV/c^2 without to significantly cut the resonance peak tails.
The second selection was made on the K^+K^- invariant mass in order to cut the combinatorial background. Such request is accomplished by choosing a narrow window around to the ϕ mass resonance peak: the aim of this cut is to exclude the tails of the distribution retaining a large fraction of the signal.
The mass region to retain is given by studying the MC K^+K^- signal invariant mass distribution (figure 3.9): the range 1005-1035 MeV/c^2 is chosen obtaining a cut efficiency on signal of about 83%.

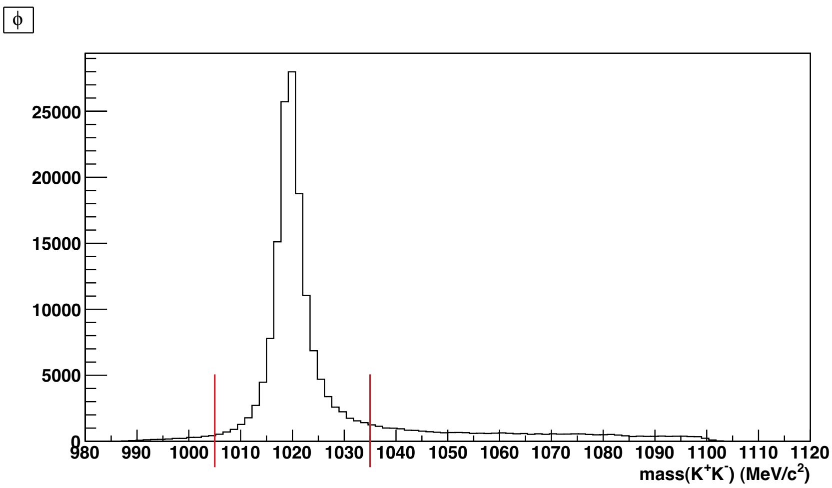

Figure 3.9: MC K^+K^- signal invariant mass distribution (MeV/c^2).

The last selection is related to the track quality of J/ψ and ϕ daughter particles. Due to the high track density in the LHCb detector, during the pattern recognition step many random combination of hits, called ghosts, could be formed (up to 18% of the tracks' samples). In the analysis phase, the probability that a track related to a particle is a fake could be taken into account. The ghost probability is obtained from a dedicated neural network (NN) algorithm trained with simulated data [115]: the misidentified tracks are classified as ghost tracks if they have less than 70% of hits matching the hits of any final state MC particle.
The NN is trained on specific tracks variable, called general variables and specific variables. The first ones are accessible from the track object (they are related to the hits on detectors), while the second ones are built inside the pattern reconstruction algorithms and then written as additional information to the track.
The ghost tracks can be classified in three main types (figure 3.10):

- ghost which have the VeLo track segment not associated to a MC particle,
- ghost that are built with TS track segment identified as ghost,
- ghost made of good VeLo and TS track segments, but with a wrong matching between them.

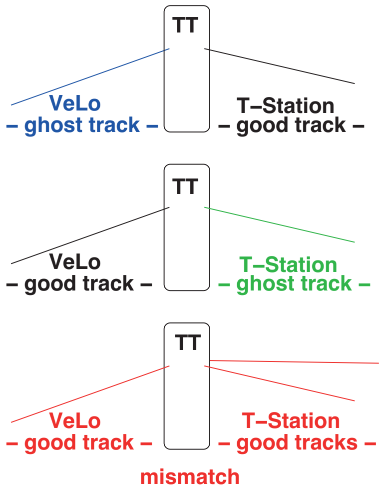

Figure 3.10: Classification of ghost tracks.

The NN returns finally a variable as additional information to the track, containing the ghost probability, called "*particle*_TRACK_GhostProb".

By comparing simulation distributions for signal and background (in figure 3.11 the distributions for K^+ and μ^+ are shown) a cut that preserves the signal and at the same drops the most of background is chosen to be used in the final part of the analysis.

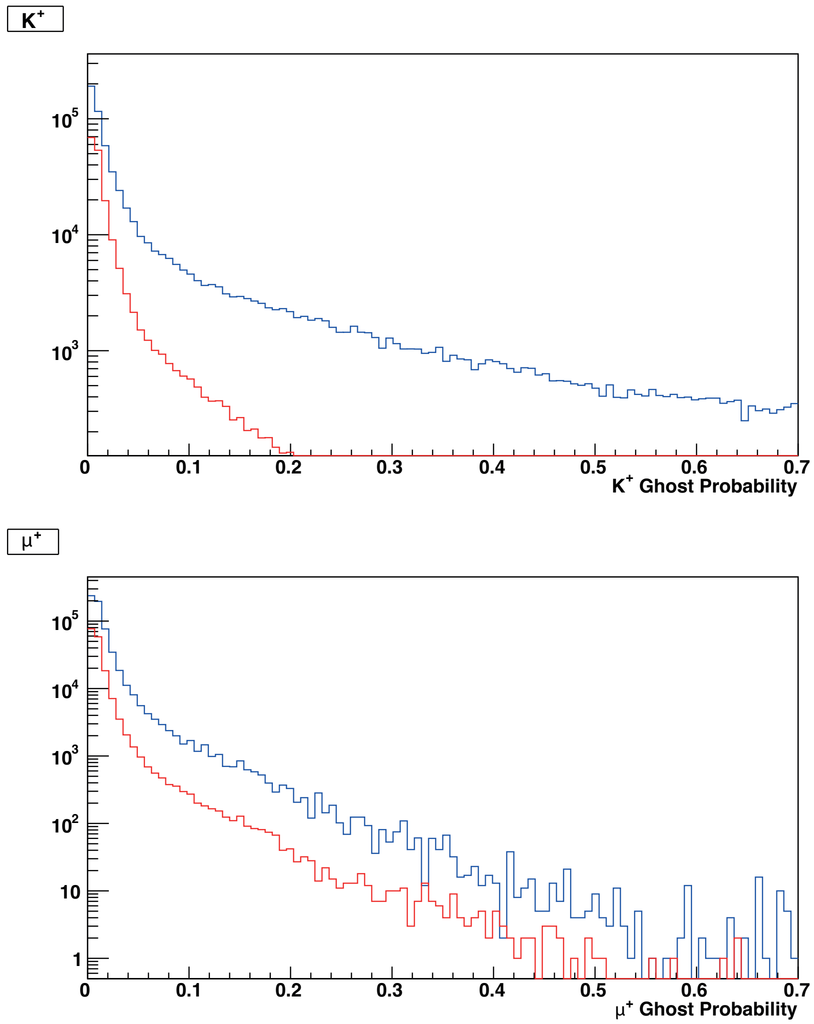

Figure 3.11: Ghost probability distributions related to K^+ and μ^+. MC background (blue) and signal (red) are overlapped.

The chosen selection cuts are finally summarized in the table 3.5.

Table 3.5: Selection cuts.

Variable	**cut**
$\Delta m(B^+)$ (MeV/c^2)	[5200, 5360]
$\Delta m(\phi)$ (MeV/c^2)	[1005, 1035]
$K^{\pm}$ TRACK_GhostProb	< 0.4
$\mu^{\pm}$ TRACK_GhostProb	< 0.4

The selection just described produces the expected effect to sensibly reduce the real data yield obtained after the offline selection: about 4% of the previous sample are in fact left, that is about 8.4×10^5 vs 19.8×10^6.

3.5 Fit model

MC simulation has been used to define the function that better describes the B^+ invariant mass distribution: this is composed by two functions, one used to describe the combinatorial background and the other to represent the B^+ resonance peak. For the background an exponential function, that well fit the background for the distribution under study, was chosen.
The choice for the signal function was made by studying the MC data of the distribution at the end of the preselection phase (figure 3.12).
The mass peak of a resonance is well described by the probability density function (*p.d.f.*) called Crystal Ball (CB) [116, 117, 118]:

$$p(m) \propto \begin{cases} e^{-\frac{1}{2}\left(\frac{m-\mu}{\sigma}\right)^2} & \text{, if } \frac{m-\mu}{\sigma} > -a \\ A\left(B - \frac{m-\mu}{\sigma}\right)^n & \text{, otherwise} \end{cases} \tag{3.5}$$

where m is the measured mass, μ is the resonance mass, σ is the resolution, a is the transition point, A and B are calculated after the continuity of the function and its derivative in a is imposed. This function takes into account the detector response: it consists of a gaussian core and a tail on the left side that parameterizes the effect of photon radiation by the final state particles in the decay. Sometimes is useful to combine two of more CB functions in order to better describe the resonance peak. Since the mass constraint on J/ψ is applied, tails on the mass distribution can be generated due to the photon energy radiated in the $J/\psi \to \mu^+\mu^+$ decay. Hence, even with a perfect detector resolution, the combination of the mass constraint and the

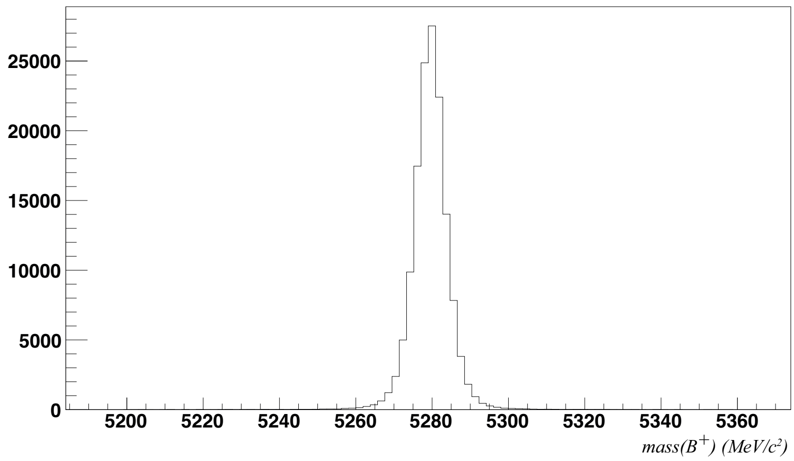

Figure 3.12: MC B^+ invariant mass signal distribution (MeV/c^2) after preselection cuts.

photon radiation will generate non-Gaussian tails. Such effect, even if it expected to be small, sometimes can be well described taking into account the generalization of the CB: an excellent description of mass resolution non-Gaussian tails is the Hypatia distribution, $I(m, \mu, \sigma, p_1, ..., p_7)$ [119] (where m is the free variable (the measured mass), μ is the most probable value (the resonance mass), σ the resolution and p_i are other seven parameters of the function), that corresponds to a CB-like tail with a generalized hyperbolic core. In order to choose the best function for the final fit of real data resonance peak, an extended unbinned maximum likelihood fit both with a Double CB function and with an Hypatia function was performed (figures 3.13) and then the two resulting χ^2/dof were compared (table 3.6).

Table 3.6: Double Crystal Ball and Hypatia fit results.

Fit function	binned χ^2/dof
Double Crystal Ball	2.287
Hypatia	1.188

According to the best binned χ^2/dof the Hypatia function was preferred, while the Double Crystal Ball function is used to define the systematics related to the resonance peak fit.

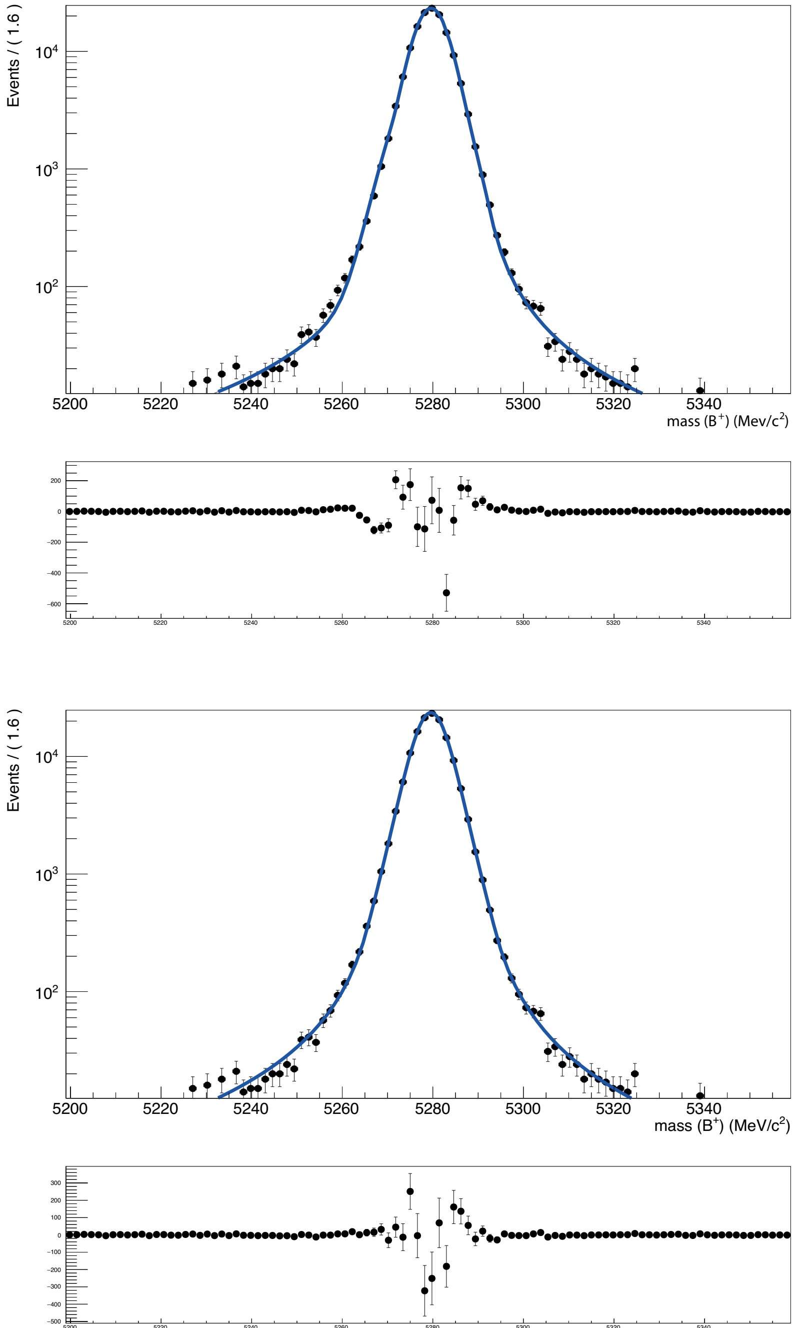

Figure 3.13: MC fit with Double Crystal Ball function and residual distribution (top), MC fit with Hypatia function and residual distribution (bottom).

3.6 Event selection with Boosted Decision Tree (BDT)

After the event preselection, the signal/background discrimination is performed using the Boosted Decision Tree (BDT) procedure as described in Appendix A. Since BDT is trained with background and signal samples, the choice of such samples is a crucial point of the procedure. In our case up to three different combinations of signal/background samples are used: three BDT are then produced named BDT1, BDT2 and BDT3. BDT1 is trained with a MC sample signal and a Real Data sample Background, BDT2 with a MC sample signal and MC sample Background. BDT3 is trained with a Real Data sample Background and with a Real Data sample signal coming from $B^+ \to \psi(2S)K^+$ (with $\psi(2S) \to J/\psi\pi^+\pi^-$, $J/\psi \to \mu^+\mu^-$) decay.

3.6.1 BDT training studies

BDT1

The signal sample used for BDT1 training is obtained by simulation of $B^+ \to J/\psi\phi K^+$ exclusive decay and its invariant mass distribution is shown in figure 3.14. For the background the sample is obtained from Real Data distribution of the decay and then retaining two mass windows corresponding to the sideband of B^+ resonance peak (figure 3.15): the signal in those regions is expected to be negligible and then the sample is almost completely formed by background.
The BDT used for the analysis is built taking in consideration, in the training phase, a set of variables for which there is a good agreement between data and MC distribution. The great advantage on using a multivariate analysis is the possibility to find an optimal cut for a copious number of variable at the same time that should be difficult to perform otherwise.
In order to train this BDT the following 10 variables are used:

- **Bplus_PT**: B^+ transverse momentum.
- **Bplus_DIRA_OWNPV**: the cosine of the angle between the momentum of B^+ and the direction flight from the best PV to the decay vertex. That is the momentum of the B^+ should agree with the flight path between primary vertex and decay vertex.
- **Bplus_IPCHI2_OWNPV**: χ^2 of the impact parameter fit on the related primary vertex.

- **Bplus_ENDVERTEX_CHI2**: χ^2 per degree of freedom of the decay vertex of the B^+.
- **J_psi_1S_PT**: J/ψ transverse momentum.
- **phi_1020_PT**: ϕ transverse momentum.
- **Kplus0_PT**: K^+ (from B^+ decay vertex) transverse momentum.
- **Kplus0_IPCHI2_OWNPV**: χ^2 of the impact parameter fit on the related primary vertex of K^+ (from B^+ decay vertex) trajectory.
- **Kplus_IPCHI2_OWNPV**: χ^2 of the impact parameter fit on the related primary vertex of K^+ (from ϕ decay vertex) trajectory.
- **Kminus_IPCHI2_OWNPV**: χ^2 of the impact parameter fit on the related primary vertex of K^- (from ϕ decay vertex) trajectory.

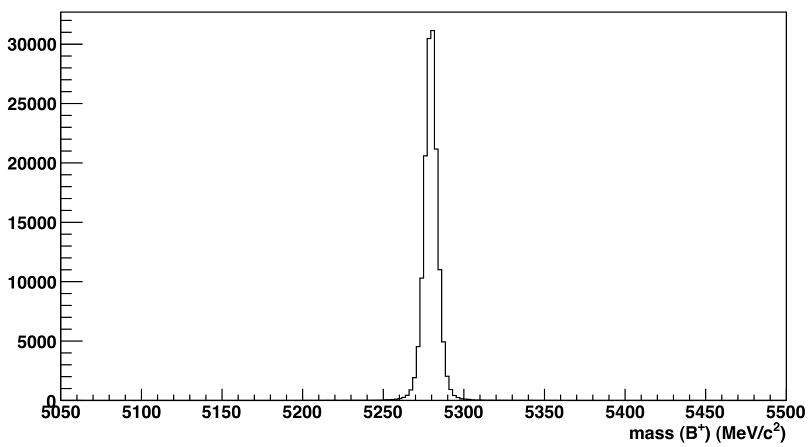

Figure 3.14: Signal sample from MC distribution.

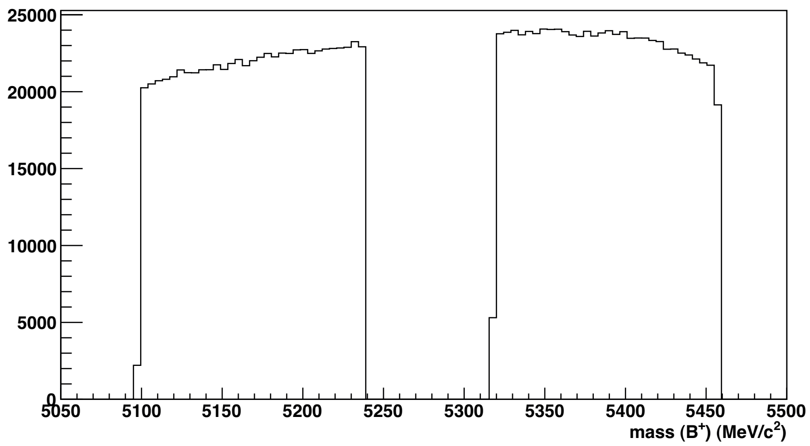

Figure 3.15: Background sample from Real Data distribution.

At the end of the training process signal and background distributions for the ten variables used are generated (figure 3.17).
The final result is the BDT response variable that has a different distribution for signal and background (figure 3.17): such variable is used as a univariate discriminant to distinguish signal from background and so to optimize signal/background separation.

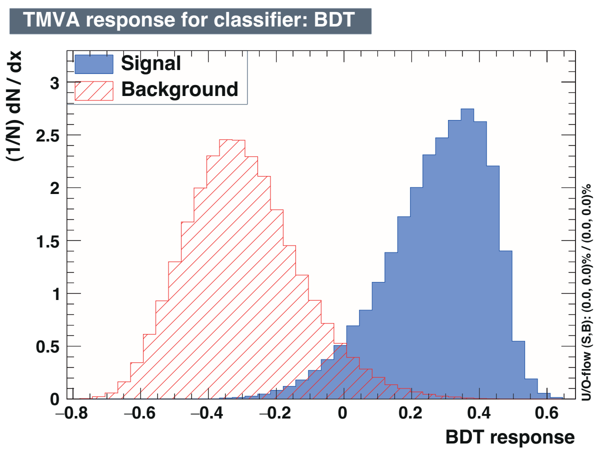

Figure 3.16: BDT1 response output histogram for signal and background.

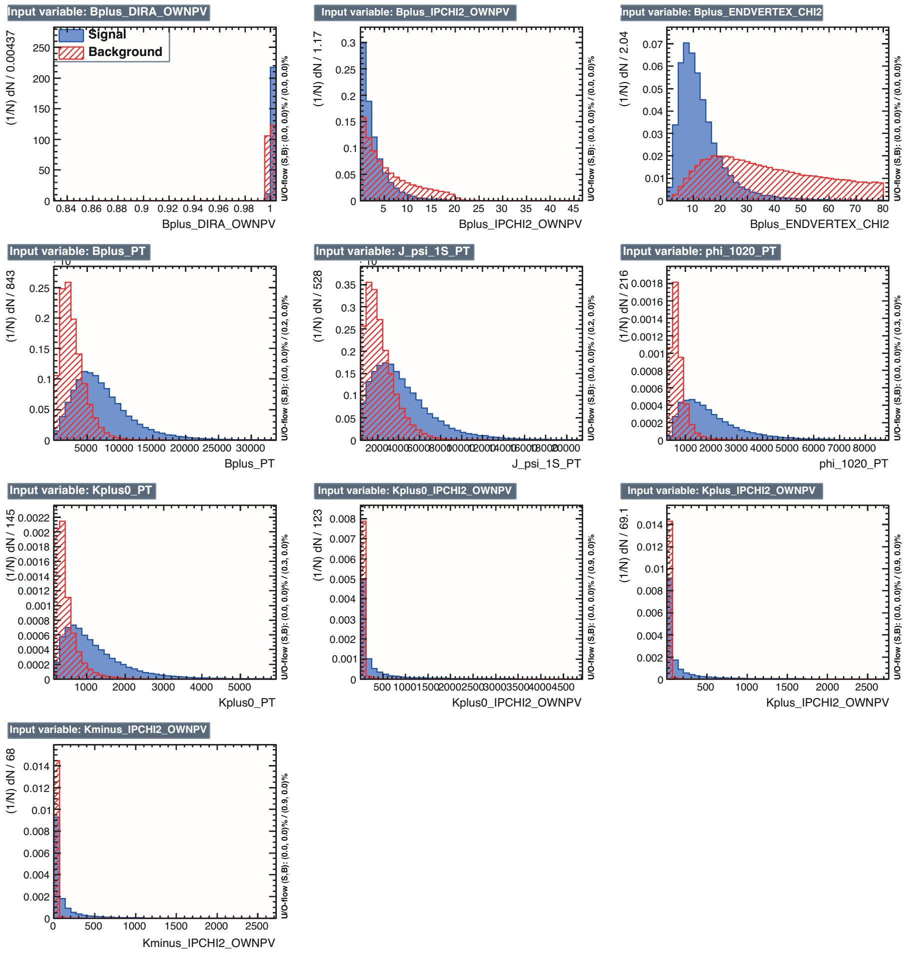

Figure 3.17: Signal and Background distributions for the ten variables used as BDT1 input.

BDT2

MC samples, both for signal and background, are used to train BDT2. For the signal the same distribution for BDT1 is used (figure 3.14), whereas for the Background the simulation of $B_{u,d,s} \to J/\psi X$ inclusive decay with the exclusion of the signal is chosen (figure 3.18). In this case the retained background mass window corresponds to the region of B^+ resonance peak.

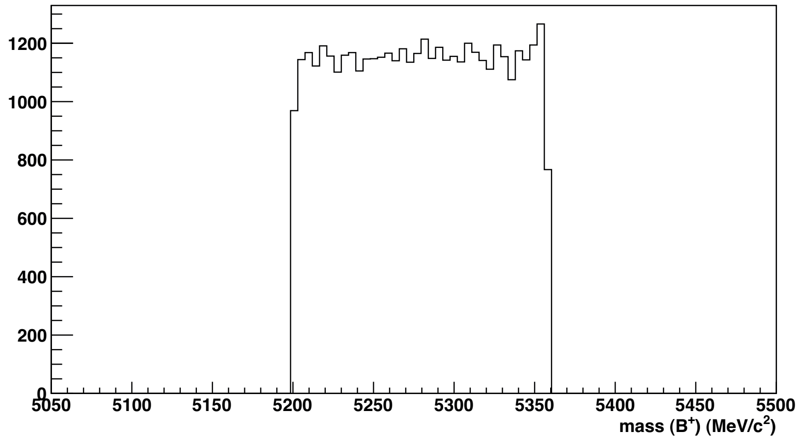

Figure 3.18: Background sample from MC distribution of $B^+ \to J/\psi X$ inclusive decay.

BDT2 is built with the same 10 variables used for BDT1: distributions produced at the end of the training phase are shown in figures 3.19 and 3.20.

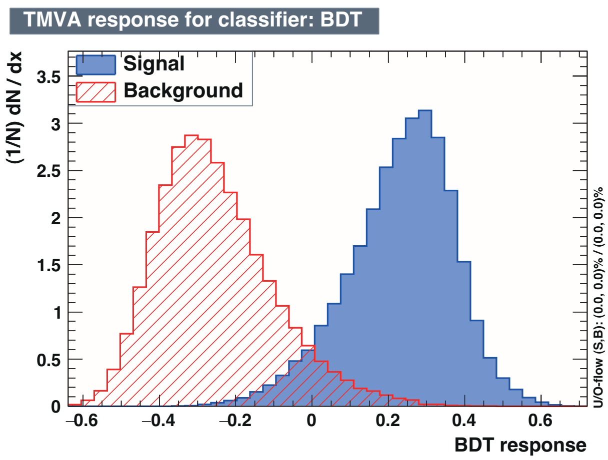

Figure 3.19: BDT2 response output histogram for signal and background.

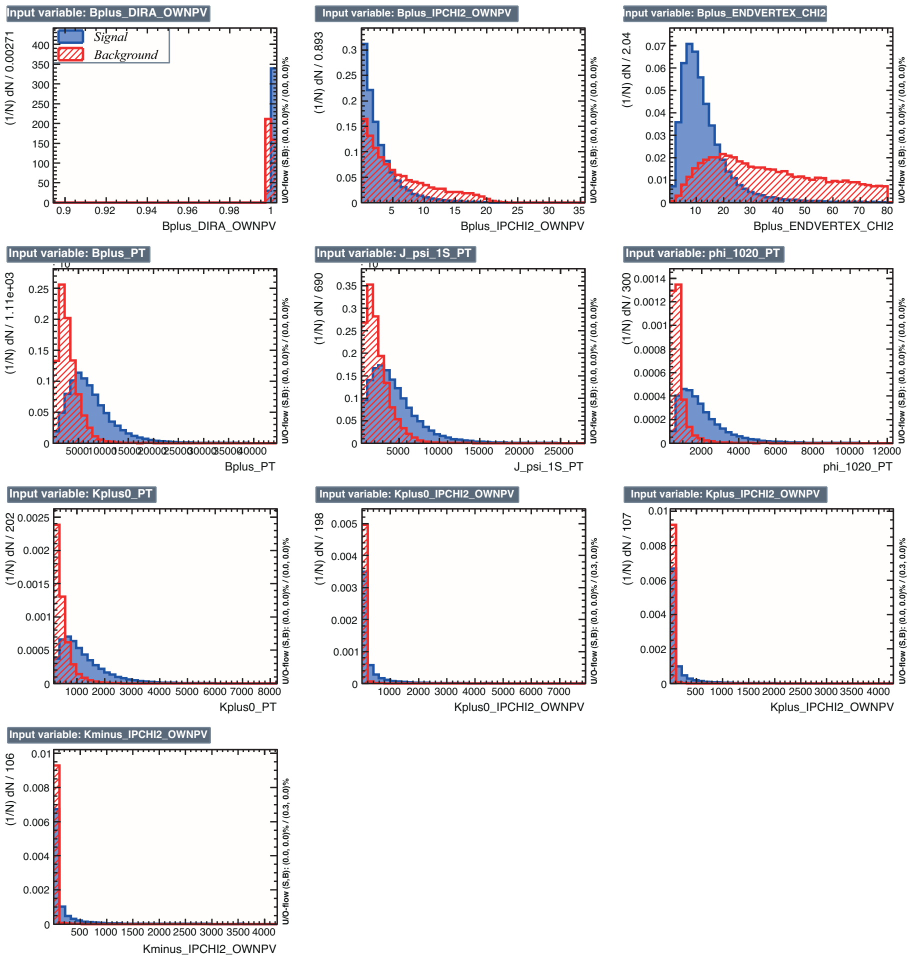

Figure 3.20: Signal and Background distributions for the ten variables used as BDT2 input.

BDT3

This BDT has been trained with Real Data samples both for background and signal. As for BDT1, $B^+ \to J/\psi\phi K^+$ invariant mass Real Data distribution is used for the background (figure 3.15).
For the signal too a Real Data sample was chosen. A good candidate is a channel that has five charged particles in the final state, the same of the decay under

study, a J/ψ and a K^+ as daughter particles. Finally the channel could have a good statistics in order to reduce background/signal ratio in the B^+ resonance peak mass window. For this purpose the decay $B^+ \to \psi(2S)K^+$ (with $\psi(2S) \to J/\psi\pi^+\pi^-$, $J/\psi \to \mu^+\mu^-$) was chosen. The tree level and the penguin diagrams for the decay mode are shown in figure 3.21.

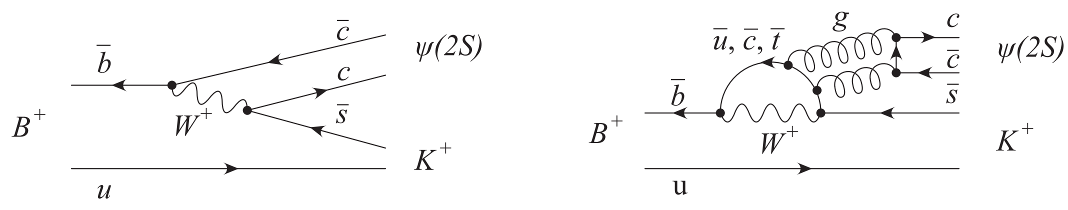

(a) (b)

Figure 3.21: Tree level (a) and Penguin (b) diagram for $B^+ \to \psi(2S)K^+$ decay.

The branching fraction of this channel, BF, is given by [93]

$$BF = BF_{B^+\to\psi(2S)K^+} BF_{\psi(2S)\to J/\psi\pi^+\pi^-} BF_{J/\psi\to\mu^+\mu^-} \simeq 2.2 \cdot 10^{-4} \tag{3.6}$$

that is about 150 times greater than the channel under study.
The main selection cuts adopted for this channel are related to transverse momentum of particles, track quality of primary and secondary vertex particles, K^+ mass hypothesis from the RICH detector is consistent with a Kaon, $\psi(2S)$ mass window, trigger on muons from J/ψ, $\mu^+\mu^-$ invariant mass constrained to J/ψ mass nominal value and are summarized in table 3.7.
After this selection, a B^+ invariant mass distribution with a small background contamination is produced: in this case the multivariate analysis is not necessary to further improve the signal/background ratio. In order to perform the extended unbinned maximum likelihood invariant fit to the invariant mass distribution, a function made by the sum of a Double Crystal Ball (DCB) for the signal and an exponential for the background is used and a binned $\chi^2/dof = 1.63$ is obtained: this value not relevant because the fit is used only to estimate the background of the distribution. In figure 3.22 the result of the fit is visible: the red line is the DCB function, the green one is the exponential and the blue one is the sum of both. As can be seen, the number of background events under the resonance peak is negligible: $background/signal \simeq 2.2 \cdot 10^{-2}$.

Table 3.7: Main selection cuts for $B^+ \to \psi(2S)K^+$ decay.

Variable	**cut**
$p_t(\pi^{+,-})$ (MeV/c)	> 200
$p_t(J/psi)$ (MeV/c)	> 1000
$p_t(K^+)$ (MeV/c)	> 500
$p_t(B^+)$ (MeV/c)	> 3000
B^+ track χ^2 related to Primary Vertex	< 4
$\pi^\pm$, K^+ track χ^2 related to Primary Vertex	> 6
$\pi^\pm$, K^+ TRACK_GhostProb	< 0.3
K^+ PIDK	> 3
$\Delta m(\psi(2S))$ (MeV/c^2)	$[3666, 3706]$

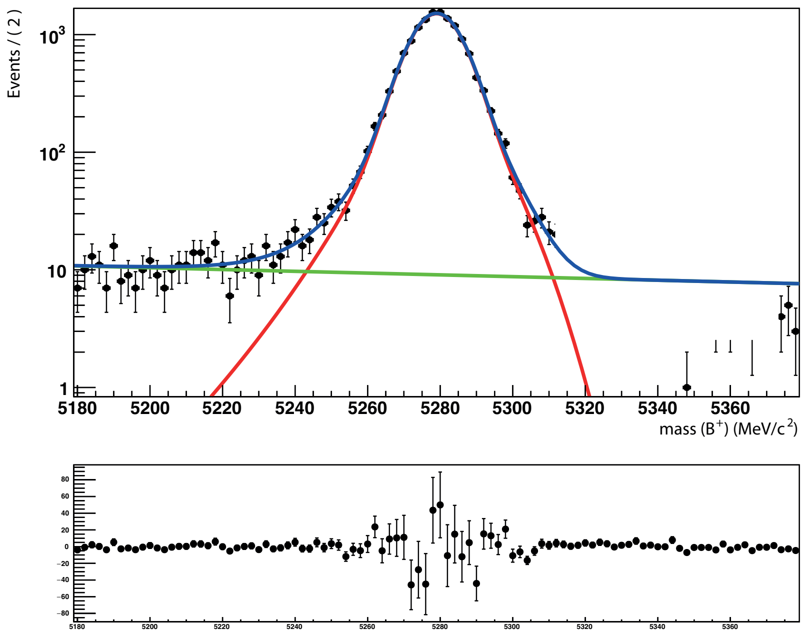

Figure 3.22: Top: fit after selection cuts. Bottom: residual distribution. Red: DCB signal function for the resonance peak. Green: exponential function for the background. Blue: sum of the two functions.

The signal sample for BDT3 is finally obtained by excluding the B^+ mass side-band where the background is not negligible compared to the signal (figure 3.23).

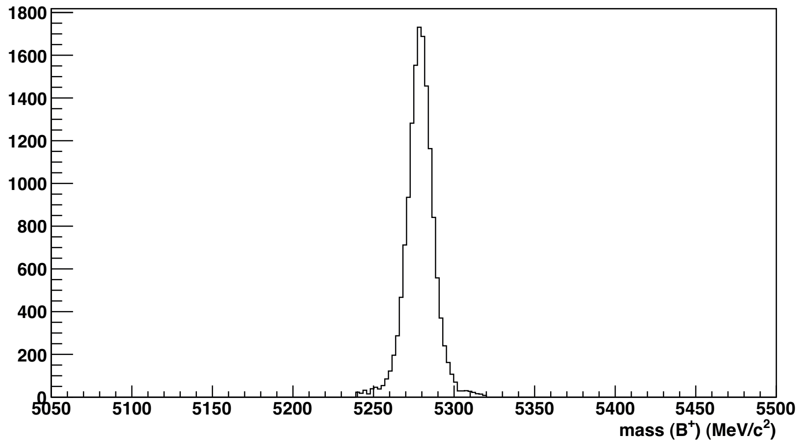

Figure 3.23: Signal sample from $B^+ \to \psi(2S)K^+$ (with $\psi(2S) \to J/\psi\pi^+\pi^-$, $J/\psi \to \mu^+\mu^-$) decay. The retained mass window corresponds to $5239 - 5219$ MeV$/c^2$.

Since background and signal samples come from decays with different particles in the final state, a different set of variables has to be used: in particular, beside the ones related to the particles not in common between the two decays, we decided to exclude the variables related to the K^+ from PV also (since background sample has two K^+ in the final state that could be misidentified in the reconstruction process). BDT3 is built with the following five variables:

- **Bplus_DIRA_OWNPV**.
- **Bplus_IPCHI2_OWNPV**.
- **Bplus_ENDVERTEX_CHI2**.
- **Bplus_PT**.
- **J_psi_1S_PT**.

The distributions produced at the end of the training phase are shown in figures 3.24 3.25.

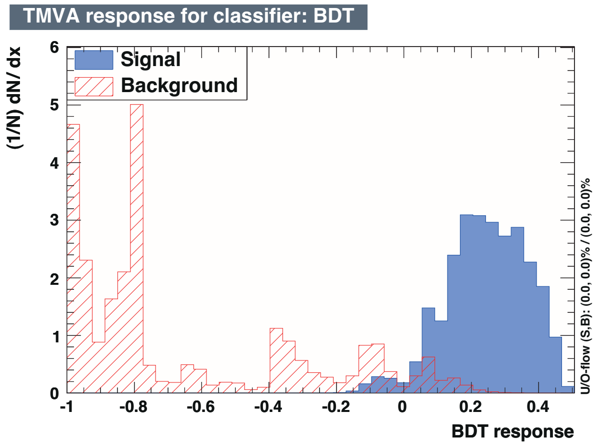

Figure 3.24: BDT3 response output histogram for signal and background.

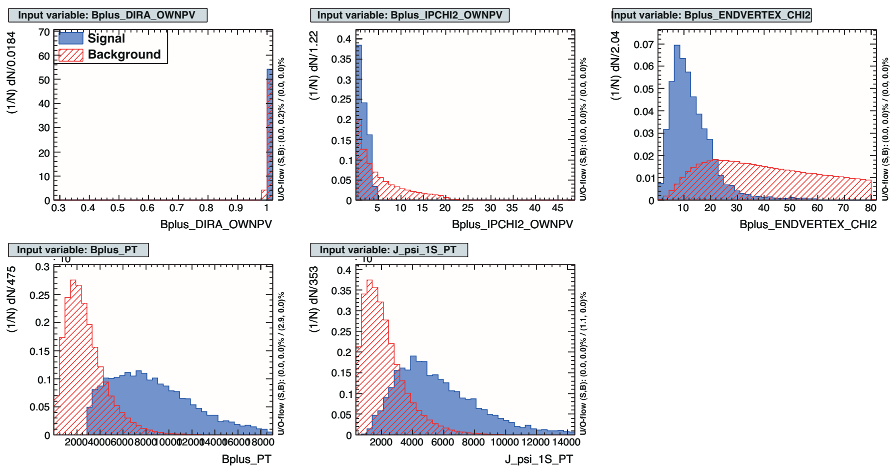

Figure 3.25: Signal and Background distributions for the five variables used as BDT3 input.

BDT results comparison

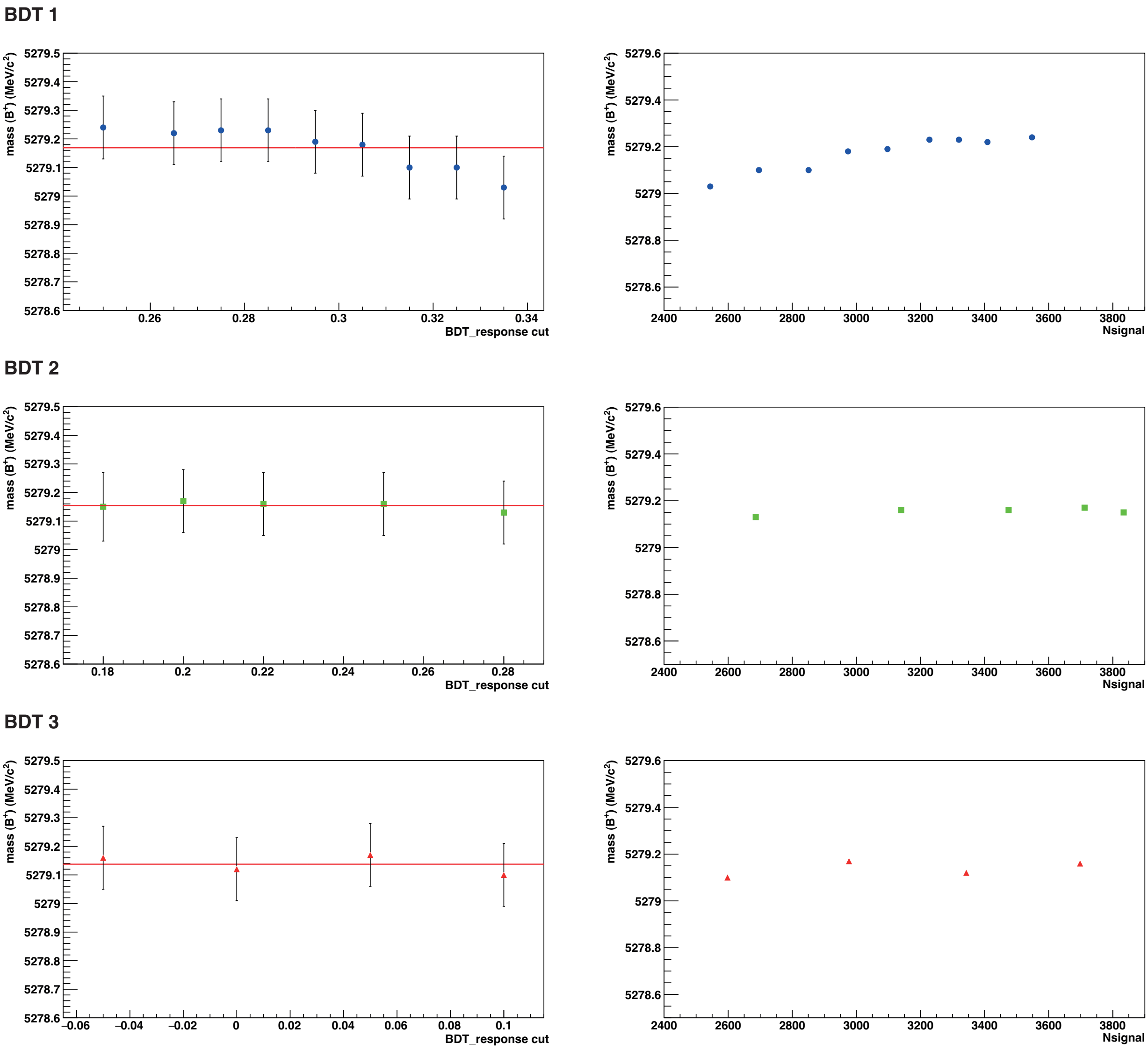

Figure 3.26: BDT results comparison. Top plot: BDT1. Middle plot: BDT2. Bottom plot: BDT3.

In order to define which is the best BDT to use in the analysis, the stability of each BDT as the BDT response cut changes was studied.

This was accomplished by applying the 3 BDTs to Real Data sample and then, after the application of a BDT response set of cuts, by comparing the extended unbinned maximum likelihood fit results: B^+ invariant mass fits with the function described in section 3.5 are performed in order to get the B^+ mass value and the number of signal event. In particular, for a given BDT response cut, the mass mean value as a function of BDT response cut and the mass mean value as a function of signal event number for each BDT are compared.
Figure 3.26 shows that BDT2 and BDT3 are more stable than BDT1.
Finally, BDT2 was preferred to BDT3 thanks to its better stability: the last step is the optimization of BDT response cut.

3.6.2 BDT cut optimization

The BDT response best cut is calculated at the end of the training phase starting from: the Background number, B, before BDT application on the Real Data sample and the number of expected signal events, S. Then it is possible to maximize the Significance, defined as $S/\sqrt{S+B}$ vs the BDT response and get the best cut for the data sample under study.
An estimation of B and S for the Real Data sample has to be now defined.
The entries number is with good approximation the total yield obtained after all the preselection cuts (about $8.3 \cdot 10^5$), being the signal number negligible, while the S number could be evaluated by multiplying the expected number of B^+ produced at LHCb for the MC efficiency of all cuts performed so far.
The S number is so defined as:

$$S = \mathcal{N}_{accept} \times \epsilon_{MC},$$

where $\mathcal{N}_{accept} = 1.7 \cdot 10^5$ as seen in equation 3.4 and ϵ_{MC} is the MC efficiency defined as the ratio between the MC signal number ($N(MC)_{signal}$) after the cuts and the total MC event number before the cuts shown in table 3.3 ($N(MC)_{total}$).
The $N(MC)_{signal}$ number is calculated by the extended unbinned maximum likelihood fit to the whole MC sample, both signal and background, with the function defined in 3.5 (figure 3.27). This is the same technique used for the real data distribution: in this way, including the background too, it is expected to well simulate the shape of data distribution resonance peak, that will be contaminated by not resonant events.

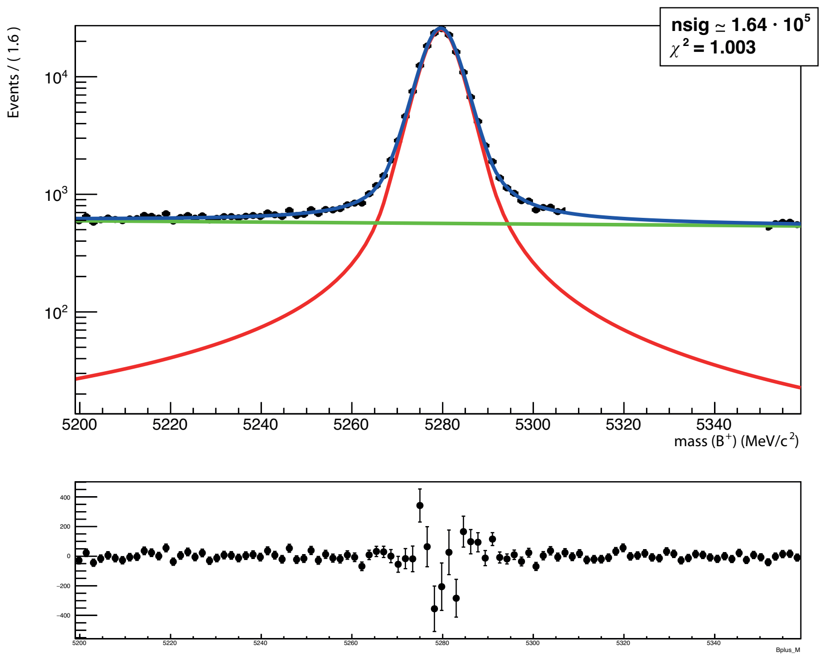

Figure 3.27: Top: invariant B^+ mass (MeV/c^2) MC sample fit after the selection cuts. Bottom: residual distribution. Red: signal function for the resonance peak. Green: exponential function for the background. Blue: sum of the two functions.

From the fit $N(MC)_{signal}$ is about $1.64 \cdot 10^5$ and since $N(MC)_{total}$ is about $4.56 \cdot 10^6$ (see section 3.3) the efficiency results to be:

$$\epsilon_{MC} = \frac{N(MC)_{signal}}{N(MC)_{total}} = 3.6\% \tag{3.7}$$

and finally the S number estimate is obtained:

$$S = \mathcal{N}_{accept} \times \epsilon_{MC} \simeq 6.1 \cdot 10^3. \tag{3.8}$$

According to the plot in figure 3.28 the Significance is maximized for

$$BDTresponse \sim 0.23$$

corresponding to signal a efficiency of about 54% and a negligible background. The signal expected for this value is then calculated as:

$$S_{expected} \simeq 3.3 \cdot 10^3. \tag{3.9}$$

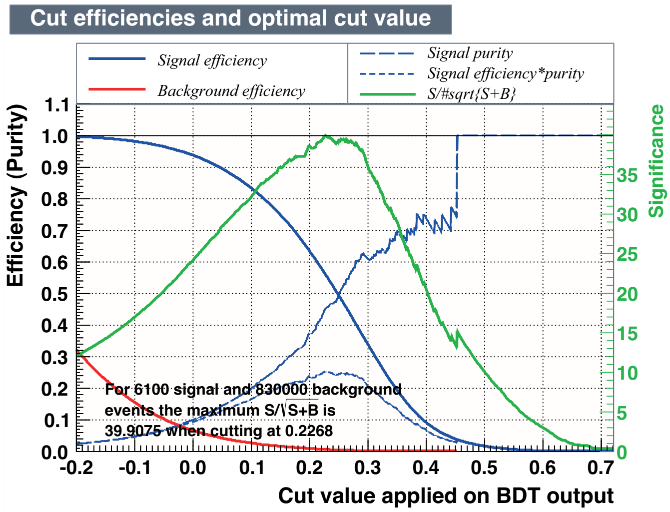

Figure 3.28: Efficiency and significance vs BDT output variable.

After applying the best BDT cut a further cut is performed to refine the event selection. Such cut regards the "multi-candidates" suppressions.
A multi-candidates event could occur when, considering a final state with many particles, the mother particle could be reconstructed by combining the daughter ones in more than one way. In the process under study there is a K^+ in the final state coming from the B^+ decay vertex and a $K^+ - K^-$ pair coming from the decay of the detached ϕ. It could so happen that there is ambiguity between the two K^+ and both could be used once to reconstruct the ϕ particle and once to define the B^+ one. The result of such ambiguity is the possibility to have more than one reconstructed set of particles per event.
The strategy in multi-candidates removing adopted in this analysis consists in keeping only one of the reconstructed sets per event by considering the B^+ mass value first: if two or more candidates have the same B^+ reconstructed mass of them is taken indifferently. After this removal, if other candidates with different masses are

present, one of them is taken randomly. In case of all candidates having different masses, one of them are selected randomly.
The efficiency of this final selection results to be about 96%.
A B^+ invariant mass distribution for real data with a clear visible resonance peak is finally obtained, figure 3.29.
In the next sections I will describe the last part of the analysis, concerning the fitting of the final distribution and the evaluation of systematics uncertainties, leading to the final results.

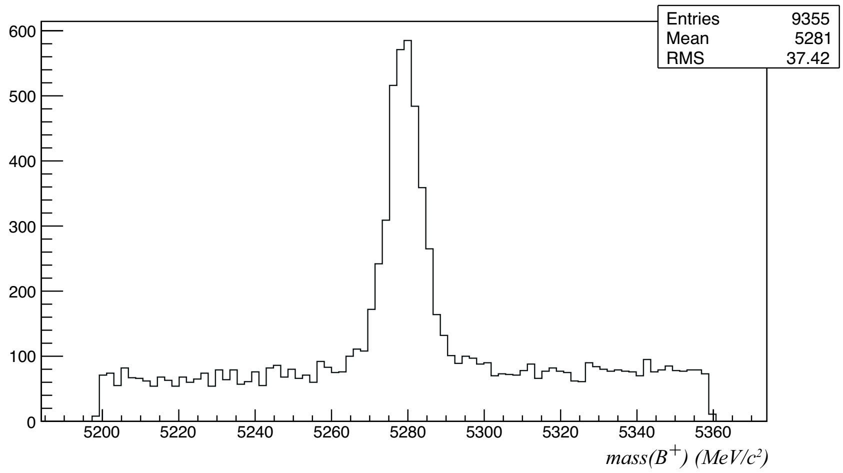

Figure 3.29: B^+ invariant mass distribution (MeV/c^2) after the event selection.

3.7 Results

Once events are selected, extended unbinned maximum likelihood fit to the resulting invariant mass distribution is performed and the B^+ mass and lifetime value with their statistic error are obtained. In this section I will show the fit results obtained after the best fit function choice while in the next one the systematics uncertainties will be discussed.

3.7.1 B^+ invariant mass fit

Before to fit the real data invariant mass distribution of figure 3.29, the parameters that define both Hypatia and DCB functions are fixed to the values obtained from simulation, except for μ and σ. In order to accomplish it, a fit both with signal and background functions, after the application of the best BDT cut, is performed on MC data.
Such values are listed in the following table both Hypatia and double-CB function:

Table 3.8: Hypatia and DCB parameters fixed to values obtained from simulation.

Hypatia parameters	**Value**
$p1$	2.66
$p2$	2.37
$p3$	-2.2457
$p4$	1.37
$p5$	1.83
$p6$	0
$p7$	0
DCB parameters	**Value**
a_{CB1}	-2.2736
a_{CB2}	2.225
n	1.66

Real Data distribution is finally fitted with the function described in section 3.5 that gives a binned $\chi^2 = 86.912$ and $dof = 97$ (using 100 bins): χ^2 probability ($P(\chi^2)$) for such number of degree of freedom is $P(\chi^2) = 0.76$.
Real Data fit is shown in figure 3.30 and in figure 3.31 (where the plot with residual distribution are shown): the red line is the Hypatia function, the green one is the exponential and the blue one is the sum of both.

The B^+ mass value at the end of the analysis results to be:

$$m\left(B^+\right) = 5279.14 \pm 0.11\ \text{MeV}/c^2 \tag{3.10}$$

where the associated error comes only from statistics.

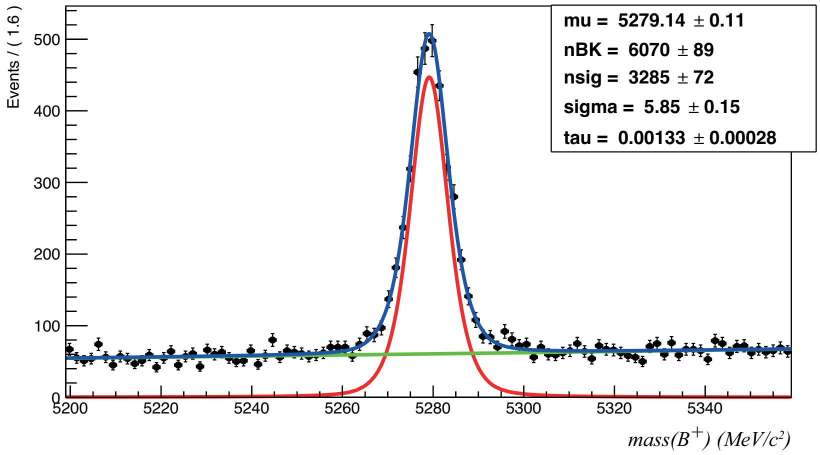

Figure 3.30: Real data B^+ invariant mass distribution (MeV/c^2) final fit. Red: Hypatia function for the resonance peak. Green: exponential function for the background. Blue: sum of the two functions.

After the fit the signal yield number is 3285 ± 72 that is very close to the expected number shown in equation 3.9.
A comparison between MC signal sample and real data distribution of particles transverse momentum was finally done. In order to show that the final distributions are in agreement with simulation, the comparison was made applying a BDT response cut such that: background contamination is negligible, the significance is very close to its maximum value. According to plot in figure 3.28, $BDT\_response > 0.26$ cut was performed.
In figure 3.32 comparison between Real Data (normalized to MC) and MC distributions for the following 6 particles is shown: J/ψ, ϕ, K^+ (from B^+), B^+, K^+ (from ϕ), μ^+.

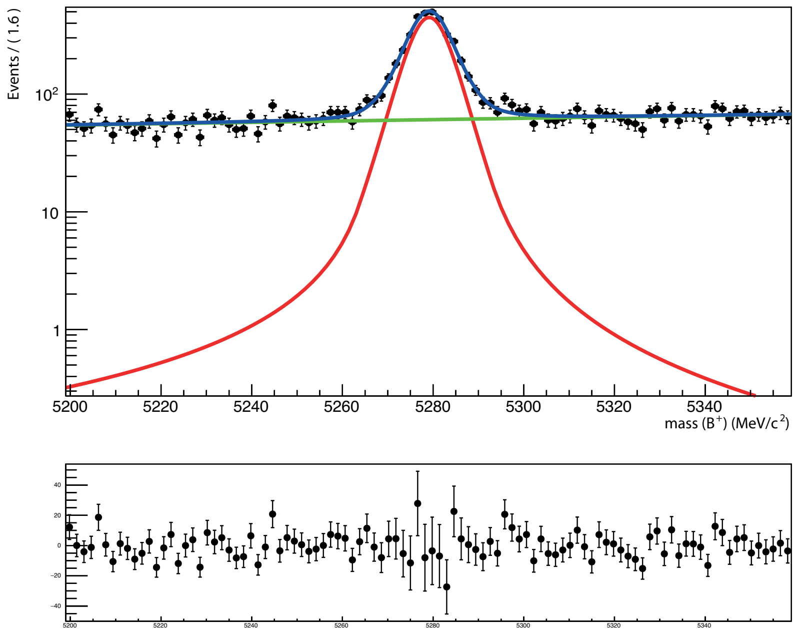

Figure 3.31: Top: Real Data B^+ invariant mass distribution (MeV/c^2) final fit. Bottom: residual distribution. Red: Hypatia function for the resonance peak. Green: exponential function for the background. Blue: sum of the two functions.

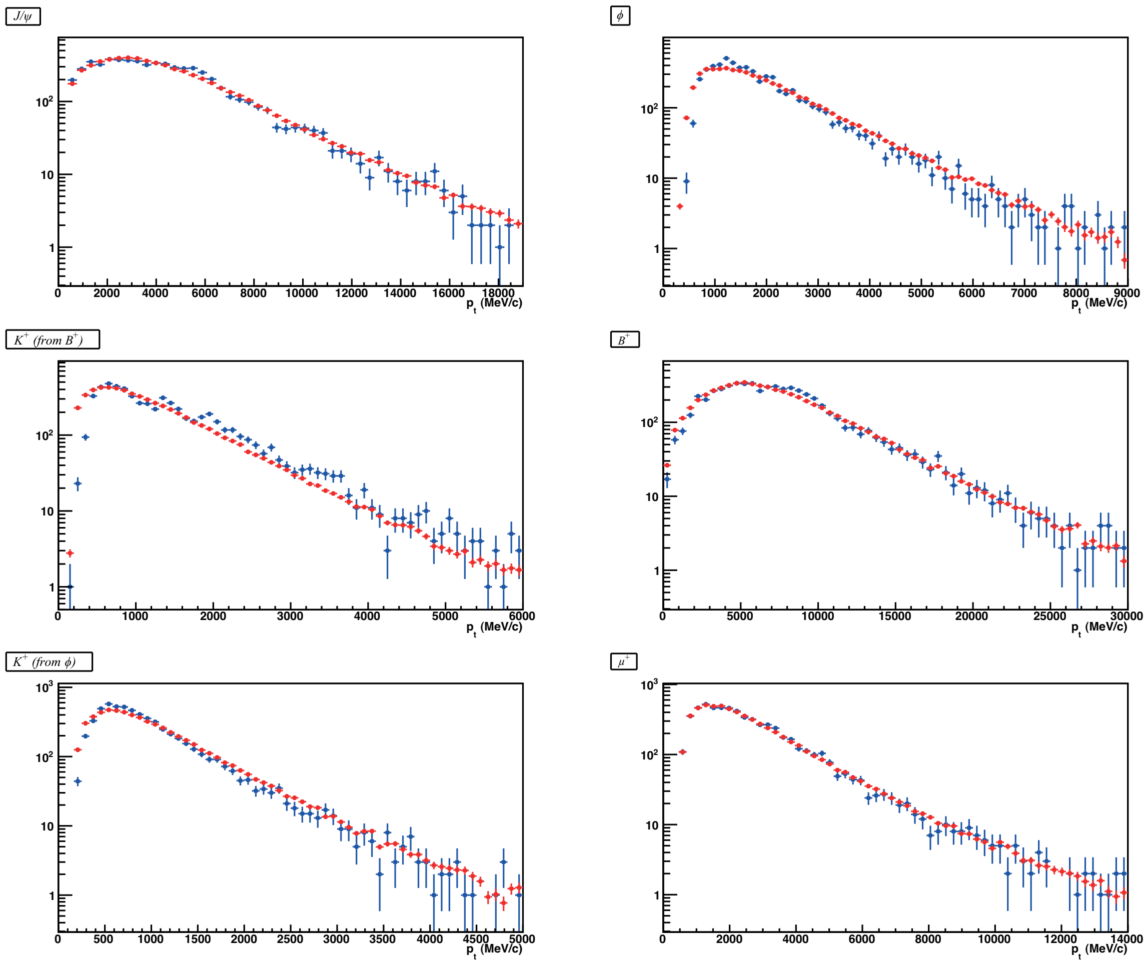

Figure 3.32: p_t distribution plots for J/ψ, ϕ, $K^{\pm}$ and $\mu^{\pm}$. Comparison between normalized to MC Real Data and MC. Blue points: Real Data. Red points: MC.

3.7.2 B^+ lifetime

As a consistency check, B^+ lifetime is evaluated starting from the B meson flight path L in the detector. According to the formula:

$$t = \frac{L}{\beta\gamma c}. \tag{3.11}$$

The B^+ time distribution is given by the combination of the exponential law, formula 3.15, and the detector response. The function $F(t)$ that describes this response is studied with MC simulation and it is defined as the product of an exponential, $T(t)$, and a combination of sigmoid functions, $A(t)$:

$$F(t) = A(t) \times T(t), \tag{3.12}$$

where

$$A(t) = \tanh(s_1 \cdot (t - \theta))^{\alpha} \cdot (\tanh(s_1 \cdot t) + \tanh(s_2 \cdot t)) \tag{3.13}$$

and

$$T(t) = e^{-\frac{t}{\tau}} \tag{3.14}$$

s_1, s_2, θ and α are parameters that are fixed from MC fit.
The last formula describes the time distribution for the signal while the background is evaluated by fit.

The strategy is to study the background from Real Data by retaining the sidebands of B^+ invariant mass distribution, figure 3.30: in this regions the sample is almost completely composed by background events.
Time distributions are evaluated for events belonging to each sideband and then they are compared to verify their agreement (figure 3.33). According to figure 3.30 the background mass distribution results to be almost flat so, being time distributions for sideband in agreement, the distribution under the resonance peak should be in agreement too. It is so reasonable to define the background fit function taking into account the sum of the distributions related to the sidebands only (figure 3.34): the formula describing the background time distribution is obtained from the the product of an exponential and a sigmoid function.

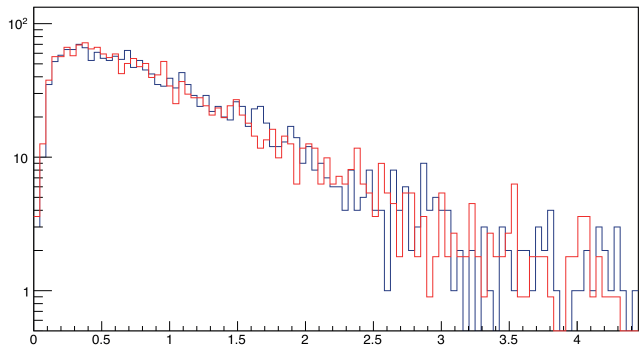

Figure 3.33: Comparison between time distributions for events related to sidebands B^+ invariant mass distribution.

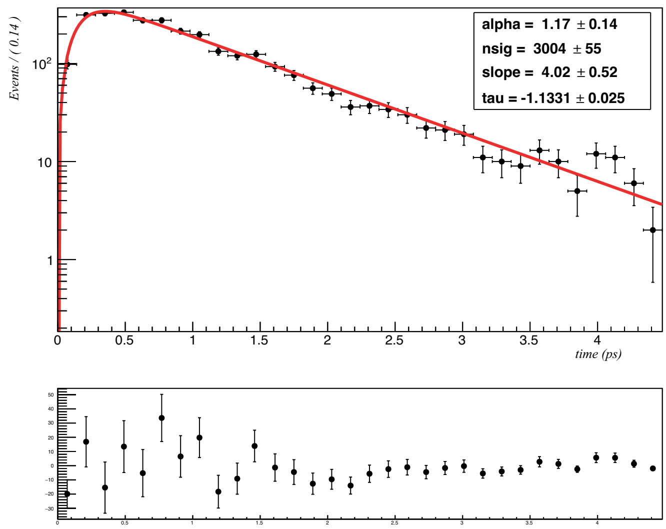

Figure 3.34: Top: background time distribution fit: the distribution is obtained by the sum of the time distributions for events related to sidebands B^+ invariant mass distribution. Bottom: residual distribution.

Finally the time distribution fit ($\chi^2/dof = 1.066$) can be performed using the function resulting from the sum of the signal and the background functions described above (figure 3.35).
Lifetime value is evaluated with statistic error only and it results to be compatible with PDG value $\tau(B^+)_{PDG} = (1.638 \pm 0.004)$ ps [93]:

$$\tau(B^+) = (1.634 \pm 0.082_{stat}) \text{ ps} \tag{3.15}$$

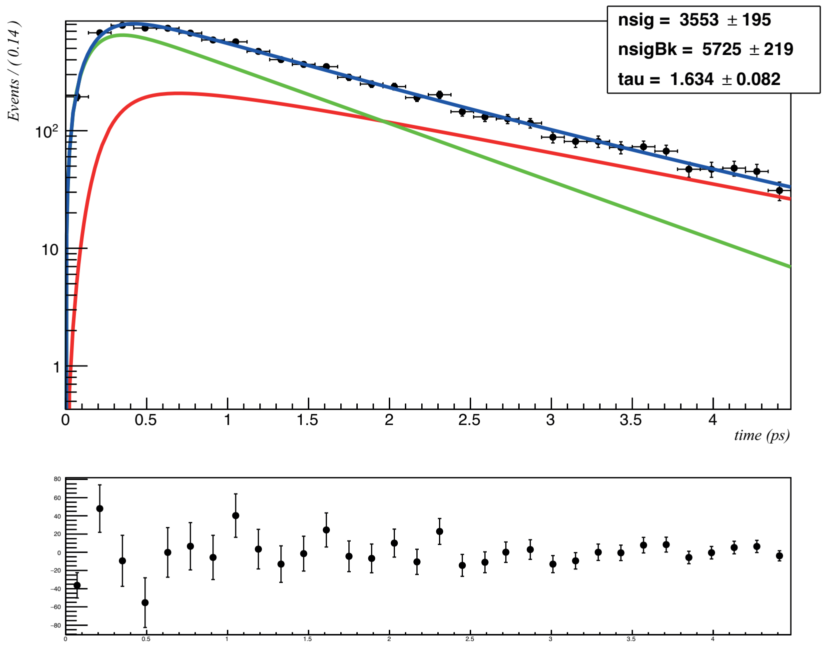

Figure 3.35: Top: time distribution fit. Bottom: residual distribution. Red: function for the signal. Green: function for the background. Blue: sum of the two functions.

3.8 Systematics uncertainties

To evaluate the systematic uncertainty the complete analysis is repeated.
The systematics associated to this measurement are dominated by the limited knowledge of the momentum scale, in addiction other sources are

- the uncertainty related to $K^{\pm}$ meson masses,
- the energy loss of $K^{\pm}$,
- the fit function model,

while systematics from J/ψ mass knowledge are negligible.

3.8.1 K momentum scale

The dominant source of uncertainty is the momentum scale calibration. As discussed before, the momentum scale takes into account the limited knowledge on the detector alignment and, by comparing measured mass values with known values, an uncertainty of 0.03% on the momentum scale is estimated [120]. The mass fits are so repeated with the momentum varied by $\pm 0.03\%$.
The result is visible in figure 3.37 and the systematic error obtained is equal to 0.245 Mev/c^2.

3.8.2 K mass knowledge

An additional uncertainty arises from the knowledge of the value of the $K^{\pm}$ mass, that is $m_{K^{\pm}} = 493.677 \pm 0.016$ Mev/c^2 [93].
The effect of this uncertainty on the measurements has been evaluated by repeating the mass fit with the $K^{\pm}$ masses varied by its error (fig 3.38).
In this case the value of systematic error is 0.040 Mev/c^2.

3.8.3 K energy loss correction

The energy loss of the kaons is another possible source of bias in the mass measurement. This uncertainty is related to the understanding of the energy loss in the material of the tracking system.
The amount of material traversed in the tracking system by a particle is known to

10% accuracy [121], the magnitude of the energy loss correction in the reconstruction is therefore varied by $\pm 10\%$.
So according to the study reported in [120], where the decay $D \to \phi\pi$ with similar q is analyzed, the value for this systematic is found to be 0.030 MeV/c^2.

3.8.4 Fit model

The last uncertainties arise from the fit model as discussed before. To evaluate the impact of the signal model, the double-CB function is used to fit the signal instead of the Hypatia one (figure 3.36): the fit is performed with all DCB parameters fixed according to the values found in the simulation as discussed in section 3.7.1. The shifts of the mass value observed in this test results to be 0.030 MeV/c^2. So this final systematic uncertainty is assigned.

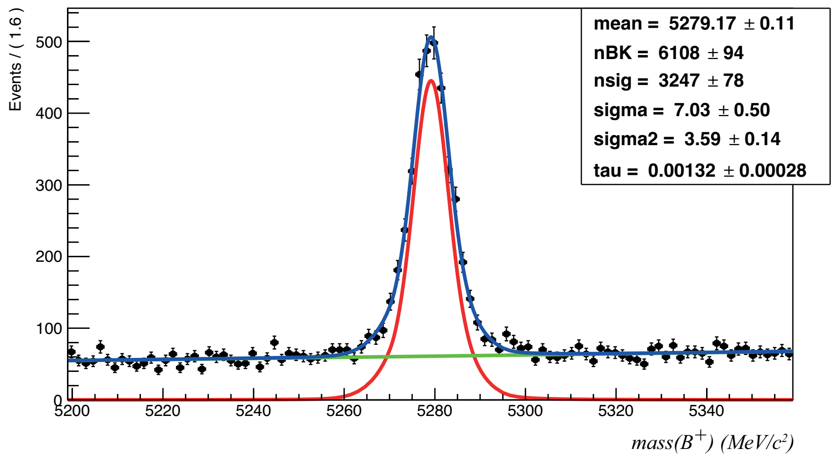

Figure 3.36: B^+ invariant mass fit (MeV/c^2) obtained using the double-CB function for the resonance peak (red) and an exponential function for the background (green). Blue: sum of the two functions.

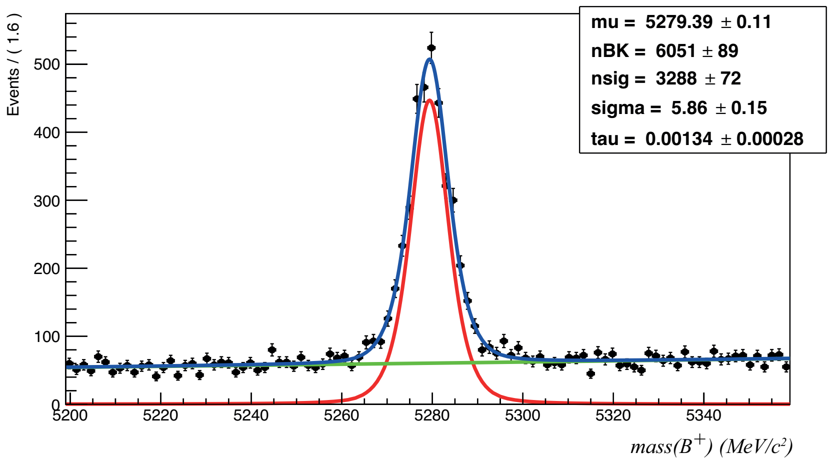

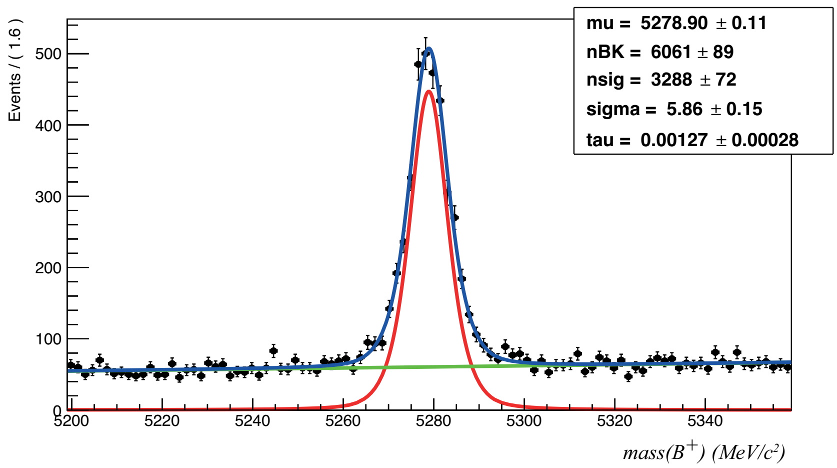

Figure 3.37: B^+ invariant mass fit (MeV/c^2) obtained by varying the momentum scale by $+0.03\%$, top, and -0.03%, bottom.

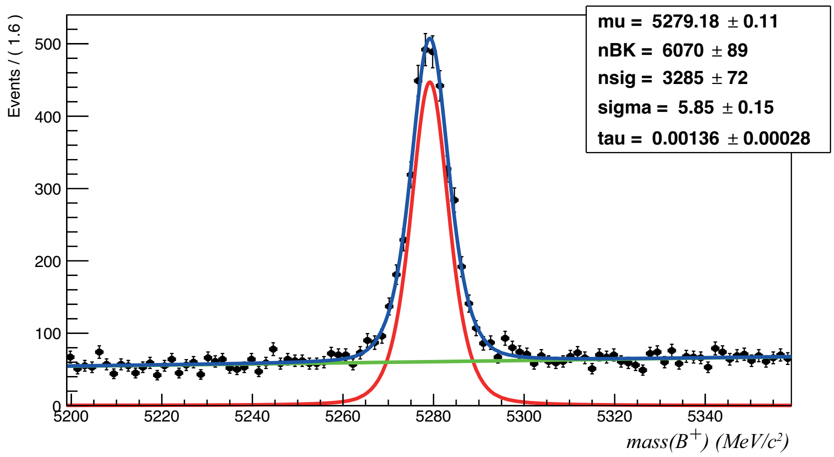

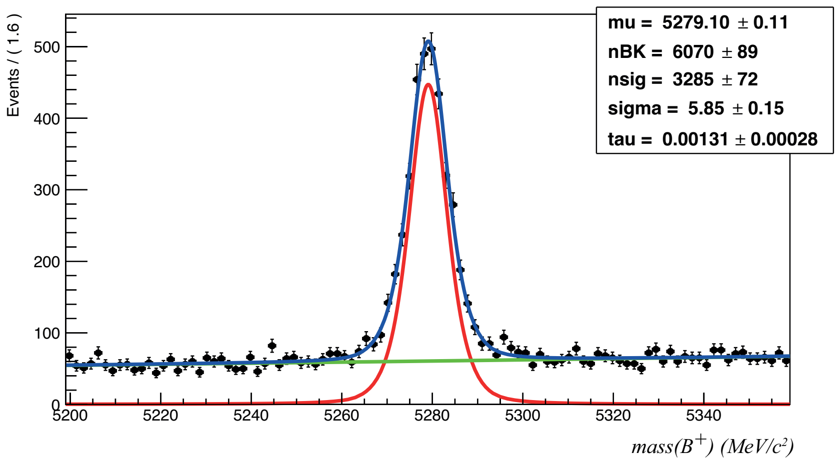

Figure 3.38: B^+ invariant mass fit (MeV/c^2) obtained by varying the $K^{\pm}$ mass value by its error: $+0.016\%$ Mev/c^2, top, and -0.016% Mev/c^2, bottom.

The total systematic uncertainties could be now evaluated as the quadratic sum of the single systematics and results to be 0.25 MeV/c^2:

Table 3.9: Systematic uncertainties (in MeV/c^2) on the mass measurement.

Source of uncertainty	**Value**
Momentum scale	0.245
K mass knowledge	0.040
Energy loss correction	0.030
Fit model	0.030
Quadratic sum	0.250

Conclusions

In the SM framework mesons and baryons are colourless particles composed of quarks and gluons. Quantum chromodynamics (QCD) describes such systems as bounded through the strong interactions.
In this framework the theoretical predictions have to be compared with experimental data in order to verify if QCD is the correct theory of strong interactions.
b physics is considered a stringent Standard Model (SM) test and recent developments in b hadron physics gave significant improvement in experimental determination of Standard Model parameters.
b mass is a fundamental parameter of SM but, since quarks are confined inside hadrons and are not observed as physical particles, it has to be extrapolated by theoretical calculations: a non-perturbative tool formulated on a discrete Euclidean space time grid for calculating the hadronic spectrum and the matrix elements of any operator called lattice QCD (LQCD) has been developed.
One of the purposes of LQCD is to provide predictions on B meson mass starting from b quark value: a fundamental request is that LQCD predictions have to match with experimental data.

Thanks to the high luminosity of LHC, precise $B^{\pm}$ meson mass can be obtained. In this study the $B^{\pm}$ mass measurement has been performed in the $B^{+} \to J/\psi\phi K^{+}$ decay channel using the total 3 fb^{-1} data collected by LHCb during 2011 at a center-of-mass energy $\sqrt{s} = 7$ TeV and 2012 at a center-of-mass energy $\sqrt{s} = 8$ TeV obtaining a signal yield of 3285 ± 72.

From the B^{+} invariant mass distribution fit (figure 3.39) and from systematic uncertainties analysis (value are reported in table 3.10) the mass of $B^{\pm}$ meson is measured to be:

$$m(B^{\pm}) = 5279.14 \pm 0.11_{stat} \pm 0.25_{sys}\ \mathrm{MeV}/c^2.$$

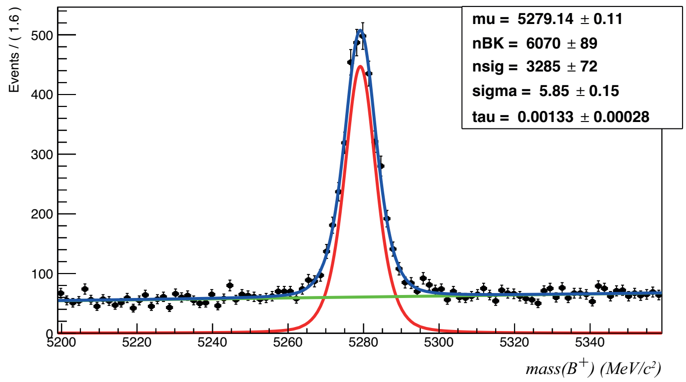

Figure 3.39: Real data B^+ invariant mass distribution (MeV/c^2) final fit. Red: Hypatia function for the resonance peak. Green: exponential function for the background. Blue: sum of the two functions.

Table 3.10: Systematic uncertainties (in MeV/c^2) on the mass measurement.

Source of uncertainty	**Value**
Momentum scale	0.245
K mass knowledge	0.040
Energy loss correction	0.030
Fit model	0.030
Quadratic sum	0.250

This value is in good agreement with the world average and is more precise than the best previous measurement (errors include statistical and systematic uncertainties, all values are in MeV/c^2):

	This analysis	Best previous measurement	PDG average
$m(B^\pm)$	5279.14 ± 0.27	5279.38 ± 0.35 [95]	5279.25 ± 0.26 [93]

Furthermore, since B^0 meson mass is $5279.58 \pm 0.15_{stat} \pm 0.28_{syst}$ (MeV/c^2) (LHCb measure [95]), the mass difference between B^0 and $B^\pm$ obtained in this analysis results to be now grater than experimental errors: last measurements led this difference to be less than experimental errors.
Then, It should be of interest to investigate $B^\pm - B^0$ mass measure.

Appendix A

Neutral B meson properties

As well as for neutral K mesons, B^0 and $\bar{B}^0$ are created by means the strong interaction, but decay by means the weak interaction that doesn't preserve the *beauty* quantum number ($\Delta B = 1$) and can oscillate to their own antiparticles ($\Delta B = 2$). A state that initially is constituted by a superposition of B^0 e $\bar{B}^0$

$$|\Psi(0)\rangle = a(0)|B^0\rangle + b(0)|\bar{B}^0\rangle \,, \tag{3.16}$$

will evolve in time acquiring components that describe all possible final states f_i of the decay, that is:

$$|\Psi(t)\rangle = a(t)|B^0\rangle + b(t)|\bar{B}^0\rangle + \sum_i c_i(t)|f_i\rangle \,, \tag{3.17}$$

and, according to Schroedinger equation:

$$i\hbar\frac{\partial}{\partial t}|\Psi(t)\rangle \ = \mathcal{H}|\Psi(t)\rangle \ . \tag{3.18}$$

We are interested only in $a(t)$ and $b(t)$ and, being the time t we are considering much larger than the typical scale of strong interaction, we can use a simplified formalism [32]. The simplified time evolution is given by a 2×2 not Hermitian effective Hamiltonian (otherwise the b mesons could only oscillate without to decay)

defined as:

$$\mathcal{H} = \mathbf{M} - \frac{i}{2}\Gamma = \begin{pmatrix} M - \frac{i}{2}\mathit{\Gamma} & M_{12} - \frac{i}{2}\mathit{\Gamma}_{12} \\ M_{12}^* - \frac{i}{2}\mathit{\Gamma}_{12}^* & M - \frac{i}{2}\mathit{\Gamma} \end{pmatrix} . \tag{3.19}$$

The diagonal terms describe the B neutral meson decay where M is the mass of the B^0 and $\bar{B}^0$ flavor eigenstate, while $\mathit{\Gamma}$ is the decay width. The off-diagonal terms are

responsible for B^0-$\bar{B}^0$ transitions. M_{12} and Γ_{12} could be calculated from the theory by evaluating the box diagrams in figure 3.40. M_{12} is the decay amplitude related to virtual transitions B^0-$\bar{B}^0$, while Γ_{12} describes the real transitions due to decays that are common to both states, like $\pi^+\pi^-$ o D^+D^-.
Such common decays are Cabibbo suppressed and constitute only a fraction of the

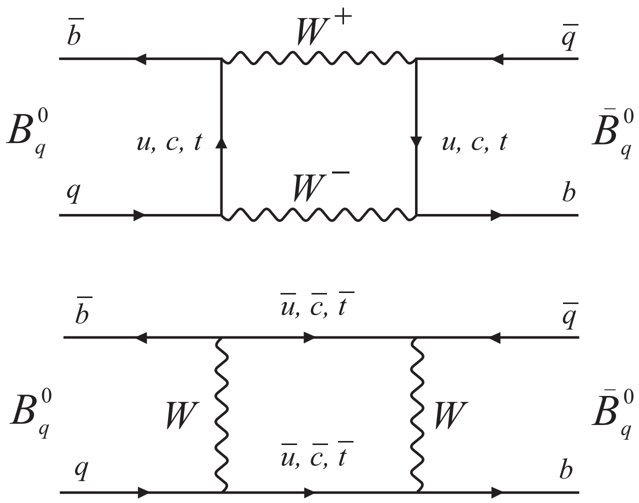

Figure 3.40: Box diagrams describing the B_q^0-$\bar{B}_q^0$ *mixing*, with $q = d, s$

total B decay rate: Γ_{12} in the B^0-$\bar{B}^0$ system could be hence neglected.

The B^0 e $\bar{B}^0$ flavor eigenstates are not CP eigenstates, indeed:

$$\mathrm{CP}|B_0\rangle = -1|\bar{B}_0\rangle \tag{3.20}$$

and

$$\mathrm{CP}|\bar{B}_0\rangle = -1|B_0\rangle\ . \tag{3.21}$$

But, starting from flavor eigenstates, CP eigenstates can be defined as:

$$B_1 = \frac{B_q^0 - \bar{B}_q^0}{\sqrt{2}} \tag{3.22}$$

$$B_2 = \frac{B_q^0 + \bar{B}_q^0}{\sqrt{2}} \tag{3.23}$$

with eigenvalue -1 e $+1$ respectively. Since $[\mathcal{H}, \mathrm{CP}] \neq 0$, the mass eigenstates will be a combination of B_q^0 and $\bar{B}_q^0$ strong eigenstates. Two weak eigenstates, B_L (*Light*) and B_H (*Heavy*), are so defined and are written in the following way:

$$
\begin{aligned}
|B_L\rangle &= p|B_q^0\rangle + q|\bar{B}_q^0\rangle = \frac{1}{\sqrt{1+|\epsilon|^2}}(B_2 + \epsilon B_1) \\
|B_H\rangle &= p|B_q^0\rangle - q|\bar{B}_q^0\rangle = \frac{1}{\sqrt{1+|\epsilon|^2}}(B_1 - \epsilon B_2)
\end{aligned} \tag{3.24}
$$

where p and q are complex coefficients that satisfy the normalization condition

$$|p|^2 + |q|^2 = 1\,.$$

If it happens that

$$\epsilon \neq 0 \rightarrow |q/p| \neq 1$$

indirect CP violation in mixing occurs, given by contamination of B_1 or B_2 in B_L or in B_H.
The eigenvalues $\omega_{H,L}$ of the weak eigenstates could be found by solving the characteristic equation $|\mathcal{H} - \omega I| = 0$:

$$
\begin{aligned}
\omega_{H,L} = M - \frac{i}{2}\mathit{\Gamma} &\pm \sqrt{\left(M_{12} - \frac{i}{2}\mathit{\Gamma}_{12}\right)\left(M_{12}^* - \frac{i}{2}\mathit{\Gamma}_{12}^*\right)} = \\
&= \left(M \pm \frac{\Delta M}{2}\right) - \frac{i}{2}\left(\mathit{\Gamma} \pm \frac{\Delta\Gamma}{2}\right) = M_{H,L} - \frac{i}{2}\Gamma_{H,L}
\end{aligned} \tag{3.25}
$$

where $M_{H,L} = M \pm |M_{12}|$, $\Gamma_{H,L} = \mathit{\Gamma} \mp |\mathit{\Gamma}_{12}|$ e $\Delta M = M_H - M_L$, $\Delta\Gamma = \Gamma_H - \Gamma_L$.
The relation between p and q in the equation 3.24 could be found by solving the eigenvalue problem for $\mathcal{H}$:

$$\left(\frac{q}{p}\right)^2 = \frac{M_{12}^* - \frac{i}{2}\mathit{\Gamma}_{12}^*}{M_{12} - \frac{i}{2}\mathit{\Gamma}_{12}}\,. \tag{3.26}$$

We can now write the time evolution for B_H e B_L eigenstates:

$$
\begin{aligned}
|B_L(t)\rangle &= e^{-i(M_L - \frac{i}{2}\mathit{\Gamma}_L)}(p|B_q^0\rangle + q|\bar{B}_q^0\rangle) \\
|B_H(t)\rangle &= e^{-i(M_H - \frac{i}{2}\mathit{\Gamma}_H)}(p|B_q^0\rangle - q|\bar{B}_q^0\rangle)
\end{aligned} \tag{3.27}
$$

and, from equation (3.24), the relation between flavor and mass eigenstates is:

$$
\begin{aligned}
|B_q^0\rangle &= \frac{1}{2p}[|B_H\rangle + |B_L\rangle] \\
|\bar{B}_q^0\rangle &= \frac{1}{2q}[-|B_H\rangle + |B_L\rangle]
\end{aligned} \tag{3.28}
$$

so the time evolution of a defined flavor state, B^0_q or $\bar{B}^0_q$, is given by:

$$
\begin{aligned}
|B^0_q(t)\rangle &= g_+(t)|B^0_q\rangle + g_-(t)\frac{q}{p}|\bar{B}^0_q\rangle \\
|\bar{B}^0_q(t)\rangle &= g_-(t)\frac{p}{q}|B^0_q\rangle + g_+(t)|\bar{B}^0_q\rangle
\end{aligned} \tag{3.29}
$$

with $g_\pm(t)$ defined as:

$$
g_\pm(t) = \frac{1}{2}[e^{-i(M_H-\frac{i}{2}\Gamma_H)t} \pm e^{-i(M_L-\frac{i}{2}\Gamma_L)t}]\,. \tag{3.30}
$$

By means these equations it is possible to write the probability to find a B^0_q or a $\bar{B}^0_q$ at time t starting from an initial state B^0_q:

$$
\begin{aligned}
|\langle B^0_q|B^0_q(t)\rangle|^2 &= |g_+(t)|^2 \\
|\langle \bar{B}^0_q|B^0_q(t)\rangle|^2 &= \left|g_-(t)\frac{q}{p}\right|^2
\end{aligned} \tag{3.31}
$$

and from an initial state $\bar{B}^0_q$:

$$
\begin{aligned}
|\langle B^0_q|\bar{B}^0_q(t)\rangle|^2 &= \left|g_-(t)\frac{p}{q}\right|^2 \\
|\langle \bar{B}^0_q|\bar{B}^0_q(t)\rangle|^2 &= |g_+(t)|^2\,.
\end{aligned} \tag{3.32}
$$

For the B^0_d-$\bar{B}^0_d$ and B^0_s-$\bar{B}^0_s$ systems the SM predicts that the ratio $\frac{\Delta\Gamma_d}{\Gamma_d}$ is very small (below 1%), while $\frac{\Delta\Gamma_s}{\Gamma_s}$ is much more larger ($\sim$ 10%) [20]. These differences are caused by the fact that there are final states to which both B^0_q and $\bar{B}^0_q$ mesons can decay: such decays involve $b \to c\bar{c}q$ transitions that are Cabibbo-suppressed if $q = d$ and Cabibbo-allowed if $q = s$.
If we define the mixing parameter as $x_q = \frac{\Delta M}{\bar{\Gamma}}$ (with $\bar{\Gamma} = \frac{\Gamma_H+\Gamma_L}{2}$), we find from experimental data [20]:

$$
\begin{aligned}
x_d &= 0.774 \pm 0.006 \\
x_s &= 26.85 \ \pm 0.13\,.
\end{aligned} \tag{3.33}
$$

So, for both B^0_d and B^0_s, $\Delta M \ll \Delta\Gamma$, hence $\Gamma_{12} \ll M_{12}$. It follows that:

$$
\begin{aligned}
\frac{q}{p} &\simeq -\frac{M^*_{12}}{M_{12}}\left(1 - \frac{1}{2}Im\left[\frac{\Gamma_{12}}{M_{12}}\right]\right) \\
\left|\frac{q}{p}\right| &\simeq 1 - \mathcal{O}(10^{-3})\,.
\end{aligned} \tag{3.34}
$$

Hence the CP indirect violation for $\Delta B = 2$ transitions in mixing is a very small effect.

Appendix B

Loose cuts distribution plots

- **particles mass**
- **VFASPF(VCHI2PDOF)**: χ^2 per degree of freedom of the end vertex of the particle
- **particles transverse momentum** p_T
- **particles momentum** p
- **MIPCHI2DV(PRIMARY)**: minimum χ^2 distance of a particles's trajectory to any set of vertices
- **BPVIPCHI2()**: χ^2 Impact Parameter (IP) on the related Primary Vertex (PV)
- **BPVDIRA**: the cosine of the angle between the momentum of the particle and the direction fo flight from the best PV to the decay vertex.
- **TRCHI2DOF**: χ^2 per degree of freedom of the track fit
- **PIDmu**: $\Delta \log(\mu - \pi)$ that is the combined delta-log-likelihood for the given hypothesis related to muons
- **PIDK**: $\Delta \log(K - \pi)$ that is the combined delta-log-likelihood for the given hypothesis related to Kaons

The set of cuts visible in table 3.11 is chosen.

Table 3.11: List of loose cut for each variable.

Variable	**cut**
$mass(\phi)$ (MeV/c^2)	$980 \div 1100$
VFASPF(VCHI2PDOF)(ϕ)	< 9
$P_T(K)$ (MeV/c)	> 200
$P_T(\phi)$ (MeV/c)	> 300
$P_T(J/\psi)$ (MeV/c)	> 400
MIPCHI2DV(PRIMARY)(K^+ from B^+)	> 4
$mass(B^+)$ (MeV/c^2)	$5000 \div 5500$
VFASPF(VCHI2PDOF)(B^+)	< 10
BPVIPCHI2()(B^+)	< 20
BPVDIRA(B^+)	> 0.9995
TRCHI2DOF(K, μ)	< 3
P(μ) (GeV/c)	> 5.0
$P_T(\mu)$ (MeV/c)	> 600
PIDK(K from ϕ)	> 0

The complete set of distributions for each variable obtained after the offline cuts is shown.

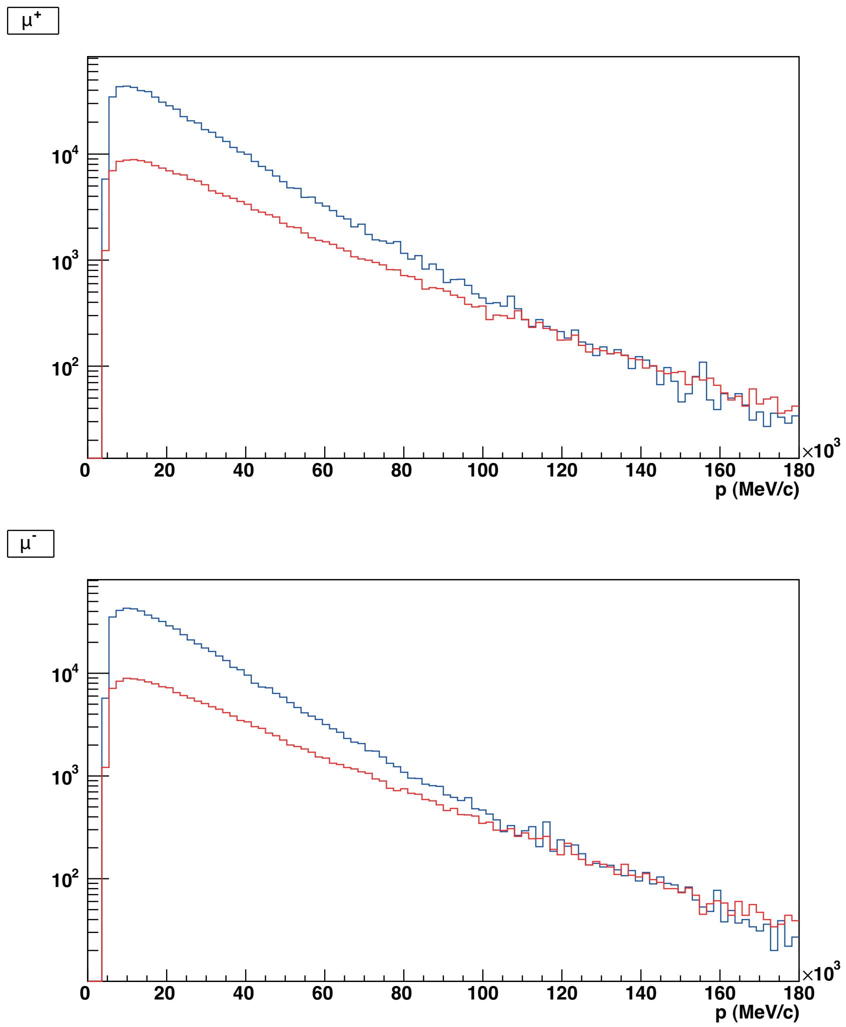

Figure 3.41: Distributions of kinematic variables after loose cuts are applied: MC background (blue) and signal (red) are overlapped.

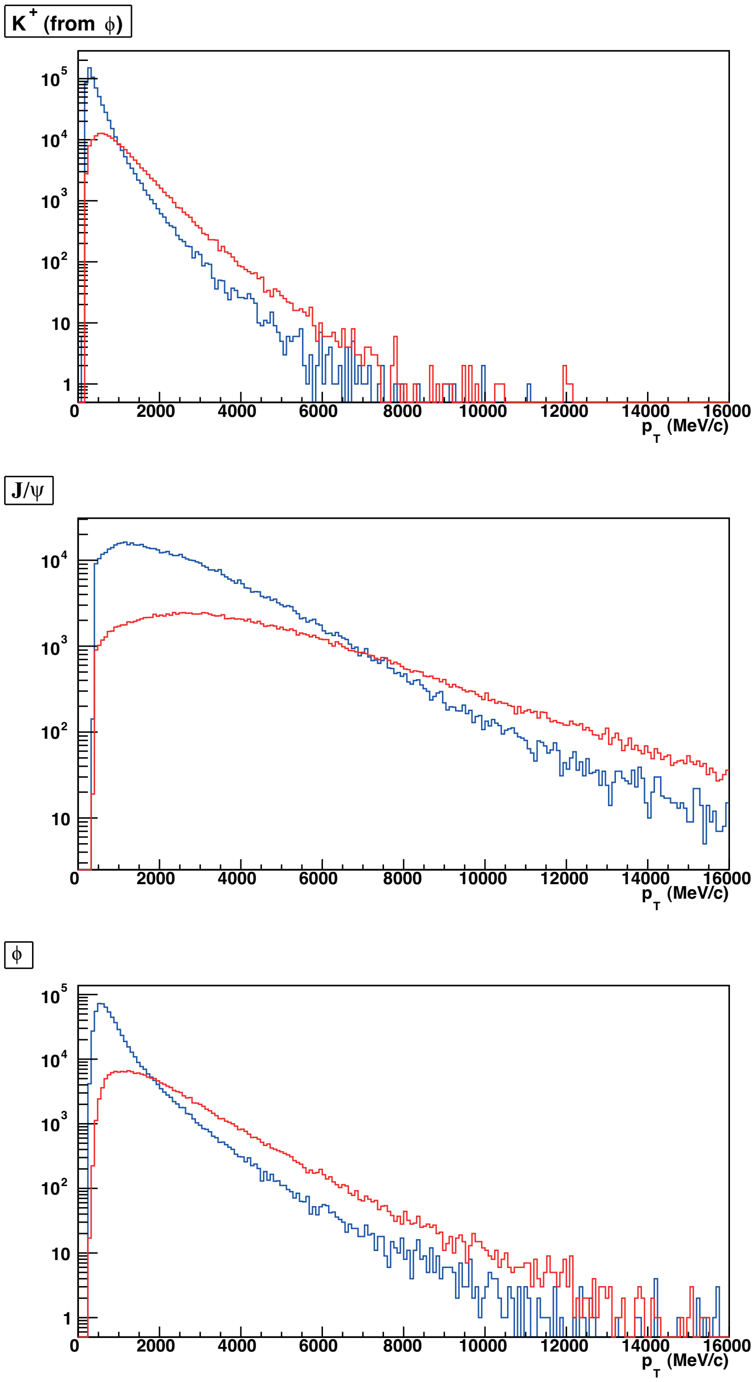

Figure 3.42: Distributions of kinematic variables after loose cuts are applied: MC background (blue) and signal (red) are overlapped.

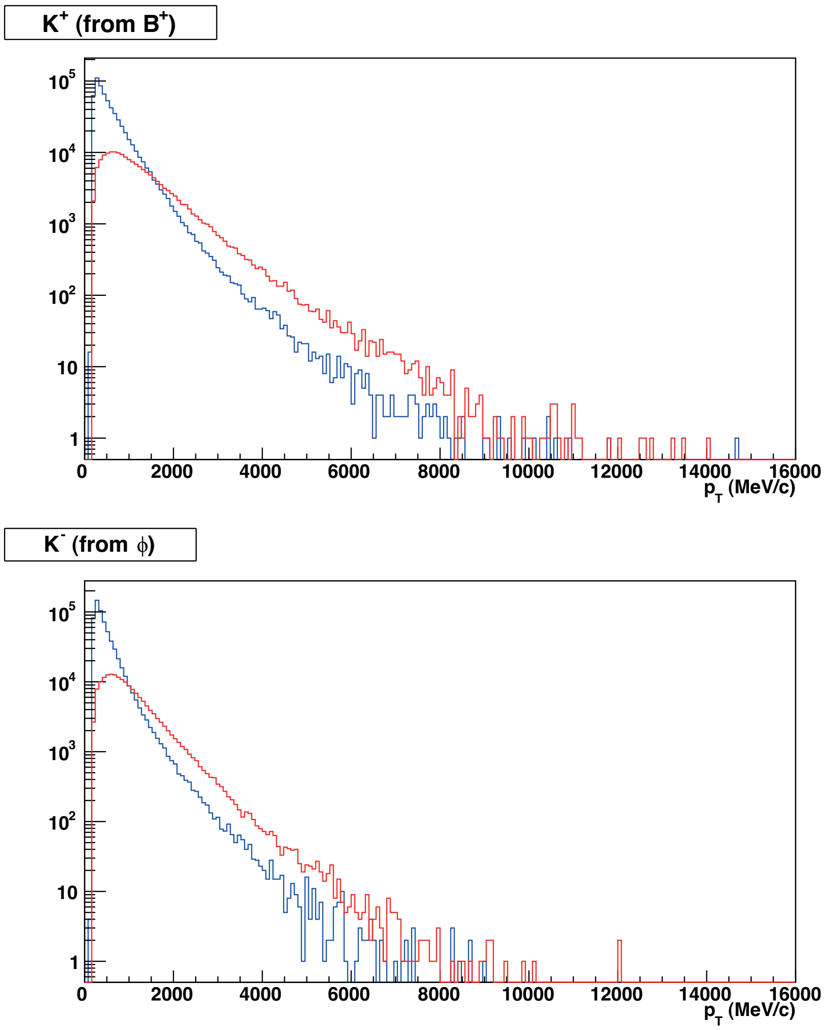

Figure 3.43: Distributions of kinematic variables after loose cuts are applied: MC background (blue) and signal (red) are overlapped.

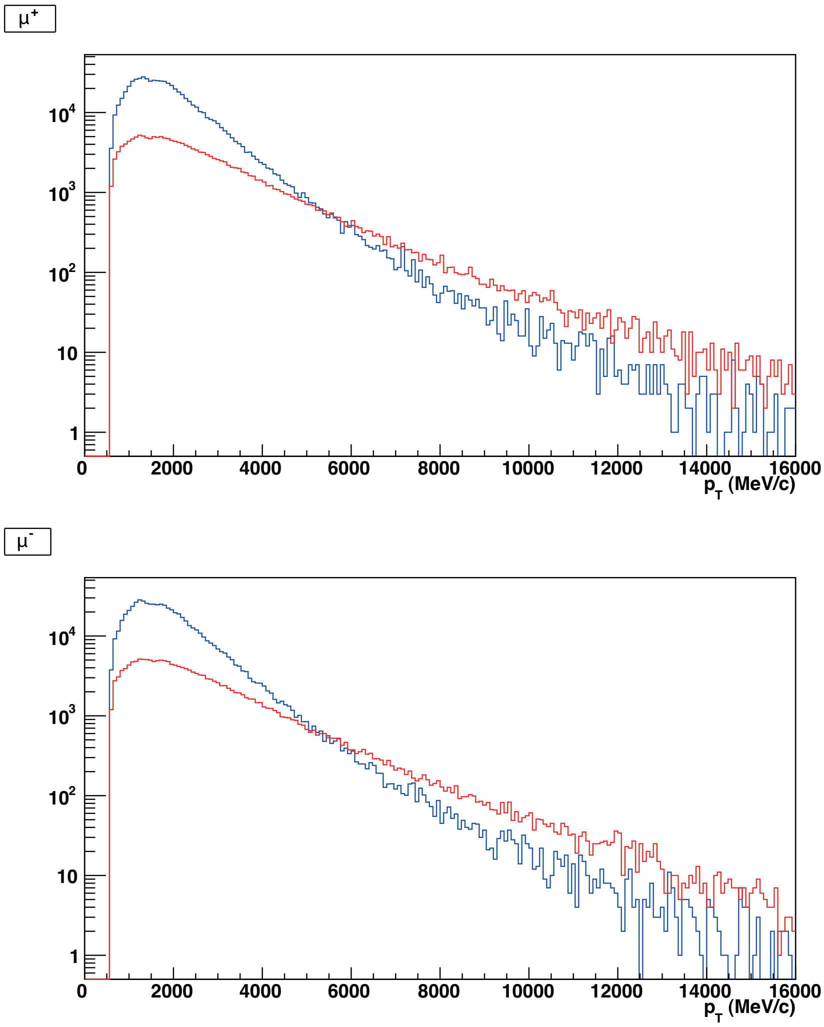

Figure 3.44: Distributions of kinematic variables after loose cuts are applied: MC background (blue) and signal (red) are overlapped.

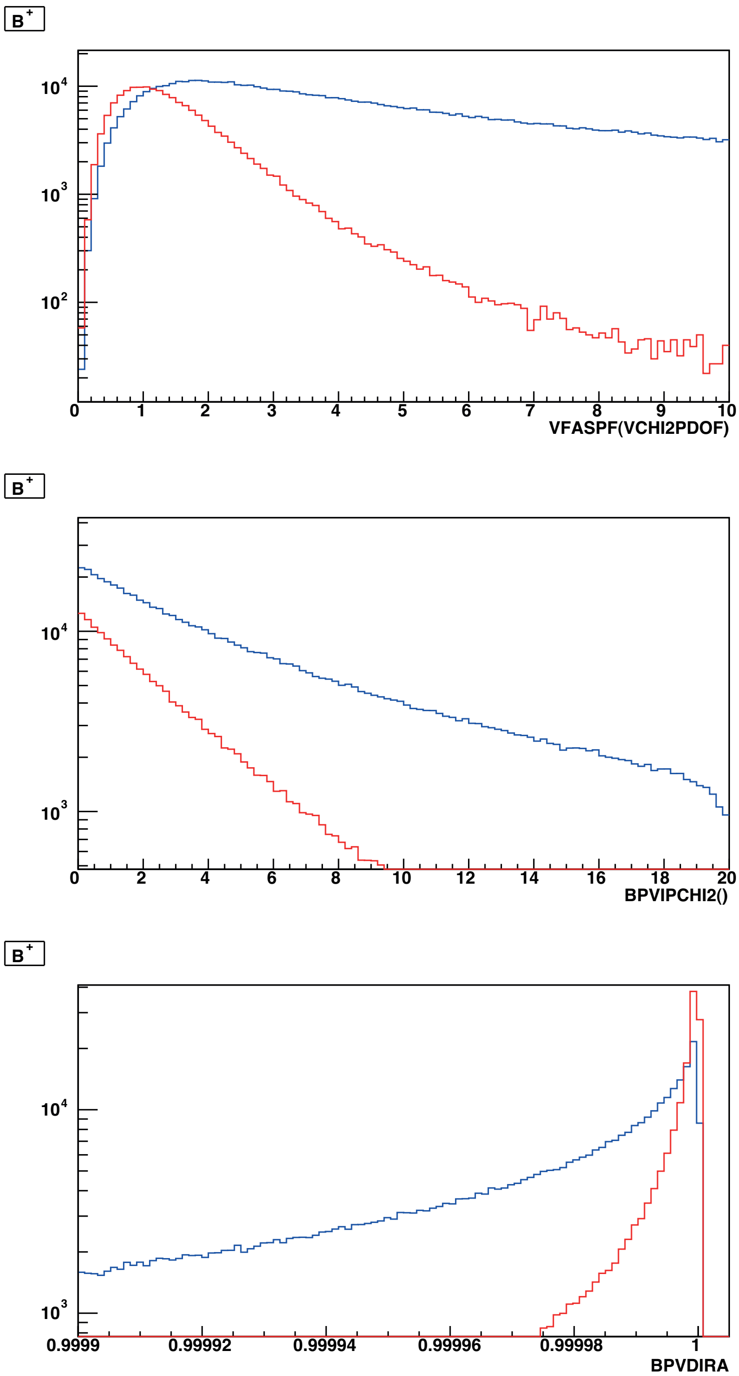

Figure 3.45: Distributions of kinematic variables after loose cuts are applied: MC background (blue) and signal (red) are overlapped.

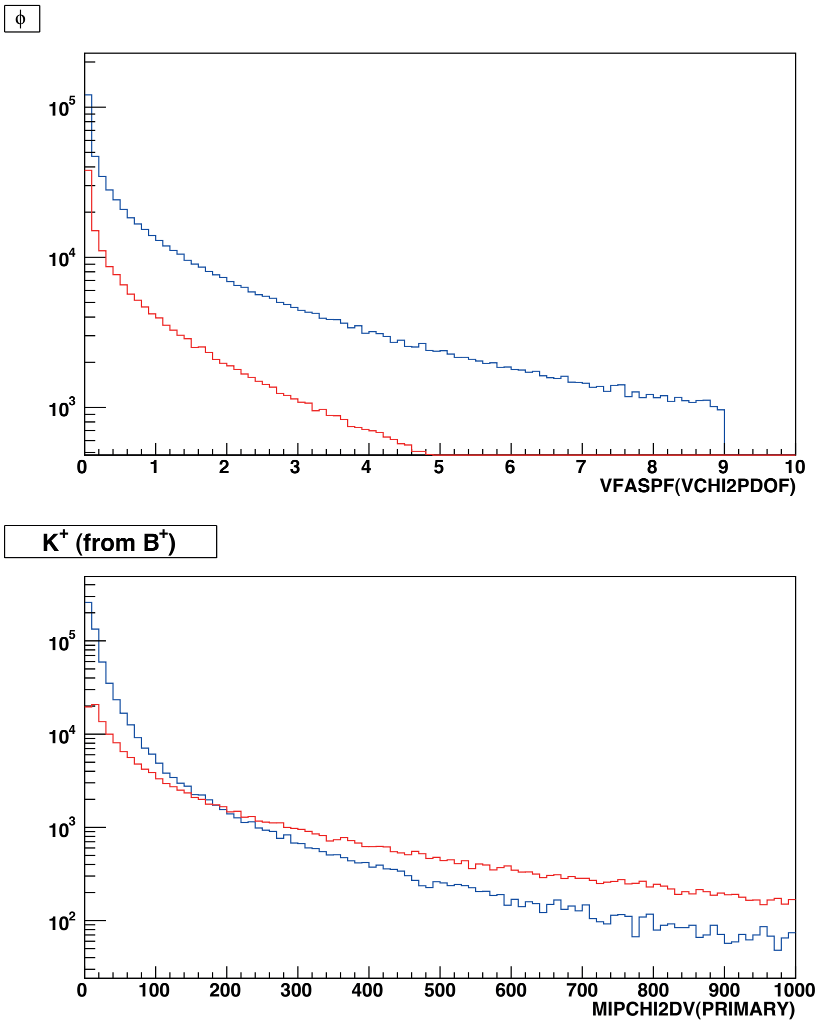

Figure 3.46: Distributions of kinematic variables after loose cuts are applied: MC background (blue) and signal (red) are overlapped.

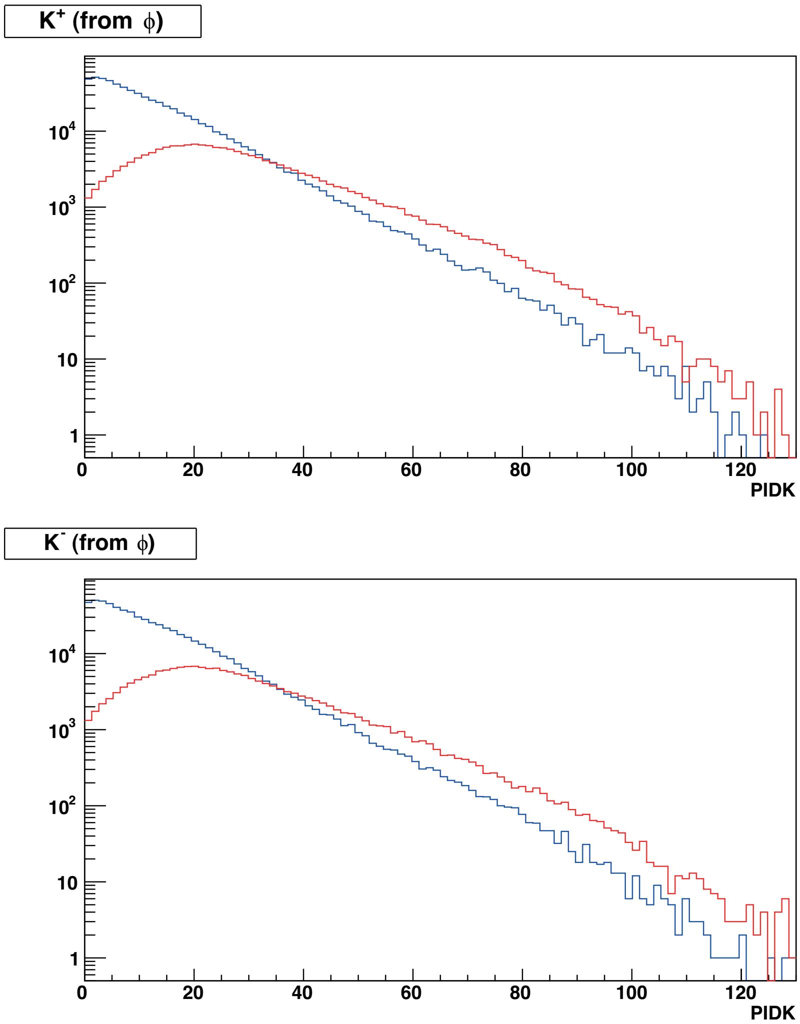

Figure 3.47: Distributions of kinematic variables after loose cuts are applied: MC background (blue) and signal (red) are overlapped.

Appendix C

Boosted Decision Tree (BDT)

In high energy physics experiments are used techniques that are able to identify interesting events between between very numerous background events.
It is so crucial to keep the signal the higher is possible and to suppress the most the background. The usual criterion used is based on a series of cuts whose efficiency is not always optimal: a lot of signal events could be get lost or a signal with a lost of background pollution can be obtained.
In order to optimize signal/background separation the so called *classifiers* are introduced [122, 123, 124, 125], that is mechanical learning techniques that provide, after preset cuts, optimal parameters for such separation. One of these is the *Decision tree*.
A decision tree consists of a binary split sequence of data forming a tree structure made up by intermediate nodes and final nodes called leaves.
It could be built by means a big number of discriminant variables that allow each node to separate signal events from background ones: the separation process is repeated for each node since the leaves node are reached. The crucial point is to define a criterion that describes the goodness of such separation: given so a couple of training data set, one for the signal and one for the background, the best cut on the single variable is established. One of the used criterion is called "Gini" [126].
Let's assume that all the events are weighted with weight W_i and define the purity P of the sample in a single node as:

$$P = \frac{\sum_s W_s}{\sum_s W_s + \sum_b W_b},$$

where $\sum_s$ is made over the signal events and $\sum_b$ over the background ones. When a node contains only signal events $P = 1$, in case of only background $P = 0$.

Let's define now *Gini* as:

$$Gini = \left(\sum_{i=1}^{n} W_i \right) P\,(1 - P)\,,$$

where the summation is over the event of each node and the quantity $P(1-P)$ is 0 both for pure signal and pure background sample. The criterion chosen is to maximize:

$$Criterion = Gini_{father} - Gini_{left\ son} - Gini_{right\ son}.$$

At the end of the process, if a leaf has purity greater than 1/2 (or than a fixed number), then it is called a signal leaf, otherwise, a background one. Events classified as signal will have a score equal to 1, the background one a score equal to -1.
In order to build a tree, it is necessary to have a sample containing well known event for signal and background. In figure 3.48 an example of a tree built with three variable to separate signal S from background B is shown. The separation at each node is obtained by maximizing the *Criterion* defined before.

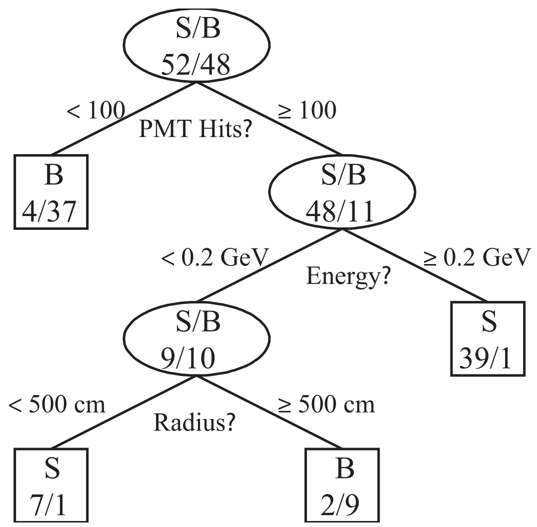

Figure 3.48: Example of a decision tree.

The decision tree are available from a long time so advantages and disadvantages are well known:

advantages:

- well known technique
- easy to understand
- the decision for each node is well known, unlike the neural networks
- easy approach
- no event is completely removed, so there is no loss of information

disadvantages:

- the decision tree are not stable: a little change or a little fluctuation in the sample used for the training may produce big differences both in the tree itself and in the results
- but a solution is given: the *boosting* $\rightarrow$ Boosted Decision Tree (BDT)

A decision tree could be made more stable by the combination of more tree: the weighted arithmetic mean over a great amount of tree is insensitive to fluctuations. The *boosting* approach consists in:

- reweighting bad classified events, that is signal events on a background leaf and background events on a signal leaf
- building and optimizing new tree with reweighted events
- score each tree
- average over all trees, using the tree-scores as weights

Several boosting algorithms are used such as AdaBoost (Adaptive Boosting), ϵ-Boost (shrinkage), ϵ-LogitBoost, ϵ-HingeBoost, LogitBoost, Gentle AdaBoost, Real AdaBoost.
In each boosting algorithm the same approach is used: first of all, given N total events in the sample, a starting weight equal to $1/N$ is given to each event, the total tree number is supposed to be M each with index m.

Let:

- x_i be the set of discriminating variables for the ith event
- $y_i = 1$ if the ith event is a signal event and $y_i = -1$ if the event is a background event
- $T_m(x_i) = 1$ if the set of variables for the ith event lands that event on a signal leaf and $T_m(x_i) = -1$ if the set of variables for that event lands it on a background leaf
- $I(y_i \neq T_m(x_i)) = 1$ if $y_i \neq T_m(x_i)$: bad classified event
- $I(y_i = T_m(x_i)) = 0$ if $y_i = T_m(x_i)$: correctly classified event

As example the AdaBoost method is described [126].

AdaBoost

We define for the mth tree:

$$err_m = \frac{\sum_{i=1}^{N} w_i I(y_i \neq T_m(x_i))}{\sum_{i=1}^{N} w_i},$$

that is the sum of bad classified events divided for the total weights. Let's now calculate:

$$\alpha_m = \beta \times \ln\left((1 - err_m)/err_m\right),$$

where $\beta = 1$ is used in the standard AdaBoost method. We change the weight of each event i, $i = 1, \ldots, N$:

$$w_i \rightarrow w_i \times e^{\alpha_m I(y_i \neq T_m(x_i))},$$

we renormalize the weights:

$$w_i \rightarrow \frac{w_i}{\sum_{i=1}^{N} w_i}.$$

The score for a given event is obtained:

$$T(x) = \sum_{m=1}^{M} \alpha_m T_m(x),$$

which is just the weighted sum of the scores of the individual trees. $T(x)$ is the final BDT output variable. In figure 3.49 AdaBoost outputs for the training MC sample and for the testing MC sample are shown for $N_{tree} = 1$, 50, and 1000. As can be seen, the signal/background separation for the training sample becomes better as N_{tree} increases: for $N_{tree} = 500$ signal and background events are completely separated. The testing sample becomes however quite stable after a few hundred tree iterations.

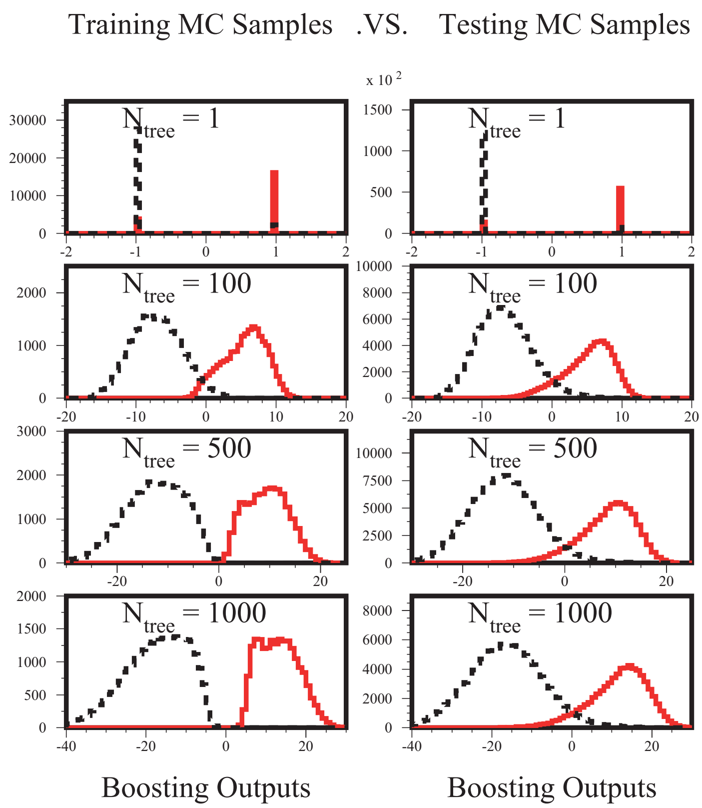

Figure 3.49: AdaBoost outputs for training MC samples (left column) and for testing MC samples (right column). Dotted black histograms represent the background events while solid red histograms represent the signal events. In this example $\beta = 0.5$ and there are 45 leaves per decision tree [126].

So, at the end of the training phase, one distribution for the signal and one for the background for each variable is obtained 3.50.

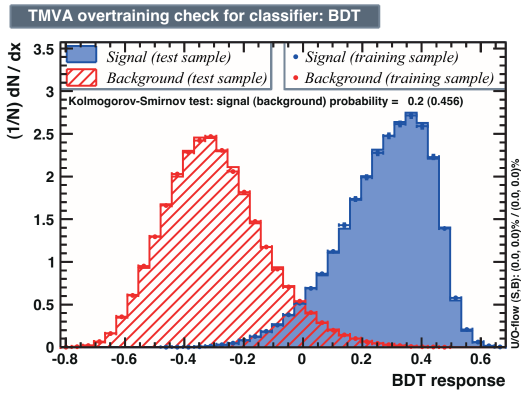

Figure 3.50: Example for signal and background distribution obtained at the end of the training phase.

Now we are able to apply the cut on the *BDT response* that provides the best signal/background separation. The chosen value is the one corresponding to the maximum of the *Significance* defined as $S/\sqrt{S+B}$ (figure 3.51), where S is the signal event number and B is the back ground event number.

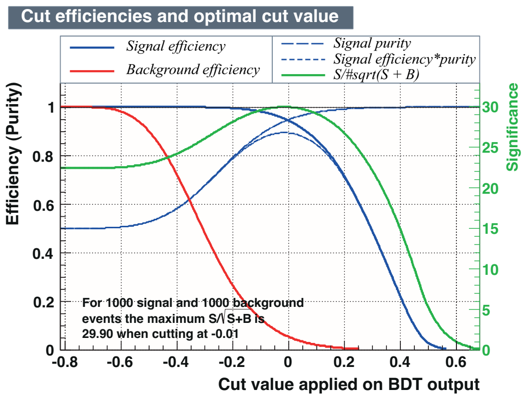

Figure 3.51: Example of BDT response plot: the best cut is suggested corresponding to the maximum value of the *Significance* (green line).

Bibliography

[1] C. S. Wu, E. Ambler, R. W. Hayward, D. D. Hoppes and R. P. Hudson, Phys. Rev. 105 (1957) 1413.

[2] M. Goldhaber, L. Grodzis, and A. Sunyar, (1958) Phys. Rev.109, 1015.

[3] J.H. Christenson et al., Phys. Rev. Lett. 13, 138 (1964).

[4] BaBar Collaboration, B. Aubert et al., *"Observation of CP violation in the B^0 meson system."* Phys. Rev. Lett., 87:091801 2001.

[5] BELLE Collaboration, K. Abe et al., *"Observation of large CP violation in the neutral B meson system."* Phys. Rev. Lett., 87:091802, 2001.

[6] ATLAS Collaboration, Observation of a new particle in the search for the Standard Model Higgs boson with the ATLAS detector at the LHC, Phys.Lett. B 716 (2012) 1-29.

[7] CMS Collaboration, Observation of a new boson at a mass of 125 GeV with the CMS experiment at the LHC, Phys.Lett. B 716 (2012) 30.

[8] LHCb Collaboration. "First evidence for the decay $B_s \to \mu^+\mu^-$", Phys. Rev. Lett. 110, 021801 (2013, DOI: 10.1103/PhysRevLett.110.021801.

[9] LHCb Collaboration. "Measurement of the CP-violating phase ϕ_s in the decay $B_s^0 \to J/\psi\phi$", Phys. Rev. Lett. 108, 101803 (2012), 10.1103/PhysRevLett.108.101803.

[10] S. Weinberg, *"A model of Leptons"*, Phys. Rev. Lett. 19 (1967) 1264.

[11] A. Salam and J. C.Ward, *"Electromagnetic and weak interactions"*, Phys. Lett. 13 (1964) 168.

[12] H. Fritzsch, M. Gell-Mann and H.Leutwyler, Phys. Lett. 47 (1973) 365.

[13] P.W. Higgs, Phys. Rev. Lett. 12, 132 (1964); idem., Phys. Rev. 145, 1156 (1966); F. Englert and R. Brout, Phys. Rev. Lett. 13, 321 (1964); G.S. Guralnik, C.R. Hagen, and T.W. Kibble, Phys. Rev. Lett. 13, 585 (1964).

[14] C. Amsler et al. (Particle Data Group), PL B667, 1 (2008) and 2009 partial update for the 2010 edition (URL: http://pdg.lbl.gov)

[15] I.Bigi and A.I.Sanda, *"CP Violation"*, Cambridge monographs on particle physics, nuclear and cosmology, 9 (2000)

[16] N. Cabibbo, *"Unitary Symmetry and Leptonic Decays"*, Phys. Rev. Lett. 10 (1963) 531-533.

[17] M. Kobayashi and T. Maskawa, Prog. Theor. Phys. 49 (1972) 282.

[18] M. Kobayashi and T. Maskawa, *"CP Violation in the Renormalizable Theory of Weak Interaction"*, Prog. Theor. Phys. 49 (1973) 652-657.

[19] L. Wolfenstein, Phys. Rev. Lett. 51, 1945 (1983).

[20] K.A. Olive et al. (Particle Data Group), Chin. Phys. C, 38, 090001 (2014)

[21] R. Aleksan et al., Phys. Rev. Lett. 73, 18 (1994).

[22] M. Kobayashi and T. Maskawa, Prog. Theor. Phys. 49, 652 (1973).

[23] S. W. Herb et al., Phys. Rev. Lett. 39, 252 (1977).

[24] D. Buskulic et al. (ALEPH Collab.), Phys. Lett. B384, 449 (1996); P. Abreu et al. (DELPHI Collab.), Z. Phys. C68, 541 (1995).

[25] T. Aaltonen et al. (CDF Collab.), Phys. Rev. Lett. 99, 202001 (2007).

[26] V.M. Abazov et al. (D0 Collab.), Phys. Rev. Lett.99, 052001 (2007).

[27] T. Aaltonen et al. (CDF Collab.), Phys. Rev. Lett. 99, 052002 (2007).

[28] T. Aaltonen et al. (CDF Collab.), Phys. Rev. Lett. 107, 102001 (2011).

[29] V. M. Abazov et al. (D0 Collab.), Phys. Rev. Lett. 101, 232002 (2008).

[30] T. Aaltonen et al. (CDF Collab.), Phys. Rev. D 80, 072003 (2009).

[31] LHCb Collab., EPJ Web of Conferences 28 04010 (2012), DOI: 10.1051/epj-conf201/22804010.

[32] V. Weisskopf and E. P. Wigner, Z. Phys. 63, 54 (1930); Z. Phys. 65, 18 (1930).

[33] The LHCb collaboration, Aaij, R., Adeva, B. et al.: Measurement of the CKM angle γ from a combination of LHCb results, J. High Energ. Phys. (2016) 2016: 87. doi:10.1007/JHEP12(2016)087.

[34] I. Dunietz and J.L. Rosner, Phys. Rev. D34, 1404 (1986).

[35] Ya.I. Azimov, N.G. Uraltsev, and V.A. Khoze, Sov. J. Nucl. Phys. 45, 878 (1987) [Yad. Fiz. 45, 1412 (1987)].

[36] I.I. Bigi and A.I. Sanda, Nucl. Phys. B281, 41 (1987).

[37] M. Adinolfi, *"Misura della vita media di mesoni B neutri e carichi"*, Tesi di dottorato, Università degli studi di Genova (1994).

[38] B. L. Combridge et al., Phys. Lett. B70 (1977) 234.

[39] B. Aubert et al. (BaBar Collab.), Phys. Rev. Lett. 87, 091801 (2001).

[40] K. Abe et al. (Belle Collab.), Phys. Rev. Lett. 87, 091802 (2001).

[41] J. Brod and J. Zupan, The ultimate theoretical error on gamma from $B \to DK$ decays, JHEP 1401 (2014) 051, arXiv:1308.5663.

[42] S. L. Glashow, J. Iliopoulos, and L. Maiani, Phys. Rev. D 2, 1285 (1970).

[43] A. J. Buras, J. Girrbach, D. Guadagnoli, and G. Isidori, On the standard model prediction for $\mathcal{B}(B_{s,d} \to \mu^+\mu^-)$, Eur. Phys. J. C72 (2012) 2172, arXiv:1208.0934.

[44] A. J. Buras, PoS BEAUTY 2011, 008 (2011) [arXiv:1106.0998 [hep-ph]].

[45] K. De Bruyn, R. Fleischer, R. Knegjens, P. Koppenburg, M. Merk and N. Tuning, Phys. Rev. D 86, 014027 (2012), DOI: 10.1103/PhysRevD.86.014027.

[46] LHCb collaboration, R. Aaij et al., Strong constraints on the rare decays $B_s^0 \to \mu^+\mu^-$ and $B^0 \to \mu^+\mu^-$, Phys. Rev., DOI: 10.1103/PhysRevLett.108.231801.

[47] First evidence for the decay $B_s^0 \to \mu^+\mu^-$, The LHCb collaboration, Phys. Rev. Lett. 110, 021801 (2013), DOI: 10.1103/PhysRevLett.110.021801.

[48] 't Hooft, G. (1973). "Dimensional regularization and the renormalization group". Nuclear Physics B 61: 455.

[49] Weinberg, S. (1973). "New Approach to the Renormalization Group". Physical Review D 8 (10): 3497-3509.

[50] A.V. Manohar and H. Georgi, Nucl. Phys. B234, 189 (1984).

[51] K.G. Wilson, Phys. Rev. D10, 2445 (1974).

[52] W. Zimmermann, in "Lectures on Elementary Particles and Quantum Field Theory", ed. S. Deser et al., MIT Press, Cambridge, MA (1971); K. Symanzik, Nucl. Phys. B226, 187 (1983); Nucl. Phys. B226, 205 (1983).

[53] M. Lüscher & P. Weisz, Commun. Math. Phys. 97, 59 (1985).

[54] Y. Iwasaki, UT-HEP-118.

[55] B.A. Thacker & G.P. Lepage, Phys. Rev. D43, 196 (1991); G.P. Lepage et al., Phys. Rev. D46, 4052 (1992).

[56] R.J. Dowdall et al., Phys. Rev. D86, 094510 (2012) [arXiv:1207.5149].

[57] A. G. Grozin Introduction to the Heavy Quark Effective Theory Part 1, BUD-KERINP 92-97, NOVOSIBIRSK 1992, arXiv:hep-ph/9908366v1 16 Aug 1999.

[58] B. Blossier et al. [ETM Collaboration], "A Proposal for B-physics on current lattices" JHEP 1004 (2010) 049, DOI: 10.1007/JHEP04(2010)049.

[59] P. Dimopoulos et al. [ETM Collaboration], "Lattice QCD determination of mb, fB and fBs with twisted mass Wilson fermions" JHEP 1201 (2012) 046, DOI: 10.1007/JHEP01(2012)046.

[60] N. Carrasco et al. [ETM Collaboration], "B-physics from Nf = 2 tmQCD: the Standard Model and beyond" JHEP 1403 (2014) 016, DOI: 10.1007/JHEP03(2014)016.

[61] Andrew T. Lytle, "Heavy quark masses from lattice QCD", published by EDP Sciences, 2016

[62] P. Lefèvre and T. Pettersson. *"The Large Hadron Collider: conceptual design"*. CERN/AC/95/05/LHC, 1995.

[63] ATLAS Collaboration, W.W. Armstrong et al. *"ATLAS: Technical Proposal for a General-Purpose pp Experiment at the Large Hadron Collider at CERN"*. CERN/LHCC/94-43, 1994.

[64] CMS Collaboration. *"Technical Proposal"*. CERN/LHCC/94-38, 1994.

[65] ALICE Collaboration, N. Ahmad et al. *"A Large Ion Collider Experiment - Technical Proposal"*. CERN/LHCC/95-71, 1995.

[66] LHCb Collaboration. *"Technical Proposal"*. CERN-LHCC/98-4, 1998.

[67] http://lhcb-track.web.cern.ch/lhcb-track/

[68] LHCb Collaboration, "LHCb Detector Performance", Int. J. Mod. Phys. A 30, 1530022 (2015), DOI: 10.1142/S0217751X15300227

[69] U. Amaldi et al., Phys. Lett. 44B (1973), p. 112.

[70] LHCb, RICH TDR, CERN LHCC 2000-037, LHCb TDR 3, 6 September 2000.

[71] LHCb Calorimeters, TDR, CERN/LHCC/2000-0036, LHCb TDR 2, 6 September 2000.

[72] LHCb, Muon System TDR, CERN LHCC 2001-010, LHCb TDR 4, 28 May 2001.

[73] LHCb collaboration, *"LHCb addendum to the muon system technical design report"*, CERN-LHCC-2003-002, http://cdsweb.cern.ch/record/600536.

[74] LHCb collaboration, *"LHCb second addendum to the muon system technical design report"*, CERN-LHCC-2005-012, http://cdsweb.cern.ch/record/831955.

[75] Velo TDR, CERN/LHCC 2001-0011, LHCb TDR 5, 31 May 2001.

[76] LHCb Magnet, TDR, CERN/LHCC/2000-007.

[77] LHCb collaboration, R. Antunes-Nobrega et al., *"LHCb reoptimized detector design and performance"*, CERN-LHCC-2003-030, http://cdsweb.cern.ch/record/630827.

[78] LHCb collaboration, P.R. Barbosa-Marinho et al., *"LHCb inner tracker technical design report"*, CERN-LHCC-2002-029, http://cdsweb.cern.ch/record/582793.

[79] LHCb collaboration, P.R. Barbosa-Marinho et al., *"Outer tracker technical design report"*, CERN-LHCC-2001-024, http://cdsweb.cern.ch/record/519146.

[80] LHCb, A. Alves et al., The LHCb Detector at the LHC, JINST 3 (2008) S08005.

[81] LHCb collaboration, R. Aaij et al., Measurement of b-hadron branching fractions for two-body decays into charmless charged hadrons, JHEP 1210 (2012) 037, DOI: 10.1007/JHEP10(2012)037.

[82] LHCb RICH group, M. Adinolfi et al., Performance of the LHCb RICH detector at the LHC, Eur. Phys. J. C 73 (2012) 2431. 25 p.

[83] Particle identification - Lippmann, Christian, Nucl.Instrum.Meth. A666 (2012) 148-172, DOI: 10.1016/j.nima.2011.03.009.

[84] G. Martellotti, R. Santacesaria and A. Satta, *"Particle rates in the LHCb muon detector"*, Note LHCb-2005-075, http://cdsweb.cern.ch/record/896904.

[85] Alves Jr. et al, Performance of the LHCb muon system, 2013 JINST 8 P02022.

[86] R. Aaij and J. Albrecht, The LHCb Trigger and its Performance in 2011, JINST 8 (2013) P04022, DOI: 10.1088/1748-0221/8/04/P04022.

[87] http://lhcb.web.cern.ch/lhcb/speakersbureau/html/

[88] A. Puig, The LHCb trigger in 2011 and 2012, LHCb-PUB-2014-046. CERN-LHCb- PUB-2014-046.

[89] LHCb Collaboration, "The LHCb Trigger and its Performance in 2011", JINST 8 (2013) P04022, DOI: 10.1088/1748-0221/8/04/P04022.

[90] R. Aaij and J. Albrecht, Muon triggers in the high level trigger of LHCb, LHCb-PUB-2011-017.

[91] F. Archilli et al., Performance of the muon identification at LHCb, JINST 8 (2013) P10020, DOI: 10.1088/1748-0221/8/10/P10020.

[92] G. Corti et al., "How the Monte Carlo production of a wide variety of different samples is centrally handled in the LHCb experiment", J. Phys.: Conf. Ser. 664 (2015) 072014, DOI: 10.1088/1742-6596/664/7/072014.

[93] K.A. Olive et al. (Particle Data Group), Chin. Phys. C, 38, 090001 (2014).

[94] CDF Collaboration (D. Acosta (Florida U.) et al.). Aug 2005. Published in Phys.Rev.Lett. 96 (2006) 202001

[95] "Measurement of b-hadron masses", LHCb Collaboration (R. Aaij et al.). Dec 2011. 15 pp. Published in Phys.Lett. B708 (2012) 241-248

[96] LHCb collaboration, R. Aaij et al., "Measurements of B_c^+ production and mass with the $B_c^+ \to J/\psi\pi^+$ decay", Phys. Rev. Lett. 109 (2012) 232001, DOI: 10.1103/PhysRevLett.109.232001.

[97] LHCb collaboration, R. Aaij et al., "Measurements of the Λ_b^0, Ξ_b^- and Ω_b^- baryon masses", Phys. Rev. Lett. 110 (2013) 182001, DOI: 10.1103/PhysRevLett.110.182001.

[98] Y. Amhis et al., "Momentum scale calibration for early 2011 data", CERN-LHCb-INT-2011-053.

[99] LHCb collaboration, R. Aaij et al., "First observation of the $B_s \to J/\psi\phi\phi$ decay and measurement of the ratio $\mathcal{B}(B_s \to J/\psi\phi\phi)/\mathcal{B}(B_s \to J/\psi\phi)$", J. High Energ. Phys. (2016) 2016: 40. DOI: 10.1007/JHEP03(2016)040.

[100] CLEO Collaboration, "First Observation of the Decay $B \to J/\psi\phi K$", Phys.Rev.Lett.84:1393,2000, DOI: 10.1103/PhysRevLett.84.1393.

[101] LHCb, M. Needham, "Precision measurement of D meson mass differences", Journal of High Energy Physics, Volume 2013, Issue 6, DOI: 10.1007/JHEP06(2013)065.

[102] LHCb collaboration, "Measurement of the Λ_b^0, Ξ_b^- and Ω_b^- baryon masses", Phys. Rev. Lett. 110, 182001 (2013), DOI: 10.1103/PhysRevLett.110.182001.

[103] LHCb collaboration, "First observation of a baryonic B_c^+ decay", Phys. Rev. Lett. 113, 152003 (2014), DOI: 10.1103/PhysRevLett.113.152003.

[104] LHCb collaboration, "Updated measurement of b-hadron masses with exclusive $J/\psi X$ decays in 2010 data", LHCb-ANA-2011-045 15/05/2012.

[105] *"Rare B^+ decays into states containing a J/ψ meson and a meson with $s\bar{s}$ quark content*, BaBar Collaboration (Bernard Aubert (Annecy, LAPP) et al.). Apr 2003. 7 pp., Published in Phys.Rev.Lett. 91 (2003) 071801

[106] *"Search for the $X(4140)$ state in $B^+ \to J/\psi\phi K^+$ decays with the D0 detector"*, D0 Collaboration (Victor Mukhamedovich Abazov (Dubna, JINR) et al.). Sep 25, 2013. 9 pp., Published in Phys.Rev. D89 (2014) 1, 012004

[107] *"Search for the $X(4140)$ state in $B^+ \to J/\psi\phi K^+$ decays"*, LHCb Collaboration (R Aaij (NIKHEF, Amsterdam) et al.). Feb 2012., Published in Phys.Rev. D85 (2012) 091103

[108] LHCb Collaboration, "Amplitude analysis of $B^+ \to J/\psi\phi K^+$ decays", Phys. Rev. D 95, 012002 (2017), DOI: 10.1103/PhysRevD.95.012002.

[109] LHCb Collaboration, "Observation of $J/\psi\phi$ structures consistent with exotic states from amplitude analysis of $B^+ \to J/\psi\phi K^+$ decays", Phys. Rev. Lett. 118, 022003 (2017), DOI: 10.1103/PhysRevLett.118.022003.

[110] F. E. Close et al., Phys. Rev. D57, 5653 (1998).

[111] The BABAR Collaboration, "Study of $B^{\pm,0} \to J/\psi K^+K^-K^{\pm,0}$ and search for $B^0 \to J/\psi\phi$ at BaBar", Phys. Rev. D 91, 012003 (2015), DOI: 10.1103/PhysRevD.91.012003.

[112] *"Measurement of $\sigma(pp \to b\bar{b}X)$ at $\sqrt{s} = 7$ TeV in the forward region"*, LHCb Collaboration, Phys.Lett. B694 (2010) 209-216.

[113] *"Production of J/psi and Upsilon mesons in pp collisions at sqrt(s) = 8 TeV"*, LHCb collaboration, J. High Energy Phys. 06 (2013) 064, DOI: 10.1007/JHEP06(2013)064.

[114] R. Brun and F. Rademakers, *ROOT: An object oriented data analysis framework*, Nucl. Instrum. Meth. A389 (1997).

[115] A. Perieanu, "Identification of Ghost Tracks using Neural Networks", LHCb 2007-158.

[116] M. Oreglia, A Study of the Reactions $\psi' \to \gamma\gamma\psi$, Ph.D. thesis (1980).

[117] J. Gaiser, Charmonium Spectroscopy From Radiative Decays of the *J/psi* and ψ', Ph.D. thesis (1982).

[118] T. Skwarnicki, A study of the radiative cascade transitions between the Upsilon-prime and Upsilon resonances, Ph.D. thesis, Institute of Nuclear Physics, Krakow, DESY-F31-86-02 (1986).

[119] D. Martínez Santos, F. Dupertuis, "Mass distributions marginalized over per-event errors", NIM A, 764, 150 (2014), DOI: 10.1016/j.nima.2014.06.081.

[120] R. Aaij et al., "Precision measurement of D meson mass differences", JHEP 06 (2013) 065, DOI: 10.1007/JHEP06(2013)065.

[121] LHCb collaboration, R. Aaij et al., "Prompt K_S^0 production in pp collisions at $\sqrt{s} = 0.9$ TeV", Phys. Lett. B693 (2010) 69, DOI: 10.1016/j.physletb.2010.08.055.

[122] L. Breiman, J.H. Friedman, R.A. Olshen, and C.J. Stone, Classification and Regression Trees, Wadsworth International Group, Belmont, California (1984).

[123] R.E. Schapire, The boosting approach to machine learning: An overview, MSRI Workshop on Nonlinear Estimation and Classification, (2002).

[124] Y. Freund and R.E. Schapire, A short introduction to boosting, Journal of Japanese Society for Artificial Intelligence, 14(5), 771-780, (September, 1999). (Appearing in Japanese, translation by Naoki Abe.)

[125] J. Friedman, Recent Advances in Predictive (Machine) Learning, Proceedings of Phystat2003, Stanford University, (September 2003).

[126] Hai-Jun Yanga, Byron P. Roea, Ji Zhub, "Studies of Boosted Decision Trees for MiniBooNE Particle Identification.", Nucl.Instrum.Meth. A555 (2005) 370-385, DOI: 10.1016/j.nima.2005.09.022.